CARBON BASED NANOELECTROMECHANICAL RESONATORS

by

Chung-Chiang Wu

A dissertation submitted in partial fulfillment
of the requirements for the degree of
Doctor of Philosophy
(Electrical Engineering)
in The University of Michigan
2012

Doctoral Committee:
    Assistant Professor Zhaohui Zhong, Chair
    Professor L. Jay Guo
    Associate Professor Wei Lu
    Assistant Professor A. John Hart

To
my family

ACKNOWLEDGEMENTS

Looking back what I have achieved during Ph. D study, all kinds of emotions and thoughts keep running through my mind. I am very lucky and grateful to have the support from my research advisor, collaborators, my friends, my beloved parents and partner to overcome various frustrations and challenges throughout these years. I cannot express enough thanks to all of you.

Firstly, I would like to express my gratitude to my research advisor, Professor Zhaohui Zhong, for his guidance and support during my graduate studies. In early 2008, I left my former group and almost gave up studying Ph. D until I met Zhaohui. I was very lucky to become his first graduate student in UM. I resumed my Ph. D dream and found new motivation to support me to pursue it continuously. In the past three and half years and with countless hours of discussion, I have learnt greatly about carbon nanotubes and their applications from him. In addition and more importantly, he taught me becoming a great scientist with right research attitude by setting up an excellent example. These will serve me well in the future no matter where my career would lead me. Also, I would like to thank the members of my doctoral committee, Professor Jay Guo, Professor Wei Lu, and Professor John Hart, whose suggestions and feedbacks were very constructive and appreciated.

I also would like to thank Dr. Yongyi Zhang, Sameh Tawfick, JingJing Li, and Professor John Hart, with whom I collaborated on the carbon nanotube growth. I was also fortunate to receive support and assistance from my friends who worked closely with me in the clean room: Tao Lin, Wei Guo, Gaun Huang, Luke Lee, Yi-Kuei Wu, Chi-Shen Lee, and Ting Chang. By working and learning with each other in the clean room, we developed solid friendship. I would specifically like to give thanks to Ting Chang for providing me additional help on my research writing and discussion. I also thank all LNF crew for helping me to fabricate and characterize my devices.

I would also like to thank the members of Zhong's group for their discussions, collaborations, and friendship: Chang-Hua Liu, Girish Kulkarni, Kyunghoon Lee, Seunghyun Lee, Che-Hung Liu, and Rui Li. Thank Dr. Nanditha Dissanayake for his valuable discussions and suggestions on my research, thesis draft, and job hunting.

Furthermore, I would like to express my warmest gratitude for the love and support from my family. Sincerely thank my parents, who are always caring and providing their love unconditionally. I would not become who I am and achieve what I have without you. To my brothers, thank you for taking care of our family so that I can focus on studying without worrying and hesitation

Finally, to the love of my life, Chia-Yu Lin, thank you for accompanying me in this long journey. Without you, I cannot imagine how difficult it would be. You have been more patient than I could have ever asked and you were always there for me through ups and downs. I cannot wait to share our life together, and I cannot wait to see what life will lead us together in the future. I love you.

.

TABLE OF CONTENTS

LIST OF FIGURES

ABSTRACT

Owing to their light mass and high Young's modulus, carbon nanotubes (CNTs) and graphene are promising candidates for nanoelectromechanical resonators capable of ultrasmall mass and force sensing. Unfortunately, the mass sensitivity of CNT resonators is impeded by the low quality factor (Q) caused by intrinsic losses. Therefore, one should minimize dissipations or seek an external way to enhance Q in order to overcome the fundamental limits.

In this thesis, I first carried out a one-step direct transfer technique to fabricate pristine CNT nanoelectronic devices at ambient temperature. This process technique prevents unwanted contaminations, further reducing surface losses. Using this technique, CNT resonators was fabricated and a fully suspended CNT p-n diode with ideality factor equal to 1 was demonstrated as well. Subsequently, the frequency tuning mechanisms of CNT resonators were investigated in order to study their nonlinear dynamics. Downward frequency tuning caused by capacitive spring softening effect was demonstrated for the first time in CNT resonators adopting a dual-gate configuration.

Leveraging the ability to modulate the spring constant, parametric amplification was demonstrated for Q enhancement in CNT resonators. Here, the simplest parametric amplification scheme was implemented by modulating the spring constant of CNTs at twice the resonance frequency through electrostatic gating. Consequently, at least 10 times Q enhancement was demonstrated and Q of 700 at room temperature was the highest record to date. Moreover, parametric amplification shows strong dependence on DC gate voltages, which is believed due to the difference of frequency tunability in different vibrational regimes.

Graphene takes advantages over CNTs due to the availability of wafer-scale graphene films synthesized by chemical vapor deposition (CVD) method. Thus, I also examined graphene resonators fabricated from CVD graphene films. Ultra-high frequency (UHV) graphene resonators were demonstrated, and the *Qs* of graphene resonators are around 100. Future directions of graphene resonators include investigating the potential losses, exploring the origin of nonlinear damping, and demonstrating parametric amplification for *Q* enhancement.

CHAPTER 1

INTRODUCTION

1.1 Introduction

Microelectromechancial systems (MEMS) are in general referred to miniature and multifunctional microsystems. They are usually built by micromachining techniques and composed of two essential components: mechanical elements and microelectronic circuits which control the mechanical elements [1-2]. Over the past decades, MEMS have been intensively studied in forms of sensors and actuators and deployed in a variety of technologies. We can easily find them employed in our daily life such as piezoelectrics in inkjet printers, accelerometers in video game controllers (Nintendo Wii), and pressure sensors in car tires.

In the meantime, with the fabrication techniques of microelectronics pushed deep into the submicron scale, nanoelectromechanical systems (NEMS), a successor of MEMS, have also attracted great interests from researchers [3-5] due to their intriguing attributes. The effective masses of NEMS are usually less than femtograms (10^{-15} g) and can be as low as attogram (10^{-18} g) if carbon materials are utilized. Thus, NEMS are expected to operate at much higher frequencies with lower power consumption, and to have mechanical quality factors (Q) around tens of thousands [6]. These remarkable properties make them promising in ultrasmall mass and force sensing [7-11]. In principle, the sensitivity can be improved by reducing the effective mass of a system (nanostructure or low mass density), increasing the resonance frequency, and decreasing the linewidth of the resonance. Hence, carbon nanotubes (CNTs) and graphene would be the potential candidates to achieve the ultimate single-molecule and atomic sensing due to their high stiffness, light effective masses and ultrasmall cross sections. In addition, they can be defect-free since they are formed through bottom-up technique. To this end, I focused on these two carbon materials as NEMS mechanical elements in this thesis. First, I implemented both self-detecting carbon nanotube and graphene nanoelectromechanical resonators. Subsequently, I utilized these resonators made out of CNTs and graphene to investigate their linear and nonlinear dynamics throughout this thesis.

In this chapter, I would like to briefly introduce their remarkable electrical and mechanical properties. First, the history of carbon allotropes is described shortly in section 1.2, and the synthesis of nanotubes and graphene is introduced in section 1.3. Their electrical properties are then discussed in section 1.4 and their mechanical properties are presented in section 1.5. In section 1.6, I recap previous works regarding nanotube and graphene nanoelectromechanical resonators. In the end, this chapter is concluded with a summary and the outline of this thesis.

1.2 History of carbon allotropes

Carbon plays an irreplaceable role in the nature since it is the basis of all organic compounds. Due to the flexibility of carbon-carbon bonding, carbon allotropes are formed either naturally or artificially and show a variety of physical properties. Graphite and diamonds are only carbon allotropes occurring naturally. On the other hand, the artificial ones are studied and developed due to the demands for new materials driven by diverse applications. Among these carbon allotropes, “graphene” – a two-dimensional (2D) structure– is called the mother of all graphitics since it is the building block for graphitics of all dimensionalities and also the basis to understand the electrical properties of other carbon allotropes. Graphene is a flat monolayer of carbon atoms tightly packed into a honeycomb lattice. Graphene can be wrapped up into fullerenes (C_{60}, carbon atoms are arranged spherically and treated as zero-dimensional (0D) objects with discrete energy states) [12], or rolled into one-dimensional (1D) nanotubes (rolling it along a given direction and reconnecting the carbon bonds) [13] or stacked into 3D graphite, as shown in Figure 1.1 [14].

Over the past two decades, progress in chemistry and manufacturing has led to the success of synthesizing these different dimensional carbon allotropes. Fullerenes were carried out first [12] and several years later, “helical microtubules of graphitic carbon” known as “carbon nanotube” was observed by Iijima [13]. The success of synthesizing nanotubes allows nanotubes widely used to fabricate novel nanoelectronics based on their 1D structures and remarkable mechanical and optical properties. To synthesize graphene, a number of researches have been conducted over a century. Unfortunately, although graphene is thought as the mother of all graphitics, it was believed not existing in a free state due to its instability with respect to the formation of fullerenes or nanotubes. It was only studied as a theoretical model to predict the electrical properties of other carbon allotropes on that time. However, this thought of graphene being inaccessible was overturn in 2004 when free-standing graphene was unexpectedly found by peeling off graphites [15]. The founding of graphene makes it a rising star extensively explored by the electronics community nowadays, not just a theoretical model in condensed matter physics.

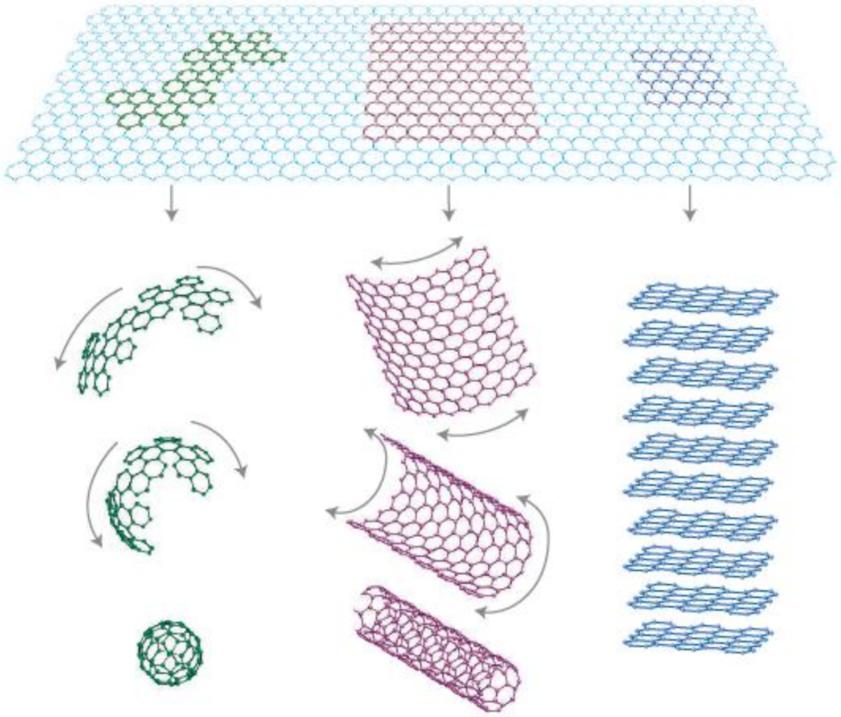

Figure 1.1. Carbon allotropes. Graphene (top) is a 2D honeycomb lattice of carbon atoms. Fullerenes (C_{60}, bottom left) are viewed by wrapping graphene with the introduction of pentagons on the hexagonal lattice. Carbon nanotubes (bottom middle) are rolled-up cylinders of graphene. Graphite (bottom right) can be viewed as a stack of graphene layers [14].

1.3 Synthesis of carbon nanotubes and graphene

1.3.1 Carbon nanotubes

A nanotube can be thought by rolling a graphene sheet along a given direction to form a hollow cylinder of covalently bonded carbon atoms. Depending on how many graphene sheets (walls) are rolled concentrically, a nanotube can be further classified as: a single-walled carbon nanotube (SWNT) or a multi-walled carbon nanotube (MWNT). The first acquirement of nanotubes was reported by Iijima in 1991 [13] who utilized the arc-discharge method to create nanotubes. Several Years later, two different methods to synthesize nanotubes by either laser-ablation [16] or catalytical [17] method were developed. The chemical vapor deposition (CVD) with catalyst-assistance method is most widely adopted to synthesize carbon nanotubes today, since it can produce nanotubes with few or free defects. Typically, SWNTs are 1−2 nanometers in diameter and few micrometers in length, as shown in figure 2(a); for other specific applications, aligned SWNTs up to millimeter long have also been reported [18]. The diameters of MWNTs are usually in the range of 2-25 nanometers and several tens of micrometers in length (figure 2(b)). In addition, vertical MWNT forests (figure 2(c)) also have attracted a lot of interests in applications of inter-connect or as microfluidic devices; they can be grown up to several centimeters in length [19]. In this thesis, we focus on individual SWNT synthesized by CVD method with catalyst-assistance.

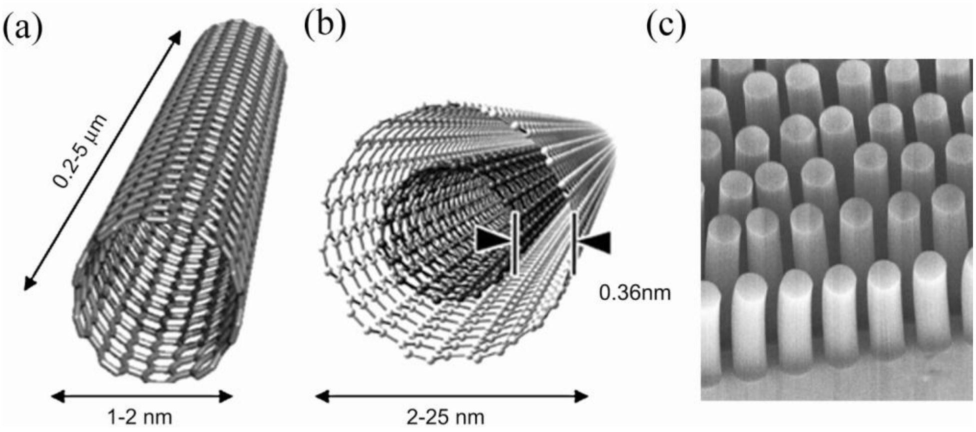

Figure 1.2. Different types of carbon nanotubes. (a) Single-walled carbon nanotube (b) Multi-walled carbon nanotube (c) Carbon nanotube forests. (www. wikipedia.com)

1.3.2 Graphene

Similar to nanotubes of single-walled and multi-walled forms, graphene can also be classified as single-layer, bilayer, and few-layers graphene. To distinguish the number of layers, one can simply place graphene on an oxidized Si substrate (SiO_2=285 nm) to compare the contrast of graphene through the optical microscope [15], as shown in figure 1.3(a). The area with lighter color indicates single- or bilayer graphene. For more precise discrimination, one can measure the Raman spectrum of graphene and compare the ratio of G to 2D peaks [20] (figure 1.3(b)) to determine the layer numbers. To create graphene, three distinct approaches have been employed so far. The first method is the mechanical exfoliation of graphite, which is also known as the "Scotch tape" or peeling-off method [15]. In this approach, graphene sheets are obtained by repeatedly peeling off graphite with scotch tape. The second one is the CVD epitaxial growth, by which graphene film is synthesized by decomposing methane (CH_4) on a metal (Ni, Cu, Ru) substrate [21-22] at high growth temperature. The third one is epitaxial growth on electrically insulating surface (SiC) at very high temperature (usually 1200~1600 ^{0}C) [23]. The principle of this method relies on that sublimation rate of silicon is higher than that of carbon; thus excess carbon atoms are left behind on the surface and rearrange to form graphene.

The mechanical exfoliation of graphites and CVD epitaxial growth on metal substrates are most common methods adopted to obtain graphene. The mechanical exfoliation method yields small-area graphene sheets but with high quality since this method can avoid contaminations and chemical residues resulting from the fabrication and solution process. However, the main drawback of exfoliation method is that it can only produce small graphene pieces, leading to it useful only in the laboratories for fundamental study. To produce large-scale graphene films, the CVD epitaxial growth on metal substrates is thought as a much feasible method. The growth of single-layer and bilayer graphene films up to wafer-scale on metal substrates has been demonstrated [24-26]. The main challenge of CVD method is the homogeneity of graphene films. In addition, since the graphene films are grown on metal substrates, an additional process step – transferring graphene from metal substrates to device substrates –is required for fabricating graphene devices. This transferring step may cause undesired contamination and chemical residues on the graphene films, degrading the quality of graphene films. Another serious concern is the wrinkle caused by the difference of thermal conductivity between the graphene and metal substrates. It may induce unwanted defects on the surface of graphene. In this thesis, we synthesized both single-layer and bilayer graphene on copper foils by CVD epitaxial method [25].

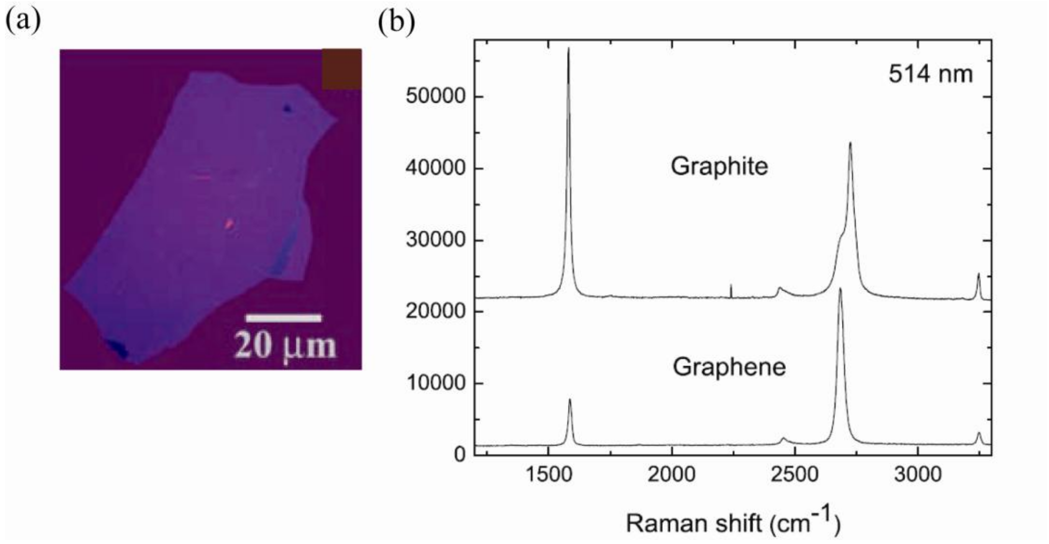

Figure 1.3. Methods of determining layer numbers of graphene sheets. (a) Comparing color contrast through the optical microscope: the area with lighter color represents fewer layers [15]. (b) Raman spectrum of graphene and graphite. The G peak is at ~1580 cm^{-1} and 2D peak is at ~2700 cm^{-1}. The ratio of intensity of G peak to 2D peak shows obvious difference for graphene and graphite [20].

1.4 Electrical properties of carbon nanotubes and graphene

1.4.1 Band structures

Graphene is a 2D monolayer composed of carbon atoms arranged in a hexagonal structure (figure 1.4(a), left panel). The structure can be viewed as a triangular lattice with a basis of two atoms per unit cell. The lattice vectors a_1 and a_2 are written as:

$$a_1 = \frac{a}{2}(3, \sqrt{3}), \quad a_2 = \frac{a}{2}(3, -\sqrt{3}) \tag{1.1}$$

, where a =1.42 Å is the nearest carbon-carbon distance. The reciprocal-lattice vectors are then given by:

$$b_1 = \frac{2\pi}{3a}(1, \sqrt{3}), \quad b_2 = \frac{2\pi}{3a}(1, -\sqrt{3}) \tag{1.2}$$

In figure 1.4(a) (right panel), two points K and K’ named ‘Dirac points’ at the corners of the Brillouin zone (BZ) of graphene are particularly important for the band structure of graphene. The energy dispersion relation of graphene simulated by the tight-binding model is illustrated in figure 1.4(b). The Dirac points are where conduction band and valence band meet at energy E= 0 corresponding to the Fermi energy. The linear energy dispersion shows that graphene is a gapless semimetal and charges in graphene are massless Dirac fermions.

Since nanotubes can be thought as formed by rolling up graphene, thus we can expect that nanotubes inherit their remarkable electrical properties from graphene. Rolling graphene to form nanotubes with diameters of few nanometers, the quantum confinement of electrons will result in the quantization of K values and produce unusual electrical properties related to the one dimensional transport. As a consequence, the band structure of a nanotube is equivalent to slicing the corn band structure of graphene at given K values, as shown in figure 1.4(c), showing nanotubes are either metallic or semiconducting [27].

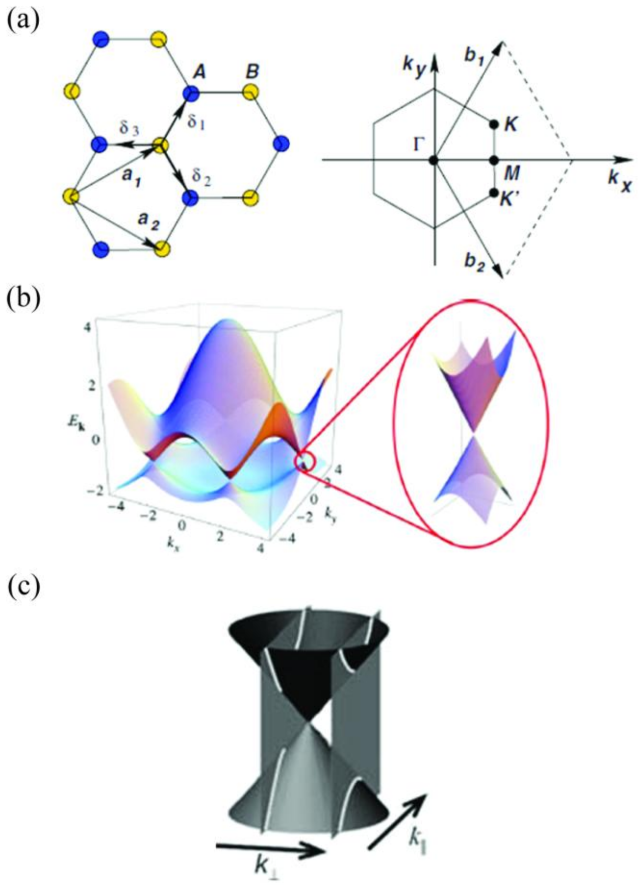

Figure 1.4. Band structures of graphene and carbon nanotubes. (a) Honeycomb lattice and its Brillouin zone. Left panel: a_1 and a_2 are lattice vectors. Right panel: b_1 andb_2 are reciprocal-lattice vectors and K and K' are Dirac points at the corners of Brillouin zone of graphene. (b) Linear energy dispersion of graphene. The conduction band and valence band meet at energy $E= 0$ corresponding to the Fermi energy. (c) Band structure of nanotube is equivalent to slicing the corn band structure of graphene at given K values [14, 27].

More specifically, a carbon nanotube can be specified by a set of two numbers (n, m) that determines the chirality of nanotube. These quantities are defined from the honeycomb lattice of graphene in figure 1.5(a). The chiral vector is $\boldsymbol{C_h} = n\boldsymbol{a_1}+m\boldsymbol{a_2} = (n, m)$ and the chiral numbers n, m are integers ($0 \leq |m| \leq n$). a_1 and a_2 are the lattice vectors same as mentioned in figure 1.4(a). The length of the unit vectors is *a*, and we can express the diameter of a nanotube as:

$$d = \frac{|C_h|}{\pi} = \frac{a}{\pi}\sqrt{n^2 + m^2 + nm} \tag{1.3}$$

Metallic carbon nanotubes are obtained when the difference *n*-*m* is a multiple of 3 [27], and the rest are semiconductive nanotubes. So statistically, there should be twice as many semiconductors as there are metals. The chiral angle from the figure 1.5 (a) is defined with the expression:

$$\cos\theta = \frac{\vec{C}_h \cdot \vec{a}_1}{|\vec{C}_h||\vec{a}_1|} = \frac{2n + m}{2\sqrt{n^2 + m^2 + nm}} \tag{1.4}$$

Depending on the chiral angle with respect to the lattice, the relative arrangement of the atoms in the wall of a nanotube with respect to the axis is different. As a result, nanotubes can be further classified as "armchair" carbon nanotubes ($\theta = 30^0$), "zigzag" carbon nanotubes ($\theta = 0^0$), and "chiral" carbon nanotubes (θ is arbitrary), as shown in figure 1.5 (b).

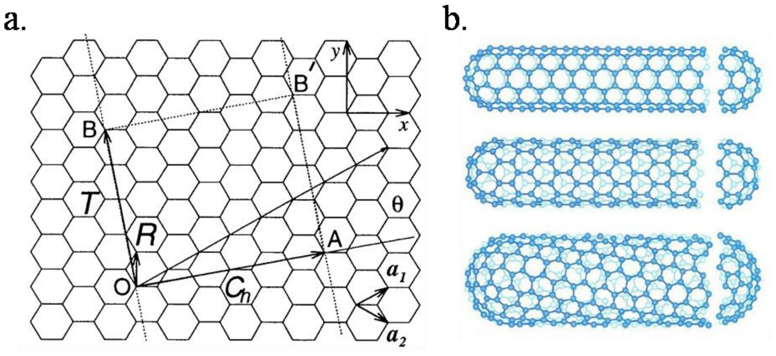

Figure 1.5. Structures of carbon nanotubes. (a) A nanotube is constructed by connecting the sites *O* to *A* and *B* to *B'*. The vectors *OA* and *OB* define the chiral vector $\boldsymbol{C_h}$. The chiral angle θ is measured with respect to the standard direction given in the figure (zigzag direction). (b) From top to bottom are an "armchair" carbon nanotube ($\theta = 30^0$), a "zigzag" carbon nanotube ($\theta = 0^0$), and a "chiral" carbon nanotube (θ is arbitrary), respectively [28].

1.4.2 Band gap

The biggest difference between metals and semiconductors is that semiconductors have band gap, allowing the field-effect transistors (FET) made out of semiconductors able to switch off. This switch-off behavior is important for modern integrated circuits. Nanotubes can be either metallic or semiconductive determined by their chiral vectors, and the band gap of semiconductive nanotubes can be predicted by the band theory with $E_g = 0.7/d$ (eV), where d is the diameter of nanotubes in nanometers [29]. On the other hand, for metallic nanotubes, most still have small band gap (typically less than 100 meV) due to perturbations such as curvature, strain, and twist on the nanotubes. The three-terminal conductance measurement is widely adopted to provide a direct means to identify semiconductive or metallic nanotubes (see next transistor subsection).

Graphene is a semimetal with zero band gap as shown in figure 1.6(i) [30], meaning that FETs with channels made out of large-area single layer graphene cannot be switched off. Thus, graphene FETs are limited for being applied in integrated circuits. To overcome this disadvantage, three distinct approaches to modify the band structure of graphene for opening band gap were proposed. The first method is to form graphene nanoribbons (GNRs) by constraining large-area single-layer graphene into one dimension [31-33]. The second one is by biasing bilayer graphene with dual-gate configurations [34-36] and the third one is to apply strain to graphene sheets [37].

Theoretically, both two types of nanoribbons, armchair and zigzag nanoribbons, are predicted to have band gap (figure 1.4 (ii)) and the opening of band gap is approximately estimated proportional to the inverse of the nanoribbons' width [32]. In addition, the band gap opening of nanoribbons has been demonstrated experimentally for the width down to 1 nm as well. Theory and experiments both show band gap in excess of 200 meV [31-32]. Moreover, bilayer graphene is also gapless, and its valence and conduction bands have a parabolic shape near the K point, as shown in figure 1.4 (iii). When an electrical field is applied perpendicular to the bilayer graphene, band gap opens due to symmetry broken and the bands near the K point take on the so-called Mexican-hat shape, as shown in figure 1.4 (iv). The band gap opening was predicted by theory [34] and has been verified in experiments [35-36].

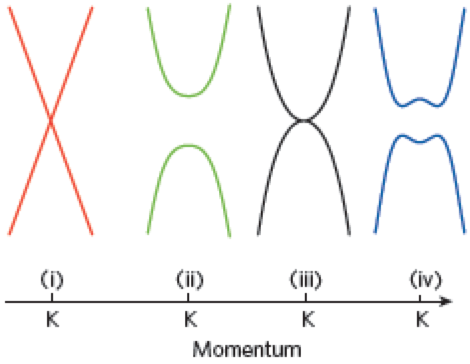

Figure 1.6. Band gap opening of graphene. Band structure around the *K* point of (i) large-area single-layer graphene, (ii) graphene nanoribbons, (iii) unbiased bilayer graphene, and (iv) bilayer graphene with an applied perpendicular electrical field [30].

1.4.3 Carbon nanotube and graphene transistors

A general FET consists of a gate, a channel (usually made out of semiconductive materials) connecting source and drain electrodes, and an insulating layer separating the gate from the channel (figure 1.7(a)) [38]. The operation of a FET is simply by applying a gate voltage to control conductivity of the channel, and thus the drain current. For high-speed operations, FETs should respond quickly to the variations in gate voltages (V_{GS}) and the fast response requires a short gate and fast carriers in the channel. In other words, thin channel and high carrier mobility are preferred. The high mobility and thin thickness own by nanotubes and graphene make them potential candidates applied in high-speed nanoelectronics. The first nanotube FET was carried out in 1998 [39], and high-speed nanotube FET operating in gigahertz was demonstrated in 2004 [40]. In 2004, the observation of field effect in graphene was first reported [15], and then the first graphene transistor was fabricated in 2007 [41]. Year later, graphene FET operating in gigahertz was reported [42] as well.

The operation of nanotube or graphene FET is analogous to the metal-oxide-semiconductor field-effect transistors (MOSFET). Here, a three-terminal nanotube transistor illustrated in Fig. 1.7(a) is taken as an example to describe the basic operation. The position of the Fermi level in a semiconductive nanotube can be tuned capacitively by the gate voltages. Negative (positive) charges built up in the nanotube are induced when positive (negative) voltages applied on the gate electrode. The additional charges will change the position of the valence and conduction bands relative to the Fermi level in the nanotube. As a consequence, the position shifting of Fermi level will modify the nanotube conductance. There are three different operation regimes when different gate voltages are applied (figure 1.7(b)). For a typical nanotube FET, nanotubes are usually *p-type* doped with excess positive charges. The p-type doping is due to the underlying oxide and various absorbates on the surface of nanotubes. As applying negative gate voltages, the Fermi energy is inside the valence band and the transport is due to the holes; thus this operation region is called “p-regime”. When gate voltages are 0~5V, the Fermi energy is in the band gap and the transport through the nanotube is “off”, which is called band-gap regime. For gate voltages larger than 5V, the Fermi energy will be shifted to the conduction band and the transport is due to electrons, which is called “n-regime” as shown in figure 1.7(c).

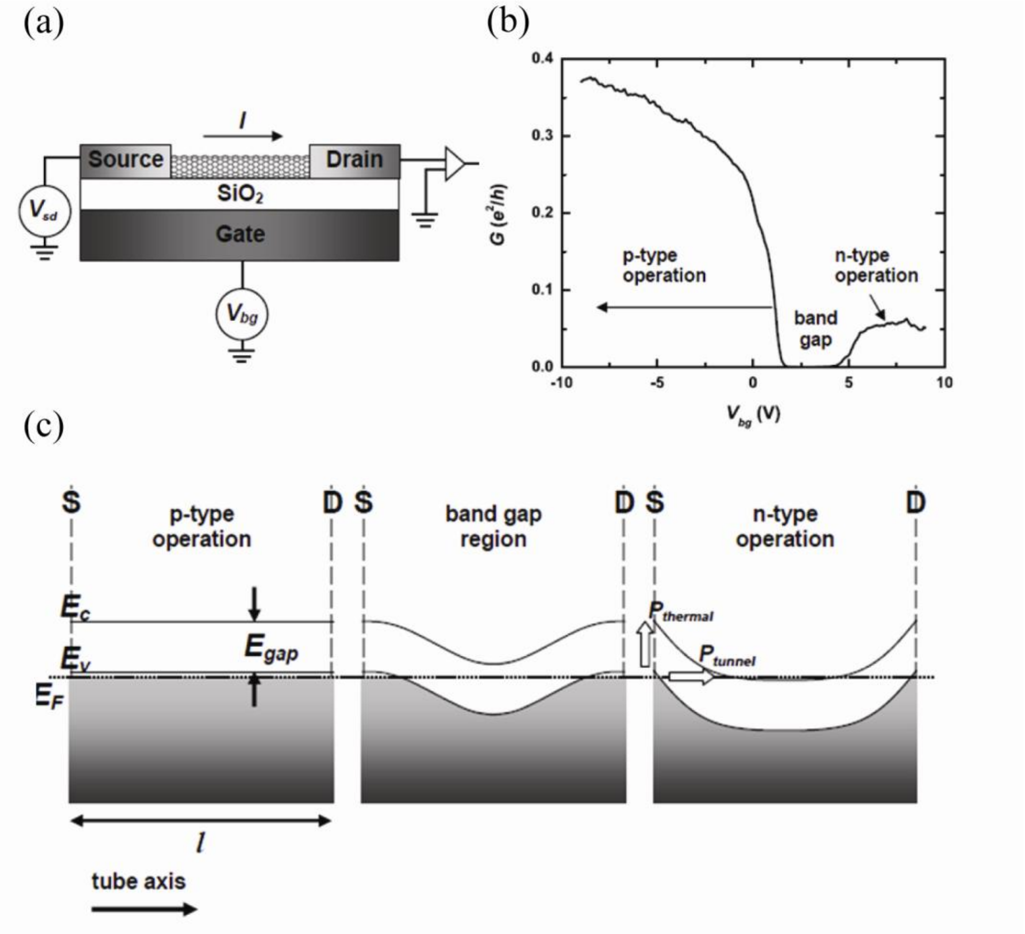

Figure 1.7. Operation of a carbon nanotube FET. (a) Schematic of a carbon nanotube FET. (b) Conductance vs. V_{bg} at the p-type, band gap and n-type regimes are illustrated. The maximum n-type conductance is less than the maximum p-type conductance. This is mainly due to tunneling barriers for electrons in the n-region. Since the contacts (Pd in this case) are typically p-type, there is no barrier for holes in the p-region. (c) Band diagram of p-type, band gap, and n-type operation regimes [38].

1.5 Mechanical properties of carbon nanotubes and graphene

In terms of mechanical properties, nanotubes and graphene are the one of stiffest materials due to sp^2 hybridized carbon-carbon bond. This remarkable mechanical property is characterized by the Young's modulus (E). It has been demonstrated that the Young's modulus of both nanotubes and graphene can reach ~1TPa [43-45], roughly 10 times greater than the steel. Besides, they are also expected to withstand large strains of up to 6~10%. Moreover, the strength of carbon-carbon bond makes them quite flexible and able to return to their original shape after bending. This excellent mechanical property leads them to be applied in many fascinating applications. For example, flexible, high-aspect-ratio nanotube atomic force microscope (AFM) tips and nanotweezers have been demonstrated [46-47].

Another unique mechanical property is that nanotubes and graphene are not piezoelectric materials. Piezoelectric effect is that the strain caused by the deformation will induce a voltage across the material and this effect is reversible. For nanotubes, an electrical effect has been observed: the charges injected to nanotubes will cause the nanotubes to elongate or shrink and it has advantages over piezoelectric effect. It can achieve strains greater than 1% (10 times larger than piezoelectrics), operate at high temperature and be achieved by few volts rather than hundreds. Utilizing this electric effect, nanotube based nonvolatile random-access memory (NRAM) has been proposed [48]. The basic NRAM cell is composed of two nanotubes: one nanotube is suspended over another one perpendicularly. This NRAM cell can store a bit of information due to the bistable property. In the "on" state, the nanotubes will contact with each other; when it is "off", both nanotubes are separated. The switch between "on" and "off" states are conducted by applying opposite (same) parity of voltages on nanotubes. Since the states of a NRAM cell are switched mechanically, it does not encounter the problem of charge storage suffered by a conventional RAM and makes it is a very promising candidate as high-speed memory.

The last mechanical property we would like to discuss is the change of band gap induced by strain. As mentioned in previous section, induced-strain is one of three approaches proposed for band gap opening of graphene. So far, this method has been extensively studied and the effect of uniaxial strain on the band structure has been simulated [37]. However, the simulation result shows that it is possible to open the band gap by inducing strain but it requires a global uniaxial strain exceeding 20%, which is difficult to achieve in practice. Moreover, little is known about if other types of strain will influence the band structure of graphene and more studies are needed to clarify these uncertainties.

For nanotubes, their band structure is determined by the chiral vectors and the chirality is directly related to the bond length. Therefore, when a strain is induced, it will change the bond length and the periodicity of boundary condition, eventually leading to the change of band structure to decrease or increase the band gap. It has been predicted theoretically [49-50] that it is possible to modify the band gap of a semiconducting nanotube and induce a band gap in metallic tubes by applying strain on them. In addition, it has been experimentally shown that the band gap (E_g) of a semiconductive nanotube can be tuned by applying a small mechanical strain, σ [51] as

$$\frac{dE_g}{d\sigma} \approx \pm 100 \frac{meV}{\%} \cos 3\phi \tag{1.5}$$

, where ϕ is the chiral angle and the sign up front depends on the exact wrapping vectors.

1.6 Previous works on carbon nanotube and graphene resonators

1.6.1 Carbon nanotube resonators

The first nanotube resonator was made out of MWNTs for the purpose of measuring the elastic modulus of nanotubes [52], and the experiment setup is illustrated in figure 1.8(a). A DC voltage was applied on the nanotube to induce charges on it, and the nanotube was placed in an oscillating electric field created by applying an AC voltage to a nearby electrode. The motion of nanotube was actuated by this oscillating electrical field when the oscillating frequency matches the natural resonance frequency of nanotube. The motion of nanotube was then detected by using transmission electron microscope (TEM) [52] or scanning electron microscope (SEM) [53]. Later, another approach was proposed by using nanotube as a field emitter [54] to measure its resonance frequency. The nanotube was actuated electrically and the resonance frequency was determined by measuring the emission current. However, although both methods successfully detected the resonance of nanotube, a couple of issues were resulted from. First, to detect the resonance by using TEM or SEM, or applying few hundred volts to create emission current is unrealistic for any industrial application. Secondly, electron beams used for imaging in TEM and SEM will damage nanotubes both structurally and electrically. In addition, the sensitivities obtained by these methods are poor and limit further studies on nanotube resonators. To this end, an electrical method in conjunction with the concept of mixing technique has successfully actuated and detected nanotube resonators simultaneously on a single chip [55], as shown in figure 1.8(b). This approach simplifies the measurement setup, increases the measurement sensitivity significantly and has been widely adopted by the subsequent works based on nanotube resonators [56-60]. Thereafter, researchers were continuously developing different methods in detecting the resonance of nanotube resonators. For example, the mechanical detection of nanotube resonators' vibration has been demonstrated in air at atmospheric pressure by means of a novel scanning force microscopy (SFM) method [61]. The vibration of fundamental mode and higher eigenmodes was successfully imaged then.

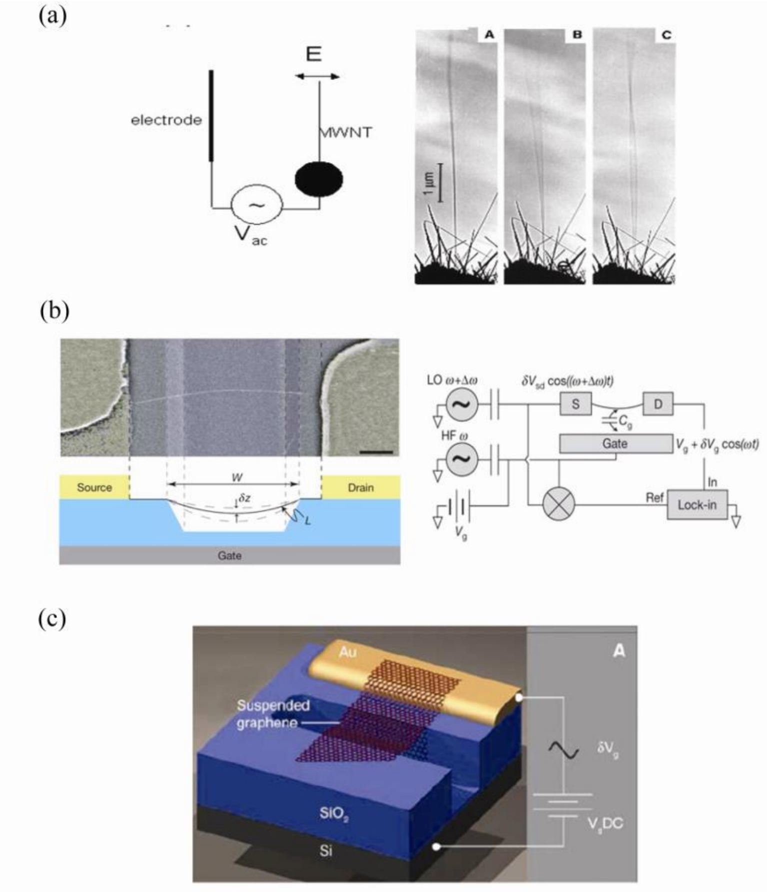

Figure 1.8. Previous works on carbon nanotube and graphene resonators. (a) Experimental schematic done by [52] and images of first and second harmonics of vibrating nanotube cantilevers. (b) Device geometry and diagram of experimental setup done by [55]. (c) First graphene mechanical resonators done by [65].

Due to their low mass and high Young's modulus, nanotube resonators are expected to have ultrahigh resonance frequency. Nanotube resonators operating at

GHz have been implemented, showing their potentials applied in radio frequency (RF) circuits [56, 61]. Furthermore, the minimum detected mass of nanotube resonators at sub-attogram level were also demonstrated [57-60]. In addition, they were also used to study the quantum theories. For instance, cooling nanotube resonators to the phononic state with a constant electron current was demonstrated experimentally [62] and the mechanical vibration coupled the charge transport at low temperatures was also realized [63-64]. However, even though a host of works based on CNT resonators have been demonstrated so far, there are still some challenges left. Firstly, the conventional process techniques to fabricate nanotube devices result in unwanted contaminations and damages on nanotubes and limit their further applications. Thus, a simple process technique to fabricate ultraclean nanotube electronics is much desired. Secondly, the fundamental operations of nanotube resonators are still not fully explored, such as frequency tuning mechanisms and nonlinear dynamics. Lastly, the biggest challenge is to improve their low quality factors, which limit their sensitivity in sensing applications significantly. The low quality factor is attributed to several intrinsic dissipations and a potential solution will be to seek an external way to enhance the low quality factor.

1.6.2 Graphene resonators

The first graphene resonator was demonstrated by the Cornell group in 2007 [65]. It was fabricated by placing a mechanical exfoliated graphene sheet on the pre-patterned structure, as shown in figure 1.8(c). The resonance of graphene resonators was measured by using interferometry method, while the graphene beam was actuated through thermal expansion/extraction caused by shining the graphene sheet with a laser beam and detected by measuring the reflected light intensity with another laser source. Later, the UAB group applied radio frequency voltages to electrostatically drive the suspended graphene sheets into motion and detect the mechanical vibrations by using scanning probe microscopy, which allowed identification and spatial imaging of the shape of the mechanical eigenmodes [66]. Though both methods successfully detected the resonance frequencies of graphene resonators, a self-detecting scheme is still preferred. To this end, the Columbia group adopted the measurement setup used in measuring nanotube resonators to detect graphene resonators [67]. Utilizing this electrical approach relies on the strong gate response of conductivity of single-layer graphene. Their results show the feasibility of actuating and detecting resonance on a single chip and open up the possibility of graphene resonators applied in other fields. Later, the Columbia group further simplified the measurement scheme to actuate and detect the mechanical motion directly by using a vector network analyzer [68].

In the meantime, the Cornell group also tried to fabricate graphene resonators by replacing the exfoliated graphene with either graphene grown on SiC substrate or by CVD method [69-71]. Those resonators showed similar characteristics of low quality factor values (~100) at room temperature. The actual dissipations causing low Q are still unclear currently and spurious edge mode, clamping loss, and interlayer friction were suggested [72-74]. To figure out the possible damping in graphene resonators, the Cornell group changed the beam geometry by fabricating drum-like graphene resonators and obtained Q up to ~2400. The improvement of Q is believed due to the elimination of spurious edge mode [75]. Recently, nonlinear damping is demonstrated to play an important role in determining Qs of nanotube and graphene resonators [76]. However, more work are still needed in order to fully explore the behind mechanisms. In addition, like nanotube resonators, graphene resonators are also considered as good mechanical sensors in detecting mass, gas and strain [77-79]. So far, only very few works based on graphene resonators have been reported. Many interesting issues such as quality factor enhancement, nonlinear dynamics, and single-molecule sensing are still waiting for being explored.

1.7 Summary and outline of the thesis

Carbon nanotubes and graphene are materials with excellent electrical and mechanical properties. Their nanometer cross section, high stiffness, great flexibility, and transistor properties make them ideal blocks in NEMS. We are therefore interested in carbon based NEMS resonators and focus on their fundamental operations. Chapter 2 gives a short introduction regarding NEMS and beam theory. In addition, the origins of dissipations occurring in resonators and the conventional measurement setups are also included. Chapter 3 describes our unique one-step direct transfer process technique to fabricate pristine SWNT nanoelectronics. Using this process technique, both SWNT resonators and suspended SWNT p-n diodes are demonstrated. Chapter 4 describes the capacitive spring softening effect in SWNT resonators and the differentiation of vibrational modes. Chapter 5 presents parametric amplification in SWNT resonators, which allows us to enhance the quality factors of SWNT resonators at least 10 times and obtain the highest Q reported at room temperature. Chapter 6 presents our ongoing work on graphene resonators. The ability to synthesize large areas of both single-layer and bilayer graphene films with well homogeneity allows us to systematically study the graphene resonators. Lastly, we propose the future research directions of graphene resonators including exploring the loss mechanisms and realizing parametric amplification for Q enhancement in graphene resonators.

REFERENCE

[1]C. Liu, "*Foundations of MEMS"*, Prentice Hall (2005).

[2]G. T. A. Kovacs, "*Micromachined Transducers Sourcebook"*, McGraw Hill (1998).

[3]H. G. Craighead, "*Nanoelectromechanical systems*", Science **290**, 1532 (2000).

[4]M. Roukes, "*Nanoelectromechanical systems face the future*", Phys. World **14**, 25 (2001).

[5]A. N. Cleland, "*Foundations of Nanomechanics"*, Springer-Verlag , Berlin (2003).

[6]K. L. Ekinci, and M. L. Roukes, "*Nanoelectromechanical systems*", Rev. Sci. Instrum. **76**, 061101 (2005).

[7]A. N. Cleland, and M. L. Roukes, "*Noise processes in nanomechanical resonators*", J. Appl. Phys. **92**, 2758 (2002).

[8]K. L. Ekinci, X. M. H. Huang, and M. L. Roukes, "*Ultrasensitive nanoelectromechanical mass detection*", Appl. Phys. Lett. **84**, 4469 (2004).

[9]K. L. Ekinci, Y. T. Yang, and M. L. Roukes, "*Ultimate limits to inertial mass sensing based upon nanoelectromechanical systems*", J. Appl. Phys. **95**, 2682 (2004).

[10]Y. T. Yang *et al.*, "*Zeptogram-scale nanomechanical mass sensing*", Nano Lett. **6**, 583 (2006).

[11]A. K. Naik *et al.*, "*Towards single-molecule nanomechanical mass spectrometry*", Nat. Nanotech. **4**, 445 (2009).

[12]J. R. H. H. W. Kroto, S. C. O'Brien, R. F. Curl, & R. E. Smalley, "*C_{60}: Buckminsterfullerene*", Nature **318**, 162 (1985).

[13]S. Iijima, "*Helical microtubules of graphitic carbon*", Nature **354**, 56 (1991).

[14]A. K. Geim, and K. S. Novoselov, "*The rise of graphene*", Nat. Mater. **6**, 183 (2007).

[15]K. S. Novoselov *et al.*, "*Electric field effect in atomically thin carbon films*", Science **306**, 666 (2004).

[16]T. Guo *et al.*, "*Self-assembly of rubular fullerenes*", J. Phys. Chem. **99**, 10694 (1995).

[17]J. Kong *et al.*, "*Synthesis of individual single-walled carbon nanotubes on patterned silicon wafers*", Nature **395**, 878 (1998).

[18]S. M. Huang, X. Y. Cai, and J. Liu, "*Growth of millimeter-long and horizontally aligned single-walled carbon nanotubes on flat substrates*", J. Amer. Chem. Soc. **125**, 5636 (2003).

[19] H. W. Zhu *et al.*, "*Direct synthesis of long single-walled carbon nanotube strands*", Science **296**, 884 (2002).

[20]A. C. Ferrari *et al.*, "*Raman spectrum of graphene and graphene layers*", Phys. Rew. Lett. **97**, 187401 (2006).

[21] P. W. Sutter, J. I. Flege, and E. A. Sutter, "*Epitaxial graphene on ruthenium*", Nat. Mater. **7**, 406 (2008).

[22]X. S. Li *et al.*, "*Large-area synthesis of high-quality and uniform graphene films on copper foils*", Science **324**, 1312 (2009).

[23]E. Rollings *et al.*, "*Synthesis and characterization of atomically thin graphite films on a silicon carbide substrate*", J. Phys.& Chem. Solids **67**, 2172 (2006).

[24]K. S. Kim *et al.*, "*Large-scale pattern growth of graphene films for stretchable transparent electrodes*", Nature **457**, 706 (2009).

[25]S. Lee, K. Lee, and Z. H. Zhong, "*Wafer scale homogeneous bilayer graphene films by chemical vapor deposition*", Nano Lett. **10**, 4702 (2010).

[26]Y. Lee *et al.*, "*Wafer-scale synthesis and transfer of graphene films*", Nano Lett. **10**, 490 (2010).

[27]M. J. Biercuk *et al.*, "*Electrical transport in single-wall carbon nanotubes"*, Carbon Nanotubes **111**, 455 (2008).

[28] R. Saito, "*Physical properties of carbon nanotubes"*, Imperial College Press (1998).

[29]M. D. Dresselhaus, G. Dresselhaus and P. Avouris, "*Carbon nanotubes: synthesis, structure properties and applications"*, Springer-Verlag, Berlin (2001).

[30]F. Schwierz. "*Graphene transistors*", Nat. Nanotech. **5**, 487 (2010)

[31]M. Y. Han *et al.*, "*Energy band-gap engineering of graphene nanoribbons*", Phys. Rev. Lett. **98**, 206805 (2007).

[32]L. Yang *et al.*, "*Quasiparticle energies and band gaps in graphene nanoribbons*", Phys. Rev. Lett. **99**, 186801 (2007).

[33]X. L. Li *et al.*, "*Chemically derived, ultrasmooth graphene nanoribbon semiconductors*", Science **319**, 1229 (2008).

[34]E. V. Castro *et al.*, "*Biased bilayer graphene: Semiconductor with a gap tunable by the electric field effect*", Phys. Rev. Lett. **99**, 216802 (2007).

[35]T. Ohta *et al.*, "*Controlling the electronic structure of bilayer graphene*", Science **313**, 951 (2006).

[36]Y. B. Zhang *et al.*, "*Direct observation of a widely tunable bandgap in bilayer graphene*", Nature **459**, 820 (2009).

[37]V. M. Pereira, A. H. C. Neto, and N. M. R. Peres, "*Tight-binding approach to uniaxial strain in graphene*", Phys. Rev. B **80**, 045401 (2009).

[38] S. Rosenblatt. "*Pushing the limits of carbon nanotube transistors*", Doctoral Thesis, Cornell Uunivesity, Ithaca, NY

[39]S. J. Tans, A. R. M. Verschueren, and C. Dekker, "*Room-temperature transistor based on a single carbon nanotube*", Nature **393**, 49 (1998).

[40]S. D. Li *et al.*, "*Carbon nanotube transistor operation at 2.6 GHz*", Nano Lett. **4**, 753 (2004).

[41]M. C. Lemme *et al.*, "*A graphene field-effect device*", IEEE Electr. Device Lett. **28**, 282 (2007).

[42]Y. M. Lin *et al.*, "*Operation of graphene rransistors at gigahertz frequencies*", Nano Lett. **9**, 422 (2009).

[43]A. Krishnan *et al.*, "*Young's modulus of single-walled nanotubes*", Phys. Rev. B **58**, 14013 (1998).

[44]C. Gomez-Navarro, M. Burghard, and K. Kern, "*Elastic properties of chemically derived single graphene sheets*", Nano Lett. **8**, 2045 (2008).

[45]C. Lee *et al.*, "*Measurement of the elastic properties and intrinsic strength of monolayer graphene*", Science **321**, 385 (2008).

[46]P. Kim, and C. M. Lieber, "*Nanotube nanotweezers*", Science **286**, 2148 (1999).

[47]J. Li, A. M. Cassell, and H. J. Dai, "*Carbon nanotubes as AFM tips: Measuring DNA molecules at the liquid/solid interface*", Surf. Interface Anal. **28**, 8 (1999).

[48]T. Rueckes *et al.*, "*Carbon nanotube-based nonvolatile random access memory for molecular computing*", Science **289**, 94 (2000).

[49]R. Heyd, A. Charlier, and E. McRae, "*Uniaxial-stress effects on the electronic properties of carbon nanotubes*", Phys. Rev. B **55**, 6820 (1997).

[50]L. Yang *et al.*, "*Band-gap change of carbon nanotubes: Effect of small uniaxial and torsional strain*", Phys. Rev. B **60**, 13874 (1999).

[51]E. D. Minot *et al.*, "*Tuning carbon nanotube band gaps with strain*", Phys. Rev. Lett. **90** (2003).

[52]P. Poncharal *et al.*, "*Electrostatic deflections and electromechanical resonances of carbon nanotubes*", Science **283**, 1513 (1999).

[53]R. P. Gao *et al.*, "*Nanomechanics of individual carbon nanotubes from pyrolytically grown arrays*", Phys. Rev. Lett. **85**, 622 (2000).

[54]S. T. Purcell *et al.*, "*Tuning of nanotube mechanical resonances by electric field pulling*", Phys. Rev. Lett. **89**, 276103 (2002).

[55]V. Sazonova *et al.*, "*A tunable carbon nanotube electromechanical oscillator*", Nature **431**, 284 (2004).

[56]H. B. Peng *et al.*, "*Ultrahigh frequency nanotube resonators*", Phys. Rev. Lett. **97**, 087203 (2006).

[57]K. Jensen, K. Kim, and A. Zettl, "*An atomic-resolution nanomechanical mass sensor*", Nat. Nanotech. **3**, 533 (2008).

[58]B. Lassagne *et al.*, "*Ultrasensitive mass sensing with a nanotube electromechanical resonator*", Nano Lett. **8**, 3735 (2008).

[59]H. Y. Chiu *et al.*, "*Atomic-scale mass sensing using carbon nanotube resonators*", Nano Lett. **8**, 4342 (2008).

[60]C. Hierold *et al.*, "*Nano electromechanical sensors based on carbon nanotubes*", Sens. Actuators A **136**, 51 (2007).

[61]D. Garcia-Sanchez *et al.*, "*Mechanical detection of carbon nanotube resonator vibrations*", Phys. Rev. Lett. **99**, 085501 (2007)

[62]S. Zippilli, G. Morigi, and A. Bachtold, "*Cooling carbon nanotubes to the phononic ground state with a constant electron current*", Phys. Rev. Lett. **102**, 096804 (2009).

[63]B. Lassagne, "*Coupling mechanics to charge transport in carbon nanotube mechanical resonators*, Science **325**, 1107 (2009).

[64]G. A. Steele *et al.*, "*Strong coupling between single-electron tunneling and nanomechanical motion*", Science **325**, 1103, (2009).

[65]J. S. Bunch *et al.*, "*Electromechanical resonators from graphene sheets*", Science **315**, 490 (2007).

[66]D. Garcia-Sanchez *et al.*, "*Imaging mechanical vibrations in suspended graphene sheets*", Nano Letters **8**, 1399 (2008).

[67]C. Y. Chen *et al.*, "*Performance of monolayer graphene nanomechanical resonators with electrical readout*", Nat. Nanotech. **4**, 861 (2009).

[68]Y. H. Xu *et al.*, "*Radio frequency electrical transduction of graphene mechanical resonators*", Appl. Phys. Lett. **97**, 243111 (2010).

[69]S. Shivaraman *et al.*, "*Free-standing epitaxial graphene*", Nano Lett. **9**, 3100 (2009).

[70]A. M. van der Zande *et al.*, "*Large-scale arrays of single-layer graphene resonators*", Nano Lett. **10**, 4869 (2010).

[71]J. S. Bunch *et al.*, "*Impermeable atomic membranes from graphene sheets*", Nano Lett. **8**, 2458 (2008).

[72]C. Seoanez, F. Guinea, and A. H. Castro, "*Dissipation in graphene and nanotube resonators*", Phys. Rev. B **76**, 125427 (2007).

[73]S. Y. Kim, and H. S. Park, "*The importance of edge effects on the intrinsic loss mechanisms of graphene nanoresonators*", Nano Lett. **9**, 969 (2009).

[74] S. Y. Kim, and H. S. Park, "*Multilayer friction and attachment effects on energy dissipation in graphene nanoresonators*", Appl. Phys. Lett. **94**, 101918 (2009).

[75] R. A. Barton *et al.*, "*High, size-dependent quality factor in an array of graphene mechanical resonators*", Nano Lett. **11**, 1232 (2011).

[76] A. Eichler *et al.*, "*Nonlinear damping in mechanical resonators made from carbon nanotubes and graphene*", Nat. Nanotech. **6**, 339 (2011).

[77] A. Sakhaee-Pour *et al.*, "*Applications of single-layered graphene sheets as mass sensors and atomistic dust detectors"*, Solid State Commun.**145**, 168 (2008).

[78] B. Arash, Q. Wang, and W. H. Duan, "*Detection of gas atoms via vibration of graphenes*", Phys. Lett. A **375**, 2411 (2011).

[79] A. Sakhaee-Pour, M. T. Ahmadian, and A. Vafai, "*Potential application of single-layered graphene sheet as strain sensor*", Solid State Commun. **147**, 336 (2008).

CHAPTER 2

REVIEW OF NANOELECTROMECHANICAL SYSTEMS

2.1 Introduction

NEMS are emerging technologies over the last decade and evolving continuously with the progress of lithography and material synthesis. They are considered as MEMS scaled down to submicron dimensions, and the shrink of dimensions brings out the reduction of the system’s effective mass, directly leading to the increase of resonance frequency and the decrease of the system’s force constant. These specific properties straightly translate into high sensitivity to the surroundings, low operating power consumption and more possibilities of applications employed with their nonlinear properties. So far, they have been served in many unprecedented applications [1-3] and used for fundamental studies of classic and quantum physics [4]. In this chapter, we will briefly introduce the development of NEMS to date [5-6].

In general, NEMS can be depicted as generic multi-terminal electromechanical systems, as shown in figure 2.1. The electrical input signals are transduced as mechanical stimulus to stimulate the mechanical system and the mechanical response are converted to electrical signals by the output transducers. Additional electrical control signals can be applied to perturb the mechanical system in order to change its properties, such as resonance frequency and quality factor. Various types of device geometries have been employed in NEMS today and the three most common seen geometries, cantilevers (singly-clamped beam) [7], doubly-clamped beams [8], and paddles (torsional resonators) [9] are illustrated in figure 2.2, respectively. In this thesis, we adopted the doubly-clamped beam structure to fabricate carbon nanotube and graphene nanoelectromechanical resonators

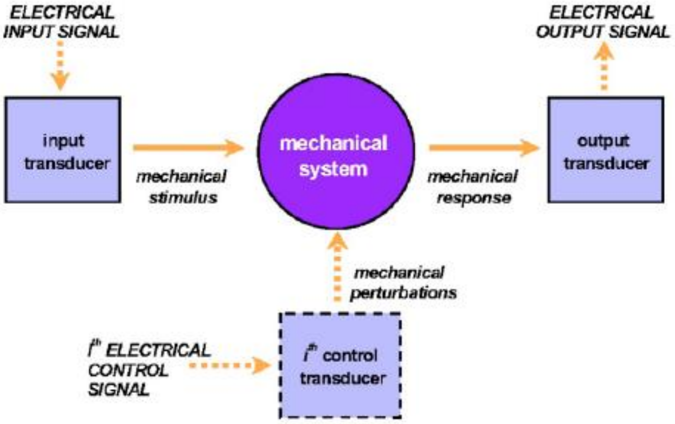

Figure 2.1. Schematic of a multi-terminal nanoelectromechanical system. Electrical input signals are transduced as mechanical stimulus to excite the system and mechanical responses are converted to output electrical signals. Additional electrical control signals can be applied to perturb the mechanical system in order to change its parameters [5].

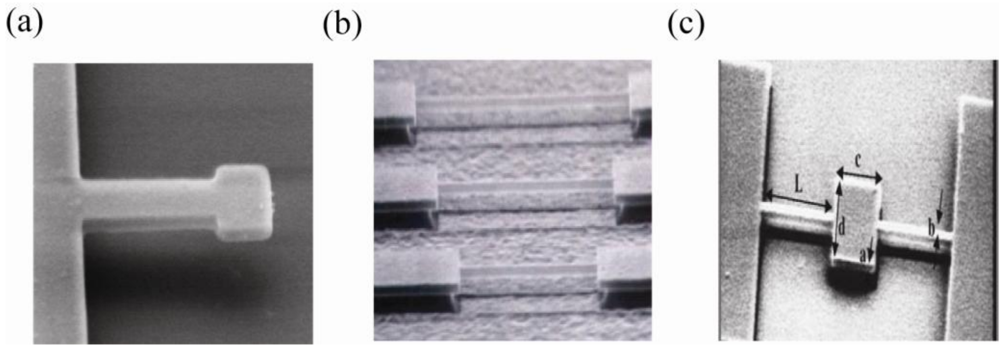

Figure 2.2. Various types of NEMS resonators. (a) A cantilever (singly-clamped beam) [7] (b) Doubly-clamped beams [8] (c) A paddle (torsional resonator) [9].

The resonance frequency of MEMS resonators can be calculated by using molecular dynamics (MD) simulation and it has been proven that these calculations are still valid even when structure sizes are reduced down to nanoscale [10]. Thus, the fundamental resonance frequency of a doubly-clamped beam NEMS resonator can be expressed [11]:

$$f_0 = \frac{\omega_0}{2\pi} = 1.05\sqrt{\frac{E}{\rho}}\left(\frac{h}{L^2}\right) \tag{2.1}$$

, where E is the elastic modulus, ρ is the mass density of the beam, and h and L are the thickness and length of the beam, respectively (see section 2.3 for details). Basically, the behavior of a mechanical resonator in the linear operation regime can be approximated by using a simple harmonic oscillator (SHO). As a result, the SHO model is first introduced in section 2.2 to illustrate the basic operation of mechanical resonators. Following the SHO section, beam mechanisms and nonlinear dynamics based on doubly-clamped beam resonators are presented in section 2.3 for further discussion.

To actuate and detect the resonance of NEMS resonators, various techniques, such as optical interferometry and magnetomotive have been utilized [12-13]. In section 2.4, we will briefly describe these two measurement schemes. Then, in section 2.5, we will focus on a capacitive approach in conjunction with the mixing technique to actuate and detect the motion of nanotube and graphene resonators electrostatically [14-15].

The minimum operation energy for a system is defined as the energy which drives the system is comparable to the thermal fluctuations (k_BT) and can be estimated as

$$P_{min} = k_BT\omega_0/Q \tag{2.2}$$

, where k_B is the Boltzmann constant, T is the temperature in Kelvin, ω_0 is the resonance frequency and Q is the quality factor. Large Q means low operating power level and high attainable sensitivities. For NEMS device dimensions made out via e-beam lithography today, the minimum power level is usually in the order of attowatts [5].

The quality factors of typical NEM resonators are in the range of 10^3-10^5, which are much higher than those usually available with electronic oscillators. A distributing trend in the quality factors of resonators as a function of resonators' volume has been noticed [5]. As the cross-section area further shrinks down to several nanometers, the quality factors decrease below 1000. The quality factors are affected by various loss mechanisms and will be discussed in section 2.6. High operating frequencies with low power consumption and high quality factors have made NEMS promising for a variety of fascinating applications. Two emerging applications will be described in section 2.7.

2.2 Simple harmonic oscillators

A SHO is a well-studied model, and broadly adopted in both classic and quantum physics. In addition, it is also the basic to understand the operation of any resonance systems. A common example of a SHO is a massless spring with a spring constant k and a mass m attached to it, as shown in figure 2.3(a). For small displacements, the spring follows Hooke's law, $F = kx$, where x is the displacement from the equilibrium. If x describes the position of the mass, the equation of motion is given by:

$$m\ddot{x}(t) + kx(t) = 0 \qquad (2.3)$$

The solution of the equation (2.3) is in the form of:

$$x(t) = x_0 \cos(\omega_0 t + \phi) \qquad (2.4)$$

, where $\omega_0 = \sqrt{k/m}$ is the resonance frequency of the system, and x_0 and ϕ are the amplitude and the phase of the motion, respectively. In reality, a damping term related to the velocity of the mass (*dx/dt*) and a driving force term should be included. The equation of motion then can be modified as:

$$m\ddot{x}(t) + b\dot{x}(t) + kx(t) = F_0 \cos(\omega t) \tag{2.5}$$

, where b is the damping coefficient, the driving force is assumed sinusoidal, and F_0 is the force amplitude. The steady solution to the modified motion equation is:

$$x(t) = \frac{F_0 / m}{\sqrt{(\omega_0^2 - \omega^2)^2 + 4\omega^2\beta^2}} \cos(\omega t - \phi), \tag{2.6}$$

$$\phi = \arctan(\frac{\omega_0^2 - \omega^2}{2\omega\beta}) \tag{2.7}$$

, where

$$\beta = b / 2m \tag{2.8}$$

$$\omega_0 = \sqrt{k / m} \tag{2.9}$$

Considering the damping in the system, the quality factor is defined in terms of the total energy divided by the energy loss in the system:

$$Q = 2\pi(\frac{Total\ Energy}{Energy\ lost\ during\ one\ period}) \tag{2.10}$$

Therefore, we have $Q=\omega_0/2\beta$ and $b=m\omega_0/Q$ and equation (2.5) can be rewritten as:

$$m\ddot{x}(t) + \frac{m\omega_0}{Q}\dot{x}(t) + kx(t) = F_0 \cos(\omega t) \tag{2.11}$$

Figure 2.3(b) shows the frequency dependence of the amplitude and the phase of the response. The amplitude reaches maximum at the resonance frequency (f = 50), where the value is Q times higher than the non-resonance response. The frequency dependence of the amplitude is in the form of a Lorentzian shape and the width of half maximum is given by $\Delta\omega=\omega_0/Q$. In addition, the phase of the signal goes through 180^0 phase shift.

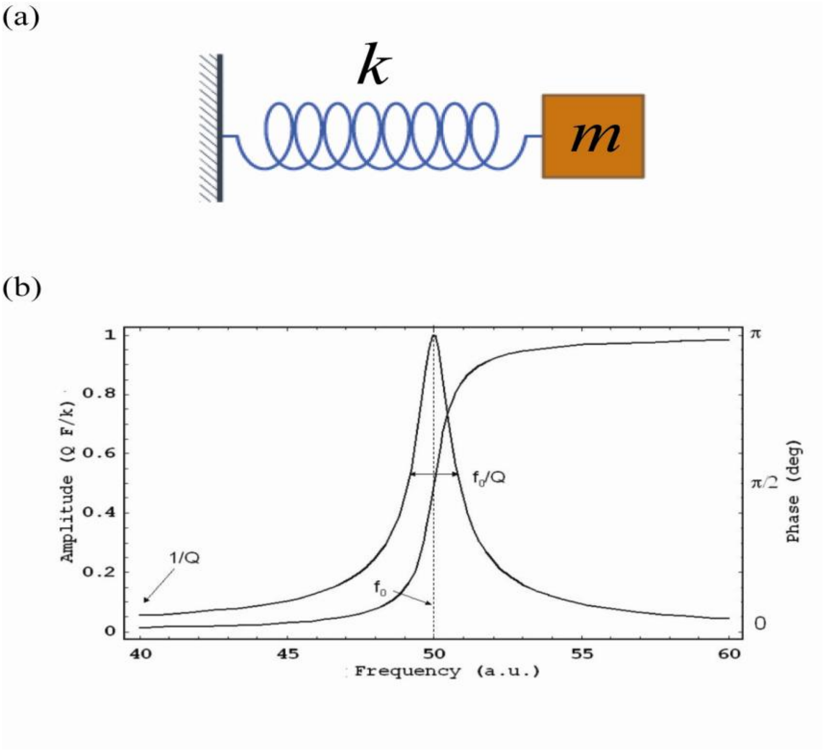

Figure 2.3. A simple harmonic oscillator. (a) A SHO has a massless spring with a spring constant *k* and a mass *m* attached to it. (b) The amplitude and the phase of the SHO response are plotted as a function of the driving frequency. The maximum amplitude at the resonance frequency is *Q* times larger than the off-resonance response. At the same time the phase of the response goes through 180^0 shift [20].

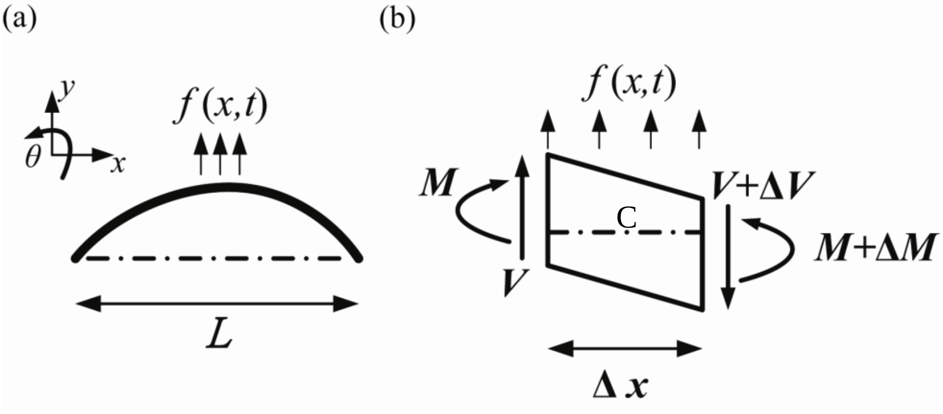

Figure 2.4. Lateral vibration of a beam. (a) Schematic of a bending beam. (b) Force acting on an element.

2.3 Beam mechanisms

2.3.1 Euler-Bernoulli beam equation

Consider a beam of length *L* subjected to an external force $f\,(x,\,t)$ per unit length, as shown in figure 2.4(a). Assume the beam vibrates laterally and its vertical displacement in the *y* direction is denoted as $u_y\,(x,\,t)$. The forces acting on an infinitesimal element are depicted in figure 2.4(b), where $M\,(x,\,t)$ is the bending moment and $V\,(x,\,t)$ is the shear force. If the beam has a Young's modulus *E*, a mass density ρ, a cross sectional area A and moment of inertia *I* about the axis perpendicular to the plane *x-y*, according the Newton's second law, the net forces and the moment equation at point C are given by:

$$\sum F_y = m\ddot{u}_y \tag{2.12}$$

$$\sum M_C = 0 \tag{2.13}$$

, where *m* is the mass of the element equal to $\rho \mathrm{A}\Delta x$ and $\ddot{u}_y$ is the acceleration in the *y* direction. Summing the forces in figures 2.4(b), equation (2.12) becomes:

$$-(V+\Delta V)+f\Delta x+V=\rho A\Delta x\frac{\partial^2 u_y}{\partial t^2} \tag{2.14}$$

Applying the moment equation at point C, equation (2.13) becomes:

$$(M+\Delta M)-(V+\Delta V)\Delta x+f\Delta x\frac{\Delta x}{2}-M=0 \tag{2.15}$$

For an infinitesimal Δx, ΔV and ΔM are approximated as:

$$\Delta V=\frac{\partial V}{\partial x}\Delta x, \qquad \Delta M=\frac{\partial M}{\partial x}\Delta x \tag{2.16}$$

Substitute equation (2.16) into equation (2.14) and (2.15) and ignore higher order term:

$$-\frac{\partial V}{\partial x}+F=\rho\, A\frac{\partial^2 u_y}{\partial t^2} \tag{2.17}$$

$$\frac{\partial M}{\partial x}-V=0 \tag{2.18}$$

Substitute equation (2.18) into equation (2.17), then it yields:

$$-\frac{\partial^2 M}{\partial x^2}+F=\rho\,A\frac{\partial^2 u_y}{\partial t^2} \tag{2.19}$$

From Euler-Bernoulli beam theory, the bending moment M is given by:

$$M=EI\,\frac{\partial^2 u_y}{\partial x^2} \tag{2.20}$$

Substitute equation (2.20) into equation (2.19), and the equation of motion is obtained:

$$EI\,\frac{\partial^4 u_y}{\partial x^4}+\rho\,A\frac{\partial^2 u_y}{\partial t^2}=F \tag{2.21}$$

For free vibration, F=0, then the equation reduces to:

$$EI\,\frac{\partial^4 u_y}{\partial x^4}+\rho\,A\frac{\partial^2 u_y}{\partial t^2}=0 \tag{2.22}$$

Solving equation (2.22) with the method of separation of variables $u_y(x, t)=U(x)T(t)$

$$\frac{c^2}{U}\frac{\partial^4 U}{\partial x^4}=-\frac{1}{T}\frac{\partial^2 T}{\partial t^2}=a=\omega_n^2, \qquad c=\sqrt{\frac{EI}{\rho A}} \tag{2.23}$$

The general solution $U(x)$, which is called the normal mode, is in the form:

$$U(x)=C_1\cos\beta x+C_2\sin\beta x+C_3\cosh\beta x+C_4\sinh\beta x, \tag{2.24}$$

, where C_1, C_2, C_3, and C_4 are constants and $\beta=\omega_n^2/c$.

$$\omega_n=\frac{(\beta_n L)^2}{L^2}\sqrt{\frac{EI}{\rho A}}=\frac{K_n^2}{L^2}\sqrt{\frac{EI}{\rho A}}, \quad K_n=4.73, 7.853, ..n=1,2.. \tag{2.25}$$

Since the moment of inertia for a beam with a rectangular cross section is $I = bh^3/12$, where b is the width and h is the thickness, then $f_0=\omega_0/2\pi$ can be rewritten as:

$$f_0=\alpha\frac{h}{L^2}\sqrt{\frac{E}{\rho}} \tag{2.26}$$

, where α is 1.05 for doubly-clamped beams and 0.162 for cantilevers [11].

In reality, tension in the beam has to be included. For a tensile tension, equation (2.22) then is written as:

$$EI\frac{\partial^4 u_y}{\partial x^4}+\rho A\frac{\partial^2 u_y}{\partial t^2}=T\frac{\partial^2 u_y}{\partial x^2} \qquad (2.27)$$

,where T is the tension in the beam, which is composed of its inherent tension T_0 and the additional tension ΔT due to its bending that induces an extension ΔL in the length of the beam. ΔT is given by the strain, or $\Delta L/L$ multiplied by Young's modulus E and cross section area A. Therefore, equation (2.27) becomes:

$$EI\frac{\partial^4 u_y}{\partial x^4}+\rho A\frac{\partial^2 u_y}{\partial t^2}=\left[T_0+\frac{EA}{2L}\int_0^L\left(\frac{\partial u_y}{\partial x}\right)^2 dx\right]\frac{\partial^2 u_y}{\partial x^2} \qquad (2.28)$$

A general solution to equation (2.28) is:

$$\begin{aligned}u_y(x)=A[&(\sin k_nL-\sinh k_nL)(\cos k_nz-\cosh k_nz)\\&-(\cos k_nL-\cosh k_nL)(\sin k_nz-\sinh k_nz)]\end{aligned} \qquad (2.29)$$

And the fundamental resonance frequency (f) with tension being considered is

$$f=f_0\sqrt{1+\frac{TL^2}{3.4Eh^3}} \qquad (2.30)$$

, where f_0 is the fundamental frequency as expressed in equation (2.26). In addition, the tension can be compressive and under compressive tension, "+" is replaced by "-", which cause a decrease in resonance frequency.

2.3.2 Nonlinear dynamics in NEMS resonators

Nonlinear behaviors observed in NEMS resonators have attracted great interests over the last few years [16]. For a practical need, it is necessary to understand these behaviors in order to avoid them when they are unwanted and exploit them efficiently when they are helpful. The origins of nonlinearities may come from the effect of external potential or the device geometry, where the Duffing nonlinearity, αx^3, is induced. In addition, they may originate from the detection/actuation schemes due to practical reasons. In fact, the nonlinearity appears not only in the form of αx^3, but also possibly occurs in the damping mechanisms $x^2*(dx/dt)$, which has been demonstrated important in investigating nanotube and graphene resonators [17].

A. *Duffing resonators*

Modeling a mechanical resonator as a SHO is usually a good approximation, since most materials can sustain relatively large deformations without breaking away the stress-strain relation from a linear fashion. However, nonlinear behaviors may occur even before the intrinsic nonlinear regime is reached. As a consequence, they may enter the equation of motion in the form of a force which is proportional to the cube of the displacement αx^3, and will turn a SHO into a so-called Duffing resonator. Qualitatively speaking, the Duffing nonlinearity, αx^3, can be positive to assist the restoring force, making the resonator stiffer, and lead to the increase in resonance frequency. On the other hand, it can be negative as well, against the restoring force, letting the resonator softer, and reduce the resonance frequency. For a quantitative view, the equation of motion with Duffing nonlinearity included can be written as:

$$m\ddot{x}(t)+\frac{m\omega_0^2}{Q}\dot{x}(t)+kx(t)+\alpha x^3(t)=F_0\cos(\omega t) \tag{2.31}$$

, where α is given by [18]:

$$\alpha=\frac{E}{18\rho}\left(\frac{2\pi}{L}\right)^4 \tag{2.32}$$

The Duffing nonlinearity is proportional to the cube of the displacement, so for small displacement, it can be neglected and the response is still Lorentzian. As the driving amplitude increases, it starts to affect the response and above the critical amplitude (a_c), the peak is pulled to the higher frequency and a backbone curve shape appears, as shown in figure 2.5 (a). The critical amplitude, a_c, is the onset of the nonlinearity and expressed as [18]:

$$a_c = \omega_0 \sqrt{\frac{8}{3\sqrt{3}\alpha Q}} \qquad (2.32)$$

It has been demonstrated that the linear operation dynamic range (*DR*) is directly related to the critical amplitude, while small critical amplitude will lead to small useful linear dynamic range. It has also been further approved that the onset of this nonlinear regime decreases with decreasing diameter, while the thermomechanical noise increases with aspect ratio. So for nanotube and graphene resonators with high aspect ratio, the useful linear dynamic range is severely limited and result in that many applications will involve operation in the nonlinear regime.

B. Nonlinear damping in resonators

We further consider the effect of nonlinear damping ($x^2*(dx/dt)$) and include it in the equation of motion, and therefore the equation (2.31) is modified as:

$$m\ddot{x}(t) + \frac{m\omega_0^2}{Q}\dot{x}(t) + kx(t) + \alpha x^3(t) + \eta x^2 \dot{x}(t) = F_0 \cos(\omega t) \qquad (2.33)$$

, where η is the nonlinear damping coefficient. By solving equation (2.33) (see ref. [16] for details), we obtain the modified critical amplitude (a_c'), which is proportional to $\sqrt{\frac{1}{\sqrt{3}-\eta'}}$, where $\eta' = \frac{\eta\omega_0}{\alpha}$, and the magnitude of the response | a | is plotted as a function of driving frequency in figure 2.5 (b). In figure 2.5(b), the thin solid curve shows the response without any nonlinear damping ($\eta = 0$), which is similar to the curve shown in figure 2.5(a). The thin dotted curve shows the response without any linear and nonlinear damping included (Q^{-1}= 0, and η = 0). However, as the nonlinear damping is put into consideration, it will reduce the critical amplitude (the thick dotted curve shown in figure 2.5(b)). Since the linear dynamic range is directly related to the critical amplitude, reduce of critical amplitude caused by the nonlinear damping will lead to the decrease of useful linear operation range.

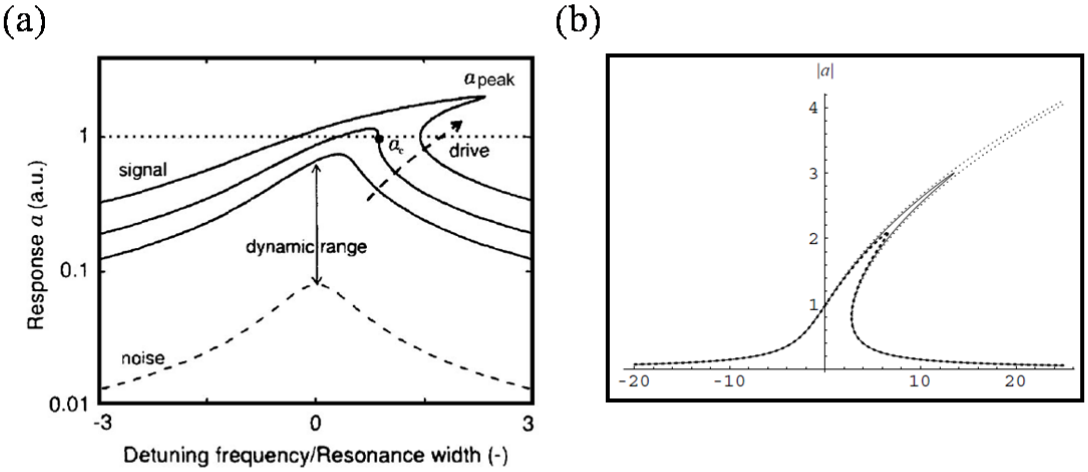

Figure 2.5. Nonlinear dynamics in NEMS resonators. (a) Duffing resonator response: amplitude response vs. driving frequency [18]. (b) Duffing resonator response with nonlinear damping term included [16]. The thin solid curve show the response without any nonlinear damping (η = 0). The thin dotted curve shows the response without any linear and nonlinear damping (Q^{-1}= 0, and η = 0). The thick dotted curve is the response with η not equal to zero, and we can see significant reduction of the critical amplitude.

2.4 NEMS measurement techniques

Optical, magnetomotive, and electrostatic (capacitive) measurement schemes have been widely adopted to measure the resonance of NEMS resonators. However, as the dimensions of resonators are scaled to nanometers, these methods somehow become difficult scalable. They are limited due to the diffraction of light or due to the effect of increasing parasitic capacitance for both magnetomotive and capacitive schemes. In this section, we briefly introduce the interferometry and magnetomotive schemes and leave the electrostatic setup discussed later in section 2.5.

2.4.1 Optical interferometry

The interferometry setup is illustrated in figure 2.6(a) [13, 19]. The intensity of a blue diode laser focused on the beam is modulated by a network analyzer, to cause a periodic contraction/expansion of the beam, then leading to motion. The vibration of the beam is then detected by monitoring the reflected light intensity from a second red laser with a high-speed photodiode. The main advantage of this approach is that the resonating structure does not require electrical contacts, while the disadvantage is that the effectiveness of driving a beam depends directly on the proximity of the laser spot to the structure and the thermal conductivity of the material. Therefore, when the resonators further shrink down, it is getting harder to realize this excitation scheme in measuring resonance.

2.4.2 Magnetomotive

To actuate the resonator, a conducting mechanical structure, usually a conducting loop such as a doubly-clamped beam, is placed in a static magnetic field (B), which is perpendicular to the plane of vibration, as shown in figure 2.6(b) [12]. With an AC current (I) passing through the beam, an AC Lorentz force ($F_{Lorentz} = IBL$; L is the beam length) is induced to drive the beam. The maximum vibration is expected to occur when the AC current frequency matches the natural resonance frequency. The motion of the beam is then detected by measuring the electromotive force (EMF) across the beam which is created when the flux enclosed in the conducting loop varies. The main drawback of this scheme is that for small resonators whose resistances are much higher than the impedance of the measurement circuit, the impedance mismatch makes it difficult to detect high frequency signals.

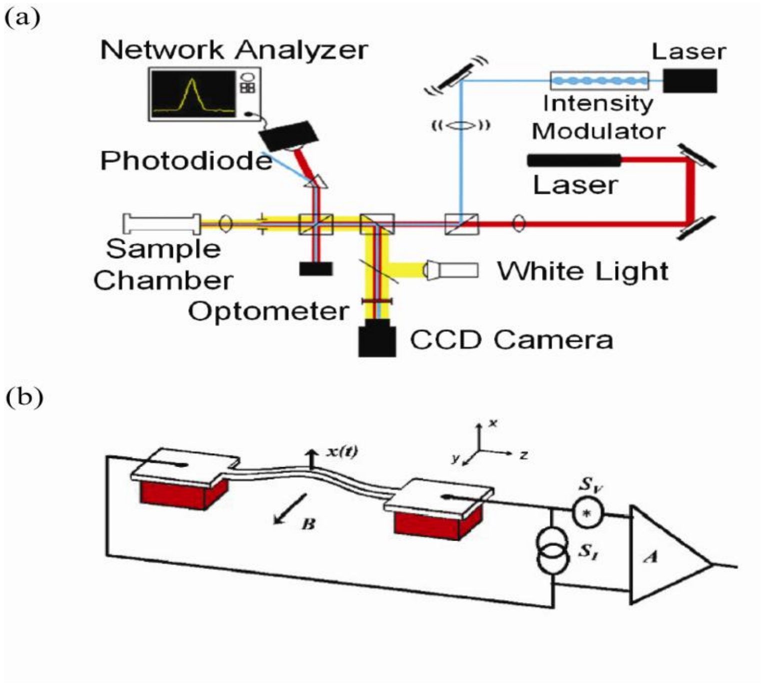

Figure 2.6. Two common NEMS measurement schemes. (a) Optical interferometry [19]: a blue laser is modulated by a network analyzer to cause contraction/expansion of the beam, then leading to motion. The vibration is detected by monitoring the reflected light intensity by using a second red laser with a high-speed photodiode. (b) Magnetomotive [12]: with an AC current passing through the beam, an AC Lorentz force is induced to drive the beam. The motion of the beam is detected by measuring the electromotive force across the beam.

2.5 Electrostatic (Capacitive) measurement scheme

Due to their extremely small cross-section, it is difficult to actuate and detect the carbon nanotube resonators' resonance by using conventional optical interferometry or magnetomotive techniques. To this end, an electrostatic measurement scheme in conjunction with the concept of mixing theory has been employed [14], which allows us to actuate and detect the resonance of nanotube resonators simultaneously on a single chip. Owing to its simplicity and sensitivity in detecting the resonance signals, we adopted this scheme for studying nanotube and graphene resonators in this thesis. Here, we summarize this technique in detail from previous work [20].

2.5.1 Actuation of carbon nanotube resonators

The motion of CNT is actuated through the electrostatic interaction between the tube and the underneath gate electrode. Appling gate voltage (V_g) will induce extra charges on the CNT given by $q = C_g V_g$, where C_g is the capacitance to the gate. As a result, an electrostatic force (F_{el}) is induced to pull down the CNT and expressed as:

$$F_{el} = \frac{1}{2} C_g^{'} V_g^2 \tag{2.34}$$

where C'_g is the derivative of C_g with respect to the distance between the CNT and gate. Modulating V_g with an AC voltage at frequency ω, the modulated $\tilde{V}_g$ is then:

$$\tilde{V}_g = V_g^{DC} + \tilde{V}_g \cos(\omega t) = V_g^{DC} + \tilde{V}_g^{\omega} \tag{2.35}$$

Substituting equation (2.28) into equation (2.27) and neglecting the higher order term, the electrostatic force is expressed as:

$$F_{el} \cong \frac{1}{2} C_g^{'} V_g^{DC} (V_g^{DC} + 2\tilde{V}_g^{\omega}) \tag{2.36}$$

From equation (2.36), F_{el} has two components: the DC term ($\frac{1}{2}C_g^{'}V_g^{DC^2}$) controlled by V_g^{DC} will increase the tension on the CNT and the AC term ($C_g^{'}V_g^{DC}\tilde{V}_g^{\omega}$) caused by $\tilde{V}_g^{\omega}$ will lead the CNT into motion. As driving frequency ω approaches the resonance frequency ω_0, the displacements become larger and reach the maximum as $\omega = \omega_0$.

2.5.2 Detection of resonance

To detect the motion of nanotube, we rely on its transistor properties. Since the conductance of nanotube is determined by the induced charge on it [18], therefore, the modulation in the induced charge ($\tilde{q}$) will lead to a modulation in the conductance, $\tilde{G} = (dG/dq)\tilde{q}$. The induced charge is modulated by either the applied AC gate voltage ($\tilde{V}_g^{\omega}$) or the capacitance to the gate ($\tilde{C}_g(\omega)$):

$$\tilde{q} = \tilde{C}_g(\omega)V_g^{DC} + C_g\tilde{V}_g^{\omega} \qquad (2.37)$$

, where the cross term is neglected since the amplitude of modulation is assumed small. If $Z(\omega)$ is the distance between the nanotube and the gate, Z_0 is the initial distance, and $z(\omega)$ is the vibration amplitude, then $Z(\omega)$ is express as:

$$Z(\omega) = Z_0 - z(\omega)\cos(\omega t) \qquad (2.38)$$

In addition, the modulated $\tilde{C}_g(\omega)$ caused by the nanotube's motion is approximated as:

$$\tilde{C}_g(\omega) = C_g^{'}z(\omega) \qquad (2.39)$$

Therefore, the conductance modulation due to the vibration of nanotube is:

$$\tilde{G} = \frac{dG}{dq}\tilde{q} = \frac{dG}{dq}C_g^{'}z(\omega)V_g^{DC} \qquad (2.40)$$

In equation (2.40), the conductance is modulated with the driving frequency and is proportional to the amplitude of vibration. The maximum conductance occurs as the driving frequency equals to the resonance frequency. However, for nanotube resonators with length in several μm, the resonance frequencies are around tens of megahertz. Thus, to measure the conductance modulation directly, we have to detect this small electrical signal at a high frequency out of a highly resistive device. High operating frequency and high resistance result in low readout frequency (only few hundreds of hertz), which is much smaller than its resonance frequency. To solve this difficulty, the concept of mixing technique is employed.

2.5.3 Mixing theory

In general, the mixing technique is to utilize a transistor as a mixer to up-convert or down-convert the signal frequency and this concept has been widely implemented in communications and RF circuits with Si-based transistors. Mixing technique based on nanotube transistors has also been demonstrated [22] and this nonlinearity in the I-V_g dependence solves the difficulty of detecting the resonance of nanotube resonators caused by the low readout frequency. The mixing theory is described briefly below:

If the conductance (G) of nanotube is modulated at frequency ω, G is then written as:

$$G = G^{DC} + \tilde{G}\cos(\omega t) = G^{DC} + \tilde{G}^{\omega} \tag{2.41}$$

And assume the source electrode is modulated at a slightly offset frequency $\omega+\Delta\omega$

$$\tilde{V}_{sd}^{\omega+\Delta\omega} = \tilde{V}_{sd}\cos((\omega+\Delta\omega)t) \tag{2.42}$$

Since the current I is the product of the V_{sd} and G, with equation (2.41) and (2.42) and without considering the current at LO frequency ($G^{DC}\tilde{V}_{sd}^{\omega+\Delta\omega}$), I is expressed as:

$$\begin{aligned} I = GV_{sd} = \tilde{G}^{\omega}\tilde{V}_{sd}^{\omega+\Delta\omega} &= \tilde{G}\cos(\omega t)\tilde{V}_{sd}\cos((\omega+\Delta\omega)t) \\ &= \tilde{G}\tilde{V}_{sd}\frac{1}{2}[\cos(\Delta\omega t) + \cos((2\omega+\Delta\omega)t)] \end{aligned} \tag{2.43}$$

In equation (2.43), the amplitude of the mixing current ($I^{\Delta\omega}$) at the intermediate frequency $\Delta\omega$ is equal to

$$I^{\Delta\omega} = \frac{1}{2}\tilde{G}\tilde{V}_{sd} = \frac{1}{2}\frac{dG}{dg}(C_g^{'} z(\omega)V_g^{DC} + C_g\tilde{V}_g)\tilde{V}_{sd} \qquad (2.44)$$

Since the intermediate frequency $\Delta\omega$ can be arbitrary small, this technique allows us to measure the amplitude of high frequency conductance modulations of nanotube by measuring the mixing current at frequencies that are within the readout bandwidth.

2.5.4 Measurement setup

There are three kinds of measurement setups used to implement the mixing concept. First one is called "two-source setup", where two RF signal generators and an external mixer are required. The second one is called "single-source setup", where the concept of amplitude modulation (AM) is utilized and only one signal generator is needed. Last is "DC mixing current setup", where the mixing current is measured in the DC level.

A. Two- source setup

The "two-source setup" is illustrated in figure 2.7(a). One RF signal is added to a DC V_g through a bias-T and applied to the gate. The AC signal (ω) applied on the gate is to drive the nanotube and the DC voltage is to increase the tension on the nanotube. The second RF signal ($\omega+\Delta\omega$) from the other RF generator is applied to the source for mixing. The mixing current through the nanotube is detected by a lock-in amplifier and the reference signal to the lock-in amplifier is provided by separately mixing these two RF signals by an external mixer. The lock-in amplifier can also serve as a low-pass filter to eliminate the high-frequency components from mixer. All voltages are given by

$$V_g = V_g^{DC} + \tilde{V}_g \cos(\omega t) \qquad (2.45)$$

$$V_{sd} = \tilde{V}_{sd}\cos((\omega + \Delta\omega)t + \phi) \tag{2.46}$$

, where ω, $\Delta\omega$, and ϕ are driving frequency, offset frequency and the gate-source phase difference, respectively.

B. Single-source setup

Single-source setup is to utilize the concept of effective gate voltage (V_g^{eff}) felt by the nanotube. This concept can be realized by performing AM within a single RF signal generator, which simplifies the measurement setup and reduces demands of instruments. V_g^{eff} felt by a nanotube is given by the voltage on the gate with respect to the potential of a nanotube, $V_g - V_{tube}$. If an AC signal is applied to the source, V_g^{eff} can be written as:

$$V_g^{eff} = V_g^{DC} - \frac{1}{2}\tilde{V}_{sd}^{\omega} \tag{2.47}$$

In equation (2.47), we found that it is not necessary to apply an AC signal on the gate to actuate the nanotube. In principle, both driving signal (V_{sd}^{ω}) and the mixing signal ($V_{sd}^{\omega+\Delta\omega}$) can be applied to the source. This significantly simplifies the setup because we can produce both signals with one RF signal generator by using its built-in AM capability, as shown in figure 2.7(b). AM at frequency $\Delta\omega$ with strength m for an arbitrary signal $A\cos(\omega t)$ is defined as:

$$\begin{aligned} V_{AM} &= (1 + m\cos(\Delta\omega t))A\cos(\omega t) \\ &= A\cos(\omega t) + \frac{Am}{2}\cos((\omega + \Delta\omega)t) + \cos((\omega - \Delta\omega)t) \end{aligned} \tag{2.48}$$

Therefore, if an AM signal is applied to the source electrode, it is equivalent to:

$$\tilde{V}_g^{\omega} = \tilde{V}_{sd}\cos(\omega t) \tag{2.49}$$

$$\tilde{V}_{sd}^{\omega+\Delta\omega} = \tilde{V}_{sd}\, m\cos((\omega + \Delta\omega)t) \tag{2.50}$$

$V_{sd}^{\omega+\Delta\omega}$ will mix with V_g^{ω} and produce a signal of the same phase and magnitude.

C DC mixing current measurement

In previous two setups, we measure the current signal at arbitrary small frequency $\Delta\omega$. This arbitrary $\Delta\omega$ can be very small even to be zero, meaning that we can measure the resonance signal in the DC level without a lock-in amplifier required. This also can be explained by expressing I_{sd} with a Taylor expansion.

$$I_{sd}(V_{sd}+\delta V)=I_{sd}(V_{sd})+\frac{\partial I_{sd}}{\partial V}\Big|_{V=V_{sd}}\cdot\delta V+\frac{\partial^2 I_{sd}}{\partial V^2}\Big|_{V=V_{sd}}\cdot\frac{(\delta V)^2}{2}+\ldots \tag{2.51}$$

For simplicity, V_{sd} can be zero and we have I_{sd}

$$I_{sd}(\delta V)=\frac{\partial I_{sd}}{\partial V}\Big|_{V=0}\cdot\delta V+\frac{\partial^2 I_{sd}}{\partial V^2}\Big|_{V=0}\cdot\frac{(\delta V)^2}{2}+\ldots=G\delta V+\frac{\partial G}{\partial V}\Big|_{V=0}\cdot\frac{(\delta V)^2}{2}+\ldots \tag{2.52}$$

If $\delta V=V_{ac}\cos(\omega t)$, *then*

$$\begin{aligned}I_{sd}(V_{ac},\omega)&=GV_{ac}\cos(\omega t)+\frac{\partial G}{\partial V}\Big|_{V=0}\cdot\frac{V_{ac}^2}{2}\cos^2(\omega t)\\&=\left(\frac{1}{4}\frac{\partial G}{\partial V}\Big|_{V=0}\cdot V_{ac}^2\right)+(GV_{ac})\cdot\cos(\omega t)+\left(\frac{1}{4}\frac{\partial G}{\partial V}\Big|_{V=0}\cdot V_{ac}^2\right)\cdot\cos(2\omega t)\end{aligned} \tag{2.53}$$

The DC mixing current term is

$$\left(\frac{1}{4}\frac{\partial G}{\partial V}\Big|_{V=0}\cdot V_{ac}^2\right) \tag{2.54}$$

This setup is much simpler than previous two since only one signal generator is required and no lock-in amplifier is needed. However, this setup has its own drawbacks: first, since the current amplifier will produce DC voltage, therefore it needs to be zeroed in order to distinguish the mixed current from the current due to this amplifier voltage. In addition, the noise level is higher at 1 KHz due to 1/f noise.

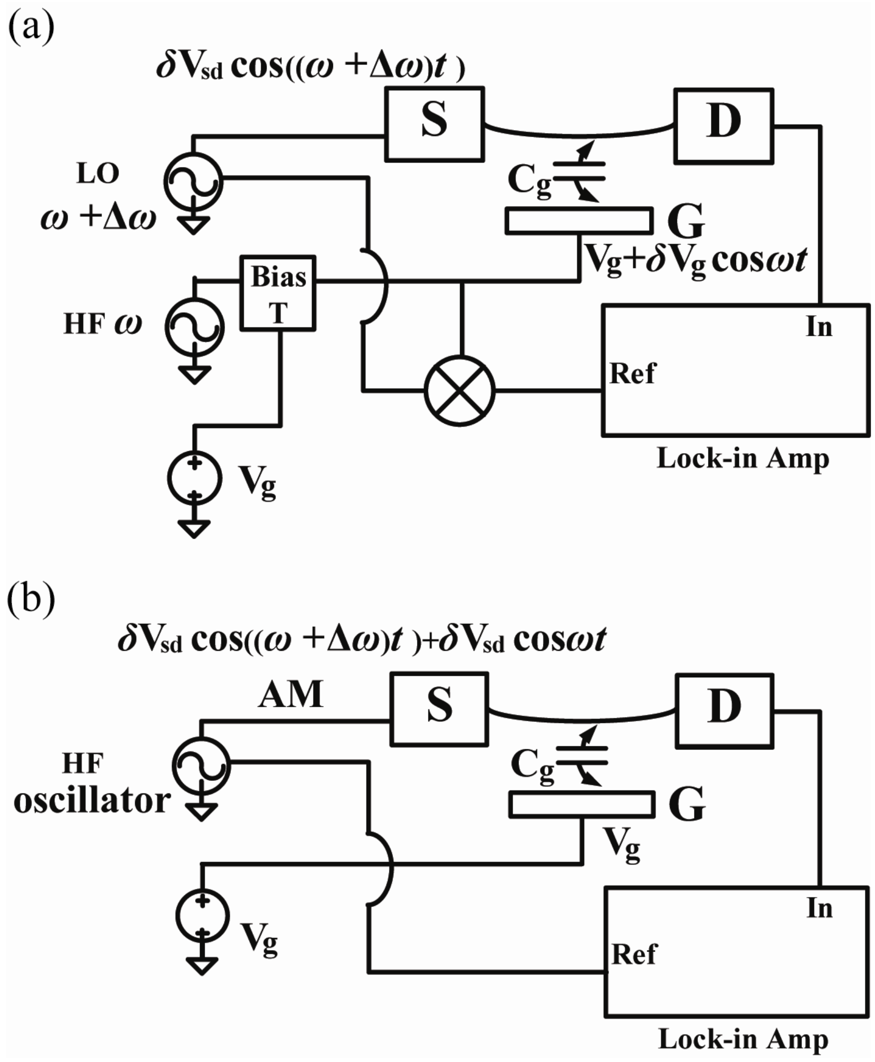

Figure 2.7. Electrostatic measurement setups of measuring nanotube resonators. (a) Two-source setup. Two high frequency signals are applied on the gate (HF) and on the source ((LO). A DC gate voltage is coupled with HF signal through a bias-T and connected to the gate. The mixing current is detected by the lock-in amplifier. The reference signal to the lock-in amplifier is provided by mixing these two high frequency signals with an external mixer. (b) Single-source setup. Both driving and mixing signals can be produced with one RF signal generator by using its built-in AM capability.

2.5.5 *Fitting the resonance frequency*

Once the mixing current is measured, the next step will be to extract the resonance frequency and quality factor from it. For the convenience, here we reproduce the mixing current $I^{\Delta\omega}$:

$$I^{\Delta\omega} = \frac{1}{2}\tilde{G}\tilde{V}_{sd} = \frac{1}{2}\frac{dG}{dq}(C_g^{'} z(\omega)V_g^{DC} + C_g\tilde{V}_g)\tilde{V}_{sd} \qquad (2.55)$$

, where $\tilde{V}_{sd}$ and $\tilde{V}_g$ are the AC voltages on the source and gate electrodes, respectively. C_g is gate capacitance, *dG/dq* is the transconductance, and $z(\omega)$ is the amplitude of vibration. In equation (2.55), the mixing current is the combination of two current sources. The first term called "I^{Peak}" is the current due to the mechanical vibration of the nanotube. The second term, I^{BG}, is the current due to the direct electrical modulation of the nanotube's potential by the AC gate voltage and is frequency independent. We can further derive $I^{Peak}(\omega)$ and $I^{BG}(\omega)$ with the solution to SHO and get:

$$I^{Peak}(\omega) = \frac{1}{2}\frac{dG}{dq}C_g^{'}V_g^{DC}\tilde{V}_{sd}\frac{z_0/Q}{\sqrt{(1-(\frac{\omega}{\omega_0})^2)^2 + (\frac{\omega/\omega_0}{Q})^2}} \qquad (2.56)$$

$$I^{BG}(\omega) = \frac{1}{2}\frac{dG}{dq}C_g\tilde{V}_g\tilde{V}_{sd} \qquad (2.57)$$

In principle, we could just add these two terms to form the total current. However, since these terms are from very different physical origins. The I^{Peak} comes from the electrons driven on and off of the nanotube due to the change in the potential in phase with the mechanical motion of the nanotube. The I^{BG} originates from the electrons moving on the nanotube due to the change in the potential in phase with voltages applied to the gate and source electrodes. Therefore, there is an arbitrary phase shift between these two terms, which causes them to interfere with each other [23]. Therefore, to fit with the total current, we have to add the peak and the background current contributions with a phase shift $\Delta\phi$ between them. The total current then can be written as:

$$I(\omega)=\frac{1}{2}\frac{dG}{dq}\left(C_g^{'}V_g^{DC}\frac{z_0}{Q}\frac{\cos(\Delta\phi+\arctan(\frac{\omega_0^2-\omega^2}{\omega\omega_0/Q}))}{\sqrt{(1-(\frac{\omega}{\omega_0})^2)^2+(\frac{\omega/\omega_0}{Q})^2}}+C_g\tilde{V}_g\right)\tilde{V}_{sd}$$

(2.58)

For further simplification, since the background current changes with driving frequency, for the frequency interval of the resonance, we can approximate its frequency dependence by a straight line. So I^{BG} can be expressed as

$$I^{BG}(\omega)=\frac{1}{2}\frac{dG}{dq}C_g\tilde{V}_g\tilde{V}_{sd}(A+B\omega) \qquad (2.59)$$

Substituting equation (2.59) into equation (2.58), total mixing current is expressed as the following form

$$I^{total}(f)=A+Bf+\frac{H\cos(\arctan(\frac{f_0^2-f^2}{\Gamma f}+\Delta\phi))}{\sqrt{(1-(\frac{f}{f_0})2)^2+(\Gamma\frac{f}{f_0})^2}} \qquad (2.60)$$

A, *B*, *H*, f_0, Γ and $\Delta\phi$ are independent fitting parameters. We can convert these fitting parameters into experimental parameters, such as the resonance frequency (f_0), quality factor (Q), I^{Peak}, and I^{BG} in the following fashion.

$$Q=\frac{f_0}{\Gamma} \qquad (2.61)$$

$$I^{Peak}=HQ \qquad (2.62)$$

$$I^{BG}=A+Bf_0 \qquad (2.63)$$

2.6 Losses

Quality factor is a major figure of merit for NEMS resonators. Firstly, the inverse of *Q* describes the energy loss in systems and is additive for different dissipation processes. Secondly, *Q* delivers the characteristics of NEMS resonators straightly. For example, the sensitivity of mass or force sensing is proportional to the inverse of *Q*, and the bandwidth of being a RF filter is also determined by *Q*. Typical NEMS resonators operate with *Qs* in the range of 10^3-10^5. However, as the cross-section area further shrinks down to few nanometers, *Qs* are usually below 100 and rarely exceed 1000. The variation of NEMS resonators' *Qs* is due to a variety of dissipations and these damping mechanisms have been extensively explored thus far. Therefore, it is worthwhile to discuss these dissipations here as studying NEMS resonators.

The sources of dissipations in NEMS resonators can be generally divided into two categories as either intrinsic or extrinsic dissipations. Intrinsic losses may come from defects and impurities within the lattice or from fundamental processes within the lattice such as phonon-phonon interactions and electron-phonon interactions. Extrinsic losses, such as gas friction, clamping loss, and surface loss are due to interactions with their surroundings. To improve *Q*, little can be done for intrinsic losses to control dissipation from these intrinsic sources rather than choosing resonator materials carefully. On the other hand, eliminating dissipation from the extrinsic sources is more realistic and feasible by lowering pressures or changing device geometries. Below several common intrinsic and extrinsic losses in NEMS resonators will be described. We also added comments on these losses to discuss their influence in determining *Qs* of nanotube resonators.

2.6.1 Intrinsic Losses

In a perfect crystal, the intrinsic dissipations come from fundamental processes in the lattice, such as phonon-phonon interactions and electron-phonon interactions. On the other hand, in a defected crystal, the losses are due to the defects and impurities in the lattice. These intrinsic dissipations, in principle, set the upper bounds of resonators' *Qs*, since little can be done to control these intrinsic losses. Here, we summarize some common intrinsic losses occurring in NEMS resonators and more thorough details can be found in [8, 24-26]. Many of these intrinsic losses can be calculated with a standard anelastic solid model [25]. The concept of this model is that mechanical vibration of a solid takes the system out of equilibrium. For an anelastic solid, this state is not stable, and the system tends to relax to its equilibrium through various mechanisms within a finite relaxation time. These relaxation mechanisms such as interaction with point-defects and thermal relaxation will lead to energy dissipation from the mechanical mode and is expressed:

$$Q^{-1} = \Delta\left(\frac{\omega\tau}{1+(\omega\tau)^2}\right) \tag{2.64}$$

, where ω is the mechanical vibration frequency and Δ is the mechanism-dependent dissipation strength and τ is the relaxation time.

A. Phonon-Phonon interactions

A real crystal is always aharmonic and this aharmonicity in the lattice causes the nonlinearity between the stress and strain in a solid, allowing the possibility of energy transfer between phonon-phonon scatterings. For a mechanical resonator with length *L*, it can be viewed as an acoustic mode with wavelength *L*. The energy transferring due to phonon-phonon scattering means that an acoustic mode can lose energy to higher energy thermal phonons. The phonon-phonon interaction can be further classified by comparing the mean free path (l_T) of thermal phonons to the wavelength of the acoustic mode. When l_T is comparable to L, the ballistic limit occurs. In this case, the losses to the resonator are due to individual scattering between the acoustic mode and thermal phonons, which is called *Landau-Rumer effect*. On the other hand, when $l_T \ll L$, diffusive limit occurs. The loss results from thermal phonons relaxing to equilibrium, which is called *Akhizer effect*. In this case, the phonons are viewed as a viscous "thermal gas" for the acoustic mode. The extreme diffusive case is called *thermoelastic effect*, in which phonons thermalize so fast that they can be thought as creating a temperature field. This temperature gradient provides a dissipation path for the system to dissipate energy, leading to loss. Thermoelastic effect is suggested a potential dissipation that results in low *Qs* of nanotube resonators and more details will be discussed in section 5.2.

B. Electron-Phonon interactions

Electron-phonon interaction occurs in metallic resonators. The mechanical motion of the resonator results in the ion oscillation and creates an oscillating electrical field. Therefore, the free electrons can be considered as a viscous gas that moves in this field and dissipates energy. The dissipation is calculated in the form [24]:

$$Q^{-1} = \frac{8}{15}\frac{E_F m_e \sigma\omega}{\rho v^2 e^2} \tag{2.65}$$

, where E_F is the Fermi energy, and e and m_e are the electron charge and electron mass, σ is the electric conductivity, ρ is the density, and v is the velocity of sound wave. From previous literature, *Qs* of nanotube resonators measured by both electrical and nonelectrical methods are consistently low at room temperature, suggesting moving electrons are not involved in producing dissipation. In addition, both metallic and semiconductive nanotube resonators show similar *Qs*. Therefore, it is reasonable that we can eliminate this damping source in nanotube resonators.

C. Two-level system

In general, internal defects include both surface defects and bulk defects. These defects can be contamination, intrinsic impurity atoms in the lattice and dangling or broken bonds on the surface. The dissipation caused by the internal defects is due to the acoustic phonon captured by these defects, which allows transition between two configurational minima. This mechanism can be addressed by using the formalism of two-level systems (TLS) [26]. The dissipation of a TLS with energy E has been calculated in two extreme cases:

$$Q^{-1} = C\frac{e^{-2E/kT}}{kT} \;@ E >> kT, \quad or \;\; Q^{-1} = \frac{d}{T^2} \;@ E << kT \qquad (2.66)$$

The dissipation caused by TLS in both nanotube and graphene resonators have been theoretically calculated [27]. The calculated dissipation (Q^{-1}) is around 10^{-22} which is much smaller than the experimental value, suggesting that we can ignore this effect when considering potential damping mechanisms in nanotube resonators.

2.6.2 Extrinsic Losses

A. Gas friction

The gas can be the dominant dissipation source for a resonator depending on the pressure inside the chamber. At high pressures (approximately above 1 torr), air can be considered as a viscous fluid. This viscous damping by the surrounding gas is expressed as $Q_{gas}^{-1} \sim \sqrt{p}$ [28]. Fortunately, it is easy to achieve lower pressures while viscous damping no longer dominates. At lower pressures, where the mean free path of the gas molecules is much larger than the length scale of the device, energy may still be dissipated through momentum transfer to individual molecule. In this case the dissipation is calculated to be [29]:

$$Q_{gas}^{-1} = \frac{pA}{M_{eff}\omega v} \qquad (2.67)$$

, where p is the pressure, A is the surface area, M_{eff} is the effective mass of the resonator, ω is frequency, and v is the thermal velocity of the gas. From equation (2.64) and multiple experiments, gas friction is not a significant dissipation source below 10m torr and thus has little effect on Q, as shown in figure 2.8(a). In previous studies and our work, nanotube resonators were all measured at pressure below 10^{-4} torr, indicating that gas friction should be minimized and will not contribute low *Qs*.

B. Clamping loss

Clamping loss is that a resonator loses its mechanical energy to the supports due to the strain at the connection to the support structure. In principle, it is expected to be temperature independent and especially important to doubly-clamped beam resonators. It has been experimentally demonstrated that with identical beam length, a free-free beam resonator shows roughly 2.5 times improvement over a doubly-clamped beam resonator [30]. Also, singly-clamped beam resonators (or cantilever) tend to have higher quality factors than doubly clamped beam resonators due to reduction of clamping loss [11]. In typical, clamping loss is theoretically modeled as elastic radiation of energy through the supports and predict a loss for a rectangular beam in the form of:

$$Q_{clamping}^{-1} \propto \frac{bh^4}{l^5} \qquad (2.68)$$

, where b is the beam width, h is the beam thickness, l is the beam length, and the proportionality constant is dependent upon material properties. From equation (2.68), to reduce clamping loss, a beam with a high aspect ratio is desirable. Since nanotubes and graphene have very high aspect ratio, they are expected to have minimum clamping loss. However, although according to equation (2.68) the clamping loss should not a dominant loss for current NEMS resonators in comparison with other loss sources, the theory behind the clamping loss is still not fully developed and maybe there is still a significant form of dissipation existing for NEM resonators.

For nanotube resonators, we know that nanotubes have high aspect ratio so that the clamping loss is expected to be low and negligible comparing to other losses. In addition, theoretical calculation also shows that the calculated dissipation is at least 10 times smaller than experimental data [20] and nanotube resonators with different geometries also show similar *Qs*. Therefore, we can exclude the clamping loss in nanotube resonators.

C. *Surface loss*

Resent experiments [5] have shown a distributing trend in the quality factors of resonators as a function of their volume, as shown in figure 2.8(b). The measured quality factor decreases in a linear fashion as the surface-to-volume ratio (*S/V*) increases, directly indicating that the surface loss plays an important role in determining the quality factors. This phenomenon can be further understood from a macroscopic view. Since dissipation arises from internal defects, therefore, when the system size is quite large, one only needs to consider bulk defects distribution. However, as the system size shrinks the surface defects start to contribute and even dominate. For large *S/V* ratio, the number of defects (dissipation) increases linearly with *S/V*. Those surface defects can be adsorbed molecules, dangling bonds, or amorphous oxide layers that occur at the surface. They absorb energy from the fundamental resonance mode and transfer it to other modes and dissipate as thermal energy.

This linear trend dominated by surface losses can also be explained by looking at the definition of the quality factor, $Q=2\pi E_0 / \Delta E$, where E_0 is the energy initially stored in the resonator, ΔE is the loss of energy per cycle. For resonating beams, the energy of a resonator is stored in the elastic strain throughout its volume and thus is proportional to its volume, V. If we assume that energy is predominately dissipated at the surface, then we would expect that the energy lost per cycle would be proportional to the surface area S, and thus:

$$Q_{surface}^{-1} \propto S/V \propto L^{-1} \tag{2.69}$$

Here, we would like to point out a general misconception that surface roughness gives rise to dissipation. A “static” rough surface will not cause dissipation, since dissipation only occurs at defects with a time-dependent potential. A time dependent potential can be formed either by a dangling bond, defects or impurity atoms moving back and forth either inside the structure or on the surface, and contaminant atoms or molecules on the surface with appropriate time dependence. It has been shown that various surface treatments such as annealing [31], oxygen removal from the surfaces [32], and surface passivation [33] can decrease the dissipation in mechanical resonators, further demonstrating the importance of surface loss in determining quality factors of small-sized resonators.

D. Ohmic loss

Ohmic loss is associated with the external circuit and caused by electrons moving through the resonator due to capacitive coupling to a nearby gate. When the time for one oscillation is matched to the time for electrons to flow through the resonator, charge flow through the resonator will dissipate energy through Joule heating. We can further model the system can as a variable capacitor in series with a resistor (*R*), where a voltage *V* is applied. The vibration with amplitude z will lead to the change in the capacitance as $\Delta C = C'$z, where *C'* is the derivative of the capacitance with respect to Z. The induced charges can be expressed as $\Delta q = C'zV$. The time for charge to flow through the resistor is determined by the RC constant of the circuit, $t = 2\pi RC$. As the result, the energy dissipated strength (ΔE) on the resonator due to ohmic loss can be expressed as

$$\Delta E = I^2 R\, t = (\frac{\Delta q}{t})^2 R\, t = \frac{C' V^2}{\pi k C} \qquad (2.70)$$

, where *k* is the spring constant of the resonator. The ohmic loss has also been examined in nanotube resonators [20] and excluded as the main dissipation in nanotube resonators. If it is the dominant loss, we should see that nanotube resonators with smaller contact resistance have higher *Qs*. However, no resistance dependent behavior has been reported, indicating ohmic loss is not the main dissipation, neither.

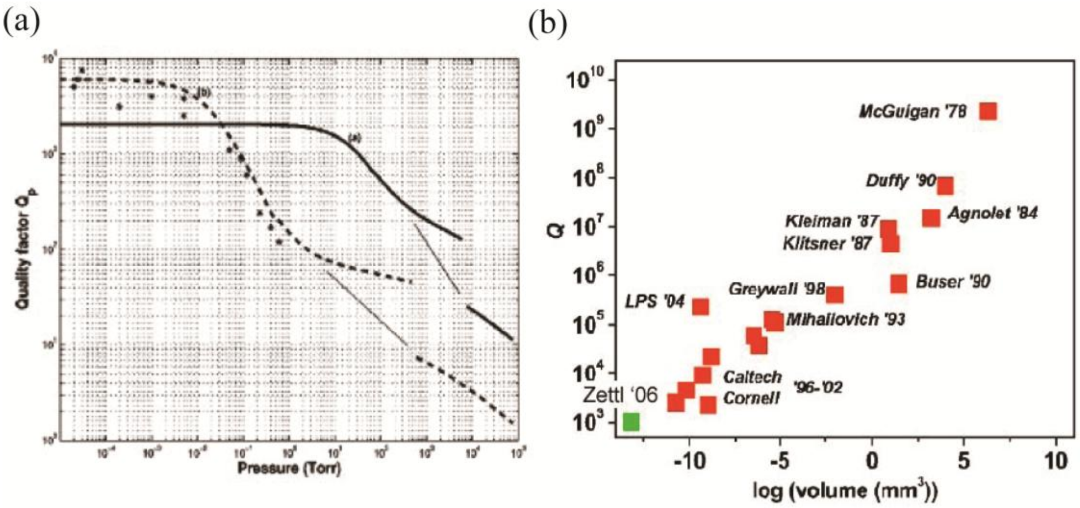

Figure 2.8. Extrinsic losses. (a) Gas friction loss: At high pressures, air can be considered as a viscous fluid, and the viscous damping is proportional to the square root of the pressure. For pressure below 10^{-2} torr, gas friction is not a significant dissipation source [28]. (b) Surface loss: The measured quality factors decrease in a linear fashion as the surface-to-volume ratio increases [5].

2.7 Applications

With their nanometer scale geometry sizes and high operation frequencies, NEMS hold great promises for much advanced performances in a broad range of applications. To date, they have been served in many unprecedented applications such as mass spectrometry [34-35], communications systems [36], and nanobiotechnology [37-38] and used for fundamental studies of both classic and quantum physics [39-42]. In addition, NEMS-based modulators of light utilizing the concept of optomechanics [43] and NEMS-based mechanical mixers for signal processing have been demonstrated as well [44]. In this section, we will discuss a couple of emerging NEMS applications.

2.7.1 *Mass spectrometry*

Mass spectrometry is an analytical technique used for determining the mass of particles and the elemental composition of molecules. It has already been demonstrated to provide rapid and quantitative identification of protein species with relatively low sample consumption as well [45-46]. For ultimate individual cell analysis, mass spectrometry with a sensitivity of a few to single molecule will be necessary, implying NEMS hold great potential in this field. For a NEMS resonator functioning as a mass sensor, the mass sensitivity (Δm) is determined by the shift of resonance frequency when deposited mass is adsorbed onto the resonator and is given by [1]

$$\Delta m \approx \left|\frac{\partial m_{eff}}{\partial \omega_0}\right| \omega_0 \approx \frac{2m_{eff}}{\omega_0}\Delta\omega \qquad (2.71)$$

, where m_{eff} is the effective mass of the resonator, ω_0 is the resonance frequency, and $\Delta\omega$ is the frequency resolution. The quantity $(2m_{eff}/\omega_0)^{-1}$, denoted as the mass responsivity (R), is an important parameter to evaluate a resonator as a mass sensor. High R enables better sensitivity and can be obtained with low m_{eff} and high ω_0, suggesting that carbon nanotubes and graphene are promising candidates due to their low mass and high Young's modulus. Furthermore, the frequency resolution, in general, can be approximated roughly by the quality factor, and therefore the minimum detectable mass can then be simply rewritten as $\Delta m = 2\frac{m_{eff}}{Q}$. So far, the mass sensitivity around zeptogram (zg) has been demonstrated [34-35].

2.7.2 *BioNEMS*

In the early 1990's, the micron scale mechanical resonator was first employed to study biological molecules and their interactions, opening up the applications of

MEMS in biosesning [47]. After this pioneering work, developments in biochemical microarray technologies showed significant advances in analyzing protein receptors, their ligands, and the gene expression profiles [48-49]. Nowadays, microarrays of a few thousand targets have become an important technique in biosensing, and are commercially available and widely used. However, although they are commercially widespread, several challenging issues are waiting for being overcome. Firstly, the large size of the reader instrumentation and the intrinsic limitations of the fluorescence analysis make them not suitable for applications where both portability and robust performance are required. Furthermore, it is a single-use methodology and thus the devices cannot easily accommodate to applications that require continuous monitoring. Lastly, those microarray devices rely on significant volumes of analyte, making them poor for exploring gene expression at the cellular scale.

To solve these practical concerns, the BioNEMS is probably a promising solution since they offer many advantages unattainable from micron scale mechanical devices [50]. Firstly, BioNEMS are scalable and they can interact with highly controlled, extremely reduced population of analytes. Secondly, their small active mass promises sensitivity to single molecule; and their fluid-loaded response can easily provide response times around microseconds. In addition, BioNEMS force measurements offer an attractive alternative to the fluorescent labeling and optical detection that are principal protocols for biochemical microarray assays. Lastly, with their nanoscale feature size, they can be performed extremely locally and provide assays on samples smaller than the diffraction limit.

2.8 Conclusion

In this chapter, we describe several intriguing attributes of NEMS resonators. To model a NEMS resonator, we start from a linear SHO model and then review the beam mechanisms of doubly-clamped beam resonators. In addition, the nonlinear dynamics in NEMS resonators, such as Duffing oscillator and nonlinear damping are also discussed briefly. To measure the resonance of NEMS resonators, various approaches have been employed so far. We summarized the electrical scheme in conjunction with the mixing concept employed in measuring nanotube and graphene resonators. Furthermore, we also discussed several important dissipation mechanisms in NEMS resonators. In last section, we described two emerging NEMS applications. In mass spectrometry, the mass sensitivity is directly related to the effective mass and the quality factor of the resonator. For biosensing, small volume and light active mass are much desired. Based on those discussions, carbon-based NEMS resonators would be potential candidates in realizing these prospects due to their extremely light mass and ultrahigh elastic modulus. This motivates and drives us to focus on NEMS resonators made out of carbon nanotubes and graphene.

REFERENCE

[1]K. L. Ekinci, X. M. H. Huang, and M. L. Roukes, "*Ultrasensitive nanoelectromechanical mass detection*", Appl. Phys. Lett. **84**, 4469 (2004).

[2]M. Roukes, "*Nanoelectromechanical systems face the future*", Phys. World **14**, 25 (2001).

[3]H. J. Mamin, and D. Rugar, "*Sub-attonewton force detection at millikelvin temperatures*", Appl. Phys. Lett. **79**, 3358 (2001).

[4]J. Eisert *et al.*, "*Towards quantum entanglement in nanoelectromechanical devices*", Phys. Rev. Lett. **93**, 190402 (2004).

[5]K. L. Ekinci, and M. L. Roukes, "*Nanoelectromechanical systems*", Rev. Sci. Instrum. **76**, 061101 (2005).

[6]H. G. Craighead, "*Nanoelectromechanical systems*", Science **290**, 1532 (2000).

[7]B. Ilic *et al.*, "*Attogram detection using nanoelectromechanical oscillators*", J. Appl. Phys. **95**, 3694 (2004).

[8]A. N. Cleland, and M. L. Roukes, "*Noise processes in nanomechanical resonators*", J. Appl. Phys. **92**, 2758 (2002).

[9]L. Sekaric *et al.*, "*Nanomechanical resonance structures in silicon nitride: fabrication, operation and dissipation issues*", Sens.Actuators A **101**, 215 (2002).

[10]J. Q. Broughton *et al.*, "*Direct atomistic simulation of quartz crystal oscillators: Bulk properties and nanoscale devices*", Phys. Rev. B **56**, 611 (1997).

[11]A. N. Cleland, "*Foundations of Nanomechanics"*, Springer-Verlag (2003).

[12]A. N. Cleland, and M. L. Roukes, "*Fabrication of high frequency nanometer scale mechanical resonators from bulk Si crystals*", Appl. Phys. Lett. **69**, 2653 (1996).

[13]B. Ilic *et al.*, "*Optical excitation of nanoelectromechanical oscillators*", Appl. Phys. Lett. **86**, 193114 (2005).

[14]V. Sazonova *et al.*, "*A tunable carbon nanotube electromechanical oscillator*", Nature **431**, 284 (2004).

[15]C. Y. Chen *et al.*, "*Performance of monolayer graphene nanomechanical resonators with electrical readout*", Nat. Nanotech. **4**, 861 (2009).

[16]R. Lifshitz, "*Reviews of nonlinear dynamics and complexity*", Wiley VCH vol. 1 (2008).

[17]A. Eichler *et al.*, "*Nonlinear damping in mechanical resonators made from carbon nanotubes and graphene*", Nat. Nanotech. **6**, 339 (2011).

[18]H. W. C. Postma *et al.*, "*Dynamic range of nanotube- and nanowire-based electromechanical systems*", Appl. Phys. Lett. **86**, 223105 (2005).

[19]J. S. Bunch *et al.*, "*Electromechanical resonators from graphene sheets*", Science **315**, 490 (2007).

[20]V. Sazonova, "*A Tunable Carbon Nanotube Resonator*", PhD. Thesis, Cornell University, Ithaca, NY (2006).

[21]S. J. Tans, A. R. M. Verschueren, and C. Dekker, "*Room-temperature transistor based on a single carbon nanotube*", Nature **393**, 49 (1998).

[22]S. Rosenblatt *et al.*, "*Mixing at 50 GHz using a single-walled carbon nanotube transistor*", Appl. Phys. Lett. **87,** 153111 (2005).

[23]R. G. Knobel, and A. N. Cleland, "*Nanometre-scale displacement sensing using a single electron transistor*", Nature **424**, 291 (2003).

[24]V. Braginsky, Mitrofanov, V., and Panov, V., "*Systems with small dissipation*", The University of Chicago Press (1985).

[25]A. a. B. Nowick, B., "*Anelastic relaxation in crystalline solids*", Academic Press. (1972).

[26]P. Mohanty, *et al.*, "*Intrinsic dissipation in high-frequency micromechanical resonators*", Phys. Rev. B **66**, 085416 (2002).

[27]C. Seoanez, F. Guinea, and A. H. Castro, "*Dissipation in graphene and nanotube resonators*", Phys. Rev. B **76**, 125427 (2007).

[28]L. Landau, "*Fluid Mechanics*", Nauka (1982).

[29]R. B. Bhiladvala, and Z. J. Wang, "*Effect of fluids on the Q factor and resonance frequency of oscillating micrometer and nanometer scale beams*", Phys. Rev. E **69**, 036307 (2004).

[30]X. Huang, Prakash, M., Zorman, C., Mehregany, M., and Roukes, M. L., "*In transducers, 03 Proceedings 12th International conference on Solid State Sensors, Actuatos and Microsystems, Boston, MA.*" (2003).

[31]K. Y. Yasumura *et al.*, "*Quality factors in micron- and submicron-thick cantilevers*", J. MEMS **9**, 117 (2000).

[32]J. L. Yang, T. Ono, and M. Esashi, "*Surface effects and high quality factors in ultrathin single-crystal silicon cantilevers*", Appl. Phys. Lett. **77**, 3860 (2000).

[33]Y. Wang *et al.*, "*Methyl monolayers suppress mechanical energy dissipation in micromechanical silicon resonators*", Appl. Phys. Lett. **85**, 5736 (2004).

[34]K. Jensen, K. Kim, and A. Zettl, "*An atomic-resolution nanomechanical mass sensor*", Nat. Nanotech. **3**, 533 (2008).

[35]A. K. Naik *et al.*, "*Towards single-molecule nanomechanical mass spectrometry*", Nat. Nanotech. **4**, 445, (2009).

[36]C. T. C. Nguyen, "*Microelectromechanical devices for wireless communications", IEEE* MEMS 98 Proceedings 1(1998).

[37]T. P. Burg *et al.*,"*Weighing of biomolecules, single cells and single nanoparticles in fluid*", Nature **446**, 1066 (2007).

[38]B. Ilic, Y. Yang, and H. G. Craighead, "*Virus detection using nanoelectromechanical devices*", Appl. Phys. Lett. **85**, 2604 (2004).

[39]M. D. LaHaye *et al.*, "*Approaching the quantum limit of a nanomechanical resonator*", Science **304**, 74 (2004).

[40]J. B. Hertzberg *et al.*, "*Back-action-evading measurements of nanomechanical motion*", Nat. Phys. **6**, 213 (2010).

[41]J. Eisert *et al.*, "*Towards quantum entanglement in nanoelectromechanical devices*", Phys. Rev. Lett. **93** 190402 (2004).

[42]D. Rugar *et al.*, "*Single spin detection by magnetic resonance force microscopy*", Nature **430**, 329 (2004).

[43]L. Sekaric, *et al.*, "*Nanomechanical resonance structures as tunable passive modulators of light*", Appl. Phys. Lett. **80**, 3617 (2002).

[44]A. Erbe, *et al.*, "*Mechanical mixing in nonlinear nanomechanical resonators*", Appl. Phys. Lett. **77**, 3102 (2000).

[45]R. Aebersold, and M. Mann, "*Mass spectrometry-based proteomics*", Nature **422**, 198 (2003).

[46]B. Domon, and R. Aebersold, "*Review - Mass spectrometry and protein analysis*", Science **312**, 212 (2006).

[47]J. H. Hoh, *et al.*, "*Quantized adhesion detected with the atomic force microscope*", J. Am. Chem. Soc. **114**, 4917 (1992).

[48]M. Schena, *et al.*, "*Quantitative Monitoring of Gene Expression Patterns with a Complementary DNA Microarray* ", Science **270**, 467 (1995).

[49]A. Brazma, *et al.*, "Minimum information about a microarray standards for microarray data", Nat. Gen. **29**, 365 (2001).

[50]J. L. Arlett, *et al.*, "BioNEMS: Nanomechanical Systems for Single-Molecule Biophysics", Nobel Symposium 131 (2005).

CHAPTER 3

ONE-STEP DIRECT TRANSFER OF PRISTINE SINGLE-WALLED CARBON NANOTUBES FOR FUNCTIONAL NANOELECTRONICS

3.1 Introduction

SWNTs are 1D nanostructures with remarkable electrical, mechanical, and optical properties [1-3]. They are ideal platform for studying low dimensional physics as well as exploring novel applications with quantum-size effect [4-7]. Their high carrier mobility leads to high speed nanoelectronics [8-10]. In addition, their low mass density and high Young's modulus make them ideal building blocks in NEMS with potential applications as ultrasensitive sensors [11-14]. Furthermore, semiconducting SWNTs are direct-bandgap materials capable of efficient absorption and emission of photons [15-18]. SWNT p-n diodes have been fabricated [19-21] with ideality factors close to unity, and light emitting diodes (LEDs) and photodetectors using SWNTs have also been demonstrated [22-24]. Recent study also showed extremely efficient multiple electron-hole pairs generation in SWNTs, suggesting potential photovoltaic applications utilizing SWNTs as the light absorber [25].

However, in spite of a variety of remarkable advantages possessed by SWNTs, their applications are constrained by fabrication issues: fabricating functional nanoelectronics with pristine SWNTs at ambient temperature and placing SWNTs onto the designed positions parallelly. Conventionally, SWNT nanoelectronics are fabricated with either post-growth fabrication or post-fabrication growth approach [1, 26-27] (see section 3.2 for details). The post-growth fabrication was first developed and widely adopted today; however, using this approach, SWNTs are inevitably contaminated by organic residues resulting from the lithography and solution processing. As a result, to eliminate contaminations, the post-fabrication growth method was proposed to avoid those solution processing. The later method results in ultraclean SWNT devices, but the high growth temperature (~900 ℃) prohibits its wide applications. More recently, SWNTs grown on substrate were transferred onto electrodes by stamping [28-29]. However, in this method, potential contamination and damages to SWNTs can come from the stamping process, and the registry of SWNTs to the electrodes is entirely random.

To this end, our goal is to develop a novel process technique in order to avoid all the drawbacks described above. In section 3.3, the one-step direct transfer technique to fabricate functional nanoelectronics with pristine SWNTs at ambient temperature is presented. This process technique is first characterized by evaluating the electrical conductance, process yield and feasibility on different substrates. To further verify the reliability of this one-step direct transfer technique, we successfully fabricated SWNT resonators with gate-tunable resonance frequencies (section 3.4) and demonstrated a fully suspended SWNT p-n diode with the ideality factor equal to 1 (section 3.5). In addition, by using this process technique, we are able to add additional end-gate electrodes to fabricate nanotube resonators with dual-gate configurations to investigate the frequency tuning mechanisms, which will be discussed in next chapter.

3.2 Conventional process methods to make SWNT nanoelectronics

3.2.1 Post-growth fabrication method

Briefly speaking, the SWNTs are first placed onto the device substrate by either direct CVD growth or indirect solution process. Standard lithography is then carried out to construct the device structures. The procedure of the post-growth fabrication to make a typical SWNT resonator is illustrated in figure 3.1 (a).

Firstly, catalyst pads are patterned by using standard lithography on a Si/SiO_2 wafer for SWNT CVD growth. To grow SWNTs, the substrate is placed into a CVD furnace, where carbon source gas, such as CH_4 or C_2H_2 is flowing at high temperature. After growth, source/drain electrodes are defined on the top of the catalyst pads and contact metals, usually Au or Pd, are deposited. To suspend the nanotubes, wet etching is conducted by using buffered hydrofluoric acid (BHF) to remove the underneath SiO_2. Lastly, a critical point drying step is manipulated to prevent the CNTs from breaking or contacting the substrate due to the tension on the nanotube caused by the water.

Since all lithographical processes are conducted after CNTs are placed onto the substrates, CNTs will inevitably experience these photo- or e-beam resistors and various chemical solutions. As a result, they are very likely damaged and contaminated by those organic residues. Those contaminations may either increase tension on the nanotubes leading to fundamental frequency shifted, or dope the nanotubes causing the direct point shifted, or increase the effective mass of nanotubes that will reduce the sensitivity of CNT resonators. These unwanted behaviors degrade the performance and also limit their applications in exploring fundamental studies of physics if ultraclean nanotubes are required.

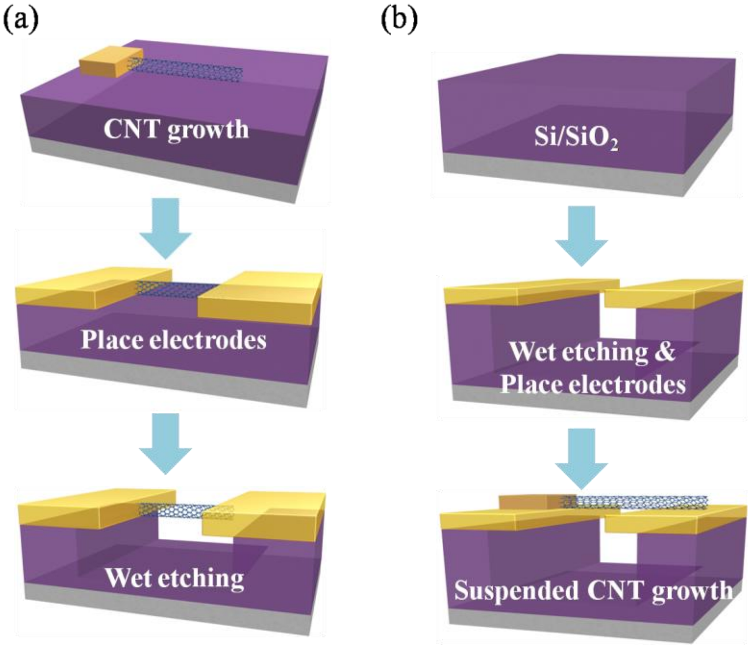

Figure 3.1. Conventional process methods to make CNT devices. (a) Post-growth fabrication. Catalyst pads are patterned by using standard lithography on a Si/SiO$_2$ wafer for CNT CVD growth. After CNT growth, metal contacts are defined and deposited on top of the catalyst pads. For making a CNT resonator, wet etching is conducted by using BHF to remove underneath SiO$_2$. A critical-point drying step is then performed to suspend the CNT in order to prevent CNT from contacting the bottom. (b) Post-process growth. Conventional lithography is carried out first to define electrical contacts made out of high melting temperature metals on a Si/SiO$_2$ wafer. A catalyst pad is then placed on the top of contact metals and CNTs are subsequently grown across the trench directly on top of the electrodes by CVD method.

3.2.2 Post-process growth method

To avoid the contaminations resulting from the organic resides and solution process, the post-process growth approach reverses the process steps of the post-growth fabrication. Instead of placing SWNTs on the substrate first, lithography is carried out first to construct the device structures and nanotubes are grown subsequently. The process flow is depicted in figure 3.1(b). First, the trenches in SiO_2 are defined by conventional lithography and then removed by wet etching. The electrical contacts made out of high melting temperature metals such as Platinum (Pt) are defined and deposited. A catalyst pad is then placed on the top of contact metals; thereafter, suspended SWNTs are subsequently grown across the trench directly on top of the electrodes by CVD method.

Although this approach results in ultraclean SWNT devices, the high growth temperature (700~900 °C) unfortunately prohibits its wide applications. Firstly, the applicable device substrates are limited by this high growth temperature. For instance, polymer substrates for fabricating flexible nanoelectronics cannot endure temperature higher than 200 °C. In addition, for nanoelectromechanical sensors, room temperature fabrication of pristine CNT resonators is much preferred. Moreover, the chosen contact metal, Pt, cannot form a good ohmic interface with respect to nanotubes. As a result, a barrier has always occurred between Pt and nanotubes, leading to much higher contact resistance and affects its performance in a variety of applications, such as electron transport or RF circuits, in which impedance matching is crucial.

3.3 One-step direct transfer of pristine SWNTs

To solve the problems mentioned above, we successfully carried out a one-step direct transfer technique to fabricate functional devices from pristine suspended SWNTs at room temperature. Briefly, suspended SWNTs grown by CVD method on a separate growth substrate are aligned and directly transferred onto the device substrate containing prefabricated electrodes to form nanoelectronics. Specifically, our approach can be further divided into three steps: the synthesis of suspended SWNTs, the process of pre-patterning device electrodes, and the direct transfer of SWNTs from the growth substrate onto the device substrate. Details are described below.

3.3.1 Synthesis of suspended carbon nanotubes

The synthesis of suspended SWNTs is illustrated in figure 3.2(a). Here, a double-side polished (DSP) quartz substrate is chosen as the growth substrate due to its transparency for alignment purpose and its endurance in high growth temperature. Firstly, a conventional photolithography (GCA AC200 AutoStepper) is carried out to define the area of each pillar (5 x 20 μm^2), and then followed by plasma dry etching (LAM 9400) to form the pillars. We note that a slack is naturally formed when SWNTs are suspended across the trench. To prevent suspended nanotubes from contacting the bottom due to the slack, the ratio of the pillars' height to the distance between a pair of pillars is kept lager than 1/3 [30]. For CVD growth, 3 Å Fe is deposited by using e-beam evaporator (SJ-26) as growth catalysts. An ethanol recipe is used in our experiment for SWNT growth, where SWNTs are grown in a horizontal furnace with He (100 sccm), H2 (40 sccm), and ethanol bubbler (120 sccm) flowing for 20 minutes at 925 ^{0}C, as shown in figure 3.2(b).

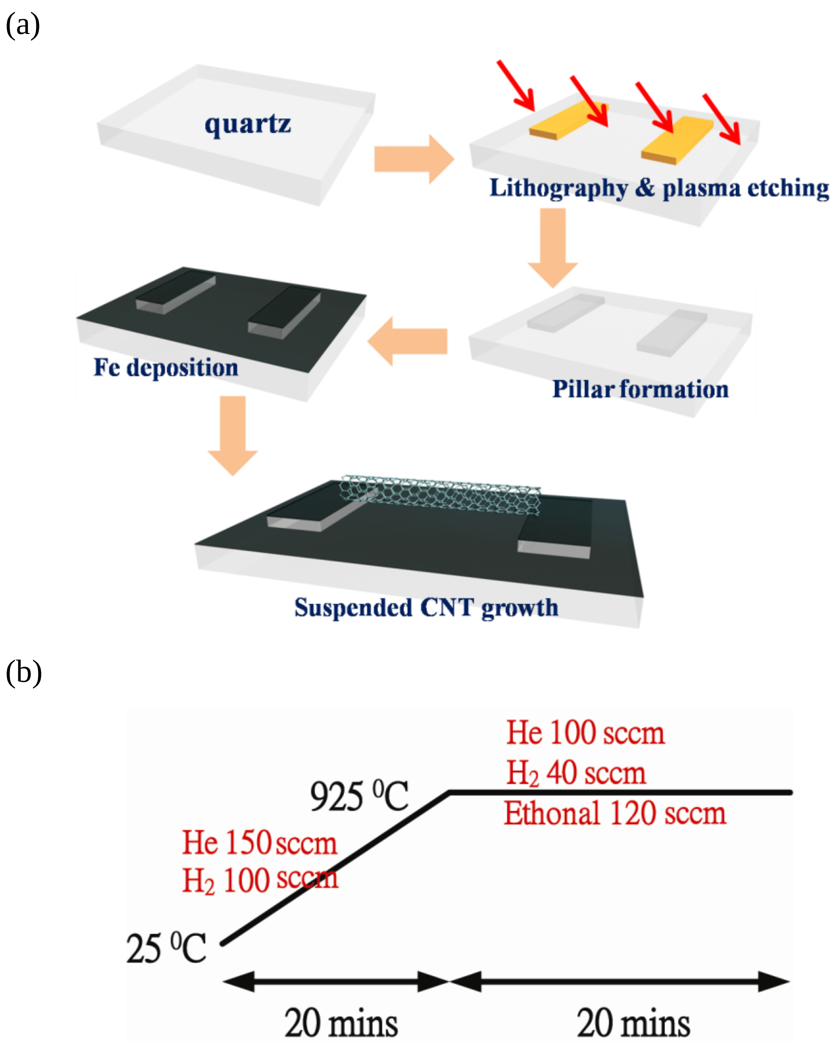

Figure 3.2. Synthesis of suspended carbon nanotubes. (a) A quartz substrate is chosen as growth substrate. Conventional lithography with plasma dry etching is used to form pillars. 3 Å Fe is deposited as catalyst for CVD growth. (b) Ethanol bubbler recipe for SWNT growth.

3.3.2 Process of pre-patterning device electrodes:

Figure 3.3(a) illustrates the procedure of preparing device electrodes. Firstly, SiO_2/Si_3N_4 = 500nm/500nm are deposited on Si wafer by low pressure chemical vapor deposition (LPCVD). Following photolithography and a sequence of etching processes, source/drain electrodes are patterned. Then, the top Si_3N_4 layer is etched away first by anisotropic plasma-etching (LAM 9400) and SiO_2 is removed by isotropic wet-etching with BHF. Note that BHF is a good selective etchant against SiO_2 and Si3N_4, so an undercut structure is expected to form due to isotropic wet- etching (figure 3.3(b)). The undercut structure will avoid electrical shortage between top and bottom electrodes when blanket deposition of Cr/Au=5nm/50nm is conducted. Lastly, we define bottom gate electrodes and etch Cr/Au by chrome (Cr-14) and gold (GE-8148) etchants

(a)

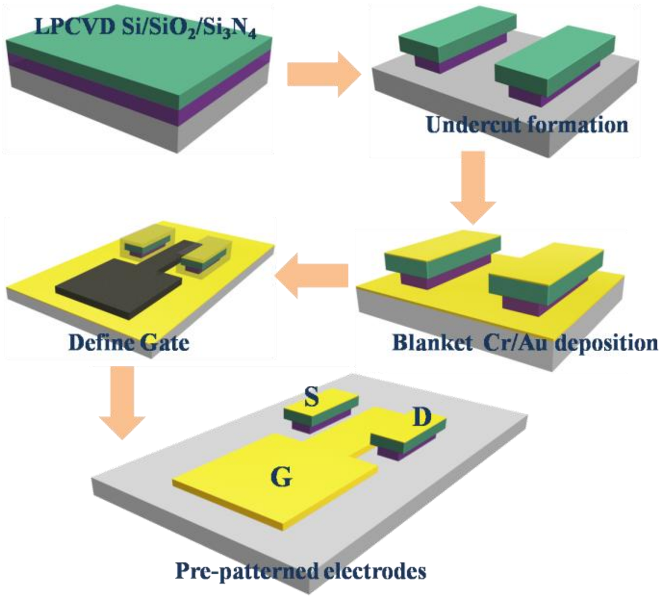

(b)

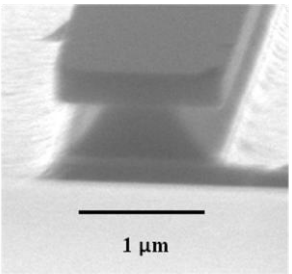

Figure 3.3. Process of pre-patterning device electrodes. (a) Si_3N_4/SiO_2 are deposited on Si wafer by LPCVD. Photolithography is conducted to pattern source/drain electrodes. Plasma dry etching and wet etching with BHF are performed subsequently to form an undercut structure. Another photolithography step is processed to define bottom gate electrodes. (b) SEM image of an undercut structure.

3.3.3 Stamping (Direct transfer of nanotubes)

After synthesizing suspended SWNTs and preparing the device substrate, the last step is to directly transfer suspended SWNTs onto the device substrate. The transfer process is shown in figure 3.4. Contact aligner (Karl Suss MJB-3) is used to manipulate the one-step direct transfer. Firstly, the quartz substrate is mounted upside-down on a blank glass mask, while the device substrate is placed on the sample stage of the manipulator (left panel). The quartz substrate is then aligned to the device substrate and subsequently brought into contact by lifting the stage (middle panel). Since the spacing of the pillars is designed to be wider than the electrode spacing, SWNTs are cut off at the contact points between the pillars and the substrate and span across the electrodes (right panel). As a result, functional SWNT nanoelectronics are readily formed without the need of further lithography, eliminating potential contamination on the nanotubes.

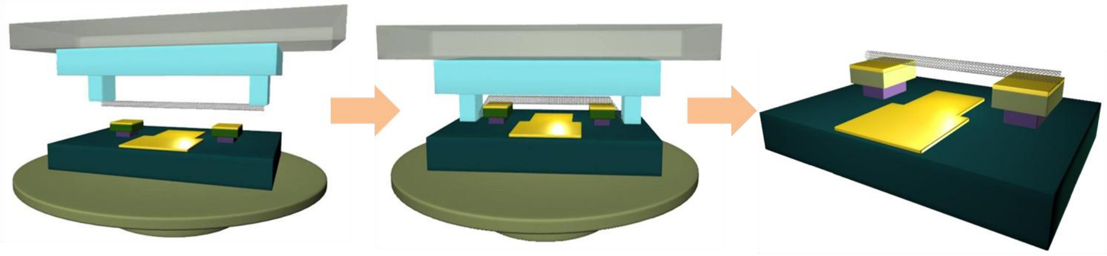

Figure 3.4. Schematic of one-step direct transfer procedure. A quartz substrate with a suspended SWNT grown on is mounted upside-down on a blank mask, and a device substrate with prefabricated electrodes is placed on the stage of the contact aligner (left panel). The quartz substrate is aligned to the device substrate and subsequently brought into contact by lifting the stage (middle panel). SWNTs are cut off at the contact points and span across the electrodes (right panel).

3.3.4 Characterizations

We first characterize our one-step direct transfer technique by taking SEM images of implemented devices, and evaluating the electrical conductance of a suspended SWNT FET, the yield of transfer process, and its feasibility applied on different dielectric substrates.

A. SEM imaging

The process technique is examined first by taking the SEM images to view the appearance of implemented devices. Figure 3.5 (a) and (b) show the lateral and top views of devices fabricated by using the one-step direct transfer technique. Nanotubes indicating by red arrows span across four pre-patterned metal electrodes.

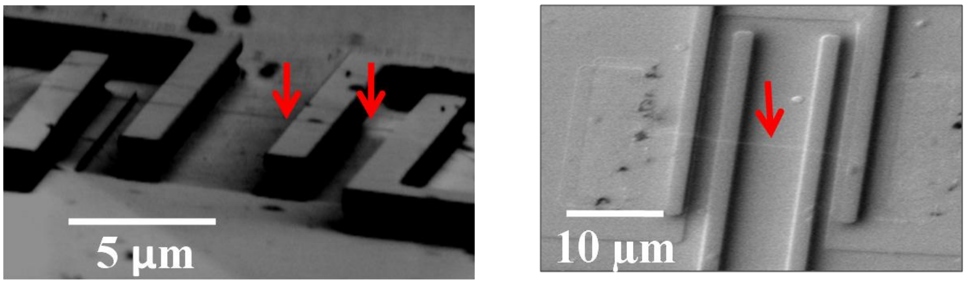

Figure 3.5. SEM image of devices fabricated by the one-step direct transfer technique. Left panel: lateral view and right panel: top view. Nanotubes span across four pre-patterned metal electrodes and the arrows indicate the positions of nanotubes.

B. Electrical conductance

The electrical contact between a nanotube and metal electrode resulting from our one-step direct transfer is evaluated by using a suspended SWNT FET configuration (Figure 3.4). Nanotube channel lengths are designed to be 1-3 μm, while Au and Pd are explored as bottom-contact metals. Figure 3.6(a) shows a conductance vs. gate voltage curve for a typical nanotube transistor. Classic transfer characteristics of a p-channel FET is observed, with ON state conductance of 12 μS and ON/OFF ratio larger than 4 orders of magnitude [31]. The device also exhibits negligible hysteresis, indicating that the nanotube is indeed suspended in air. Hysteresis is caused by charges on the SiO_2 if nanotubes are laid on the SiO_2. Similar results are obtained on 50 devices, and histogram suggests an average ON state conductance of ~12 μS (Figure 3.6(a), inset). These results are comparable with top-contacted nanotube transistors, confirming that our simple on-step direct transfer technique results in similar contact resistance as conventional fabrication technique. In addition, thermal annealing is helpful for reducing the device contact resistance but not necessary for freshly deposited metals. Typical annealing is carried out at 250 ℃ in helium for 5 min for Pd and at 400 ℃ for Au.

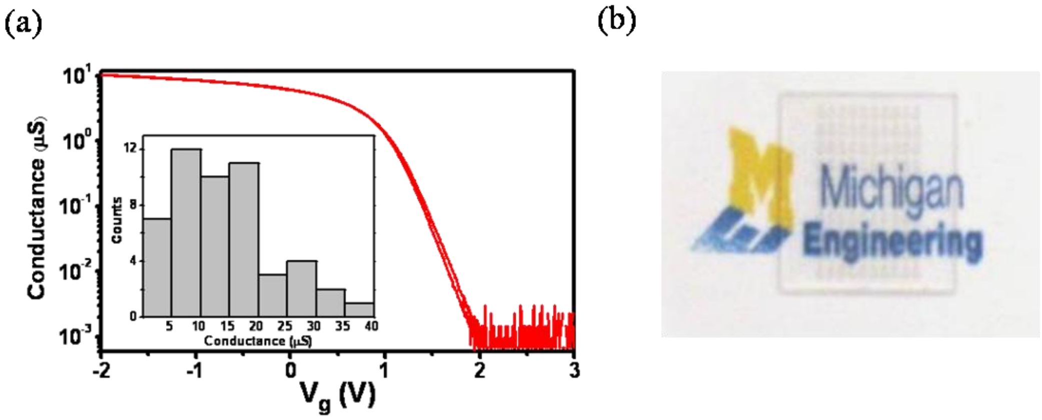

Figure 3.6. Characteristics of the one-step direct transfer technique. (a) Conductance vs. V_g for a typical suspended SWNT transistor. Classic transfer characteristics of a p-channel FET is observed, with ON state conductance of 12 μS and ON/OFF ratio larger than 4 orders of magnitude. The device also exhibits negligible hysteresis, indicating that the nanotube is indeed suspended in air. The inset shows the conductance histogram of 50 devices, and histogram suggests an average ON state conductance of ~12 μS. (b) Optical image of SWNT devices on transparent glass substrate. Die with size 1 cm × 1 cm is placed on top of a “Michigan Engineering” logo.

C. Yield

We further evaluate the yield of our one-step direct transfer technique to fabricate SWNT devices. Firstly, SEM is taken to identify 14 pairs of pillars on quartz substrate where one or a few nanotubes are grown and suspended across. After transfer, electrical measurements confirm that 13 out of 14 corresponding devices are successfully fabricated, converting to ∼92% transfer yield. 100% transfer is possible by modifying our setup to allow precise control of contact force. The overall yield is thus dictated by the growth yield of nanotubes suspended across the pillars, which can be controlled statistically by the pillar dimensions and growth condition. In general, we tune our growth condition to have on-average a single nanotube within an individual device, which results in an overall device yield of ∼20-40%.

D. Feasibility

Our technique can be widely adopted on different types of substrates since the transfer process is carried out under ambient condition. SWNT devices on a transparent glass substrate have been demonstrated through one-step direct transfer (Figure 3.6 (b)). In addition, we have also fabricated nonsuspended SWNT FET devices on substrate with high-κ dielectrics (data not shown). Moreover, we believe the technique can be readily applied onto a plastic substrate for flexible nanoelectronics and nanophotonics.

3.4 SWNT nanoelectromechanical resonators

To demonstrate the versatility of our technique, we first fabricate SWNT resonators by our one-step direct transfer technique. The SEM image of a typical SWNT resonator is shown in figure 3.7(a), with nanotube length of 1-3 μm and nanotube/bottom-gate separation of 1 μm. To measure the resonance frequency of the nanotube resonator, we adopt the single-source mixing technique (AM modulation) described in section 2.5. For the sake of convenience, we reproduce the measurement setup in figure 3.7(b). For internal AM modulation, a small signal at low frequency (1 KHz) is modulated with high frequency signals inside the RF signal generator (Agilent 8648B) and this small signal is also send to the lock-in amplifier (Stanford Research SR830) for reference. The AM signal was then sent to the source electrode to actuate the resonator through electrostatic interaction, and the mixing current from the drain electrode was read by the lock-in amplifier. The SWNT resonators are measured in a vacuum chamber at pressure below 10^{-4} torr and $V_{sd}^{ac} = 10$ mV is applied to drive the nanotube into vibration.

The electromechanical responses of a typical SWNT resonator with channel length of 3 μm is shown in figure 3.7(c). The DC gate voltage (V_{g}) is fixed at 3 V, and the frequency-dependent mixing current (I_{mix}) swept between 20 and 30 MHz reveals a clear peak, corresponding to the guitar-string like resonance mode of the doubly clamped nanotube resonator (Figure 3.7(c), dots). To obtain the resonance frequency, we fit the experimental data with equation (2.60) (Figure 3.7(c), line), yielding the resonance frequency, $f_0 = 26.1$ MHz with quality factor $Q = 90$. We further investigate the frequency tuning of nanotube resonator by sweeping the V_{g}. In figure 3.7(d), mixing current (in color) is plotted as a function of driving frequency and V_{g}. Three resonance modes are clearly observed with strong gate dependence, which corresponds to the in-plane and out-of-plan vibrational modes of the nanotube [32]. More details of different vibrational modes of nanotube resonators will be discussed in the next chapter. The resonance signals of three vibrational modes at V_g= 7 V are plotted in figure 3.7(e) (dots) with well fit (red), showing Q are around few dozens.

We further extract the resonance frequencies with respect to the V_g^{DC} for all three modes and plot them in figure 3.7(f). Three types of gate dependence are observed, quadratic ($f \sim V_g^2$, in red), linear ($f \sim V_g$, in black), and sublinear ($f \sim V_g^{0.7}$ in green), which correspond to bending regime, catenary regime, and elastic regime, respectively [33]. Increased tension due to increased gate voltage causes transition from the bending regime to the catenary regime, and eventually to the elastic regime, which is clearly visible for the second vibrational mode. Similar results have been obtained on other SWNT resonators, with quality factors ranging among 30-150 at room temperature, and resonance frequencies among 5-200 MHz. These results are comparable with previous devices made by conventional techniques, suggesting that our much simplified fabrication technique yields high quality nanotube resonators. In addition, multiple resonators can be fabricated on a single nanotube, opening up possibilities for investigating coupled 1D NEMS resonators in series.

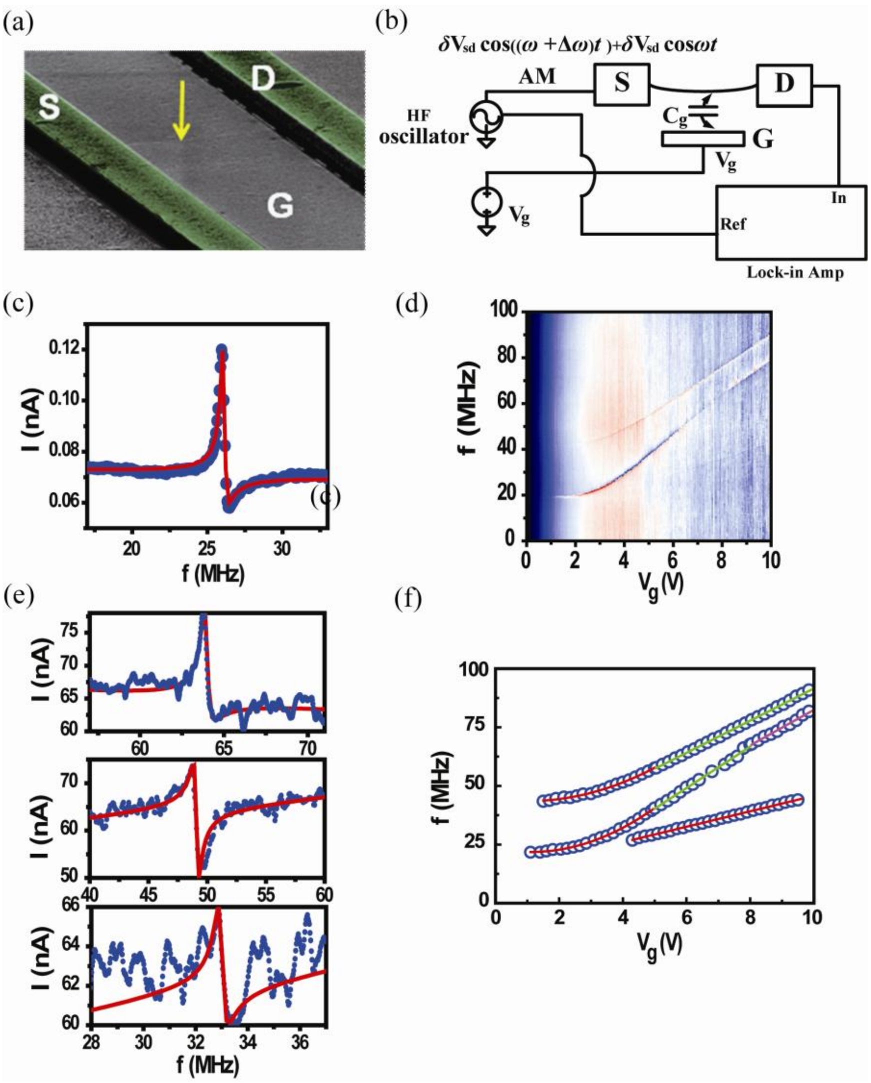

Figure 3.7. SWNT nanoelectromechanical resonators. (a) SEM image of a typical SWNT resonator. An arrow indicates the position of nanotube. (b) Measurement setup of one-source mixing (AM) technique. (c) Mixing currents as a function of driving frequency at Vg = 3 V, and ac driving voltage amplitude V_{sd} = 10 mV is plotted. Dots are the experimental data, and the solid line is the Lorentzian fitting which yields f = 26.1 MHz and quality factor Q = 90. (d) Mixing current (in color scale) is plotted as a function of driving frequency and V_g. Three vibrational resonances are clearly observed. (e) The resonance signals of three vibrational modes at V_g= 7 V are plotted (dots) and with well fit (red), showing Q are around few dozens. (f) Resonance frequencies vs. V_g for all three modes. The data are plotted in color, quadratic dependence ($f \sim V_g^2$) in red, linear ($f \sim V_g$) in green, and sublinear ($f \sim V_g^{0.7}$) in purple.

3.5 Tunable SWNT p-n diodes

The second type device fabricated with our transfer technique is a fully suspended SWNT p-n diode. As shown in figure 3.8(a), a SWNT is transferred and suspended across two split bottom gates, G_1 and G_2. The polarity of the two nanotube sections above the bottom gates is controlled by electrostatic doping through applying gate voltages, respectively. *I-V* characteristics of a typical device are shown in figure 3.8(b) When gate voltages of $V_{g1} = V_{g2} = -2$ V are applied, a linear *I-V* is observed with resistance of 300 kΩ. In this case, both sections are p-doped, and the device behaves as a resistor (Figure 3.8(b), in blue). When the gate voltages are changed to $V_{g1} = 4$ V and $V_{g2} = -4$ V, we obtain a rectified *I-V* curve. Here positive V_{g1} n-dopes the nanotube section above G1 and negative V_{g2} p-dopes the nanotube section above G2, forming a p-n junction (Figure 3.8(b), in red). Significantly, a log-scale *I-V* plot (Figure 3.8(c)) reveals that the fully suspended SWNT p-n diode has an ideality factor of 1 and reversed saturation current of 45 *p*A at room temperature. These results point toward novel optoelectronic applications by exploiting a fully suspended SWNT ideal diode.

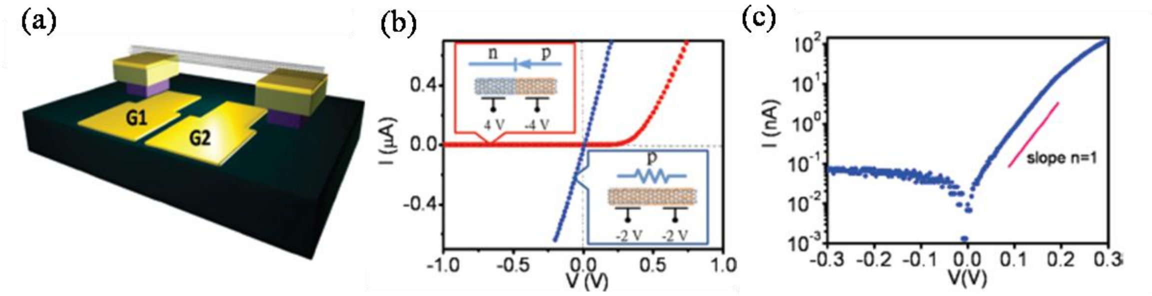

Figure 3.8. A Fully suspended SWNT p-n diode. (a) Schematic of device geometry. The separation between two gates is 1 μm, and the width of each gate electrode is also 1 μm. The separation between nanotube and gate electrode is 2 μm. (b) *I-V* characteristics of a suspended SWNT p-n diode. (c) *I-V* plot in absolute magnitude of the current at gating voltages $V_{g1} = -V_{g2} = 4$ V (blue dots). The red line corresponds to ideality factor $n = 1$ in ideal diode equation.

3.6 Conclusion

In summary, we have reported a powerful yet simple one-step fabrication technique for SWNT devices. Our method eliminates the organic residues on SWNTs resulted from conventional processing approaches. Using this technique, we demonstrate the fabrication of SWNT resonators and fully suspended SWNT ideal diodes. The results open up opportunities for the fundamental study of electron transport physics in ultraclean SWNTs. In addition, the technique can find wide applications for pristine nanotube electronic and photonic devices. It should also benefit the integration of a nanotube device onto a nonconventional substrate where device processing needs to be carried out at ambient conditions.

**This chapter is written based on our work published in Nano Letters, Volume 10, page 1032-1035, 2010.*

REFERENCE

[1]M. D. Dresselhaus, G. Dresselhaus, and P. Avouris, "*Carbon nanotubes: synthesis, structure properties and applications*", Springer-Verlag, Berlin (2001).

[2]P. L. McEuen, M. S. Fuhrer, and H. K. Park, "*Single-walled carbon nanotube electronics*", IEEE Trans. Nanotech. **1**, 78 (2002).

[3]P. Avouris, M. Freitag, and V. Perebeinos, "*Carbon-nanotube photonics and optoelectronics*", Nat. Photonics **2**, 341 (2008).

[4]M. Bockrath *et al.*, "*Single-electron transport in ropes of carbon nanotubes*", Science **275**, 1922 (1997).

[5]W. J. Liang *et al.*, "*Fabry-Perot interference in a nanotube electron waveguide*", Nature **411**, 665 (2001).

[6]S. J. Tans, A. R. M. Verschueren, and C. Dekker, "*Room-temperature transistor based on a single carbon nanotube*", Nature **393**, 49 (1998).

[7]A. Javey *et al.*, "*Ballistic carbon nanotube field-effect transistors*", Nature **424**, 654 (2003).

[8]A. Bachtold *et al.*, "*Logic circuits with carbon nanotube transistors*", Science **294**, 1317 (2001).

[9]Z. H. Chen *et al.*, "*An integrated logic circuit assembled on a single carbon nanotube*", Science **311**, 1735 (2006).

[10]V. Derycke *et al.*, "*Carbon nanotube inter- and intramolecular logic gates*", Nano Lett. **1**, 453 (2001).

[11]A. N. Cleland, "*Foundations of Nanomechanics*" Springer-Verlag, Berlin (2003).

[12]S. Sapmaz *et al.*, "*Carbon nanotubes as nanoelectromechanical systems*", Phys. Rev. B **67**, 235414 (2003).

[13]H. Y. Chiu *et al.*, "*Atomic-Scale Mass Sensing Using Carbon Nanotube Resonators*", Nano Lett. **8**, 4342, (2008).

[14]B. Lassagne *et al.*, "*Ultrasensitive Mass Sensing with a Nanotube Electromechanical Resonator*", Nano Lett. **8**, 3735 (2008).

[15]M. Freitag *et al.*, "*Photoconductivity of single carbon nanotubes*", Nano Lett. **3**, 1067 (2003).

[16]M. J. O'Connell *et al.*, "*Band gap fluorescence from individual single-walled carbon nanotubes*", Science **297**, 593 (2002).

[17]J. A. Misewich *et al.*, "*Electrically induced optical emission from a carbon nanotube FET*", Science **300**, 783 (2003).

[18]J. Chen *et al.*, "*Bright infrared emission from electrically induced excitons in carbon nanotubes*", Science **310**, 1171 (2005).

[19]K. Bosnick, N. Gabor, and P. McEuen, "*Transport in carbon nanotube p-i-n diodes*", Appl. Phys. Lett. **89**, 163121 (2006).

[20]J. U. Lee, P. P. Gipp, and C. M. Heller, "*Carbon nanotube p-n junction diodes*", Appl. Phys. Lett. **85**, 145 (2004).

[21]Y. X. Zhou *et al.*, "*p-channel, n-channel thin film transistors and p-n diodes based on single wall carbon nanotube networks*", Nano Lett. **4**, 2031 (2004).

[22]J. U. Lee, "*Photovoltaic effect in ideal carbon nanotube diodes*", Appl. Phys. Lett. **87**, 073101(2005).

[23]J. U. Lee, P. J. Codella, and M. Pietrzykowski, "*Direct probe of excitonic and continuum transitions in the photocurrent spectroscopy of individual carbon nanotube p-n diodes*", Appl. Phys. Lett. **90**, 053103 (2007).

[24]L. Marty *et al.*, "*Exciton formation and annihilation during 1D impact excitation of carbon nanotubes*", Phys. Rev. Lett. **96**, 136803 (2006).

[25]N. M. Gabor *et al.*, "*Extremely efficient multiple electron-hole pair generation in carbon nanotube photodiodes*", Science **325**, 1367 (2009).

[26]A. M. Cassell *et al.*, "*Large scale CVD synthesis of single-walled carbon nanotubes*", J. Phys. Chem. B **103**, 6484 (1999).

[27]J. Kong *et al.*, "*Synthesis of individual single-walled carbon nanotubes on patterned silicon wafers*", Nature **395**, 878 (1998).

[28]D. R. Hines *et al.*, "*Nanotransfer printing of organic and carbon nanotube thin-film transistors on plastic substrates*", Appl. Phys. Lett. **86**, 136301(2005).

[29]V. K. Sangwan *et al.*, "*Facile fabrication of suspended as-grown carbon nanotube devices*", Appl. Phys. Lett. **93**, 113112 (2008).

[30]Y. Homma *et al.*, "*Growth of suspended carbon nanotube networks on 100-nm-scale silicon pillars*", Appl. Phys. Lett. **81**, 2261 (2002).

[31]"*Here, ON/OFF ratio is limited by the dynamic range of our measurement setup.*",

[32]H. Ustunel, D. Roundy, and T. A. Arias, "*Modeling a suspended nanotube oscillator*", Nano Lette. **5**, 523 (2005).

[33]V. Sazonova *et al.*, "*A tunable carbon nanotube electromechanical oscillator*", Nature **431**, 284, (2004).

CHAPTER 4

CAPACITIVE SPRING SOFTENING IN SINGLE-WALLED CARBON NANOTUBE NANOELECTROMECHANICAL RESONATORS

4.1 Introduction

Limited by nanotubes' extremely small cross section, an electrical measurement in conjunction with the mixing technique is usually adopted [1] to measure the resonance of SWNT resonators. This electrical approach enable us to actuate and detect SNWT resonators simultaneously on a single chip through capacitive gate coupling, offering in situ frequency tuning over wide frequency range [2-4]. In this chapter, the gate-induced frequency tuning is studied, which is known to be governed by two mechanisms: the elastic hardening effect which increases the resonance frequencies, and the capacitive softening effect which decreases the resonance frequencies [5-6]. The basic concepts of both mechanisms are introduced in section 4.2. However, although elastic hardening effect has been widely reported in SWNT resonators [1, 7-8], the field-induced capacitive spring softening has rarely been observed [9]. In section 4.3, we demonstrate the capacitive spring softening effect in SWNT resonators by utilizing a dual-gate configuration containing both bottom-gate (BG) and end-gate (EG) capable of tuning the resonance frequency through capacitive coupling. Downward resonance frequency tuning is observed with increasing end-gate voltage, which is attributed to the capacitive softening of the spring constant. Furthermore, SWNT resonators are known to exhibit multiple vibrational modes, in-plane and out-of-plane, and their higher order modes [10]. In our dual-gate configuration, the in-plane modes are expected to reveal a much stronger capacitive softening effect than the fundamental out-of-plane mode, suggesting that our results also provide an experimental tool for differentiating vibrational modes (see section 4.4). Lastly, we investigate how the coupling between BG and EG affects the capacitive softening effect in section 4.5.

4.2 Frequency tuning mechanisms

It has been well studied that the gate-induced frequency tuning of NEMS resonators is governed by two mechanisms: The elastic hardening effect originated from the increased tension on the beam will increase the resonance frequencies. The capacitive softening effect caused by a beam oscillating in a constant electric field can reduce the effective spring constant, leading to the decrease of the resonance frequencies [5]. These two mechanisms can be explained more explicitly by the equation of motion of the beam, where the electrostatic force, attracting the beam towards the gate, and the elastic restoring force, trying to pull the beam back to its undeformed state, are included. The equation of motion is expressed as:

$$EIu_{xxxx} - [T_0 + T(u_x)]u_{xx} + \rho S u_{tt} = \frac{1}{2} C_z [z(x,t)] V^2 \qquad (4.1)$$

, where total displacement $u(x, t)$ is a sum of a static DC displacement $z_s(x)$ and a time-varying AC displacement $z(x,t)$ and written as $u(x, t) = z_s(x)+z(x,t)$. S is the beam's cross-sectional area, E is Young's modulus of the material, ρ is the beam density, and I is the moment of Inertia. The total tension term in brackets is a sum of residual tension T_0 and bending-induced tension $T(u_x)$. The frequency can be solved and expressed as:

$$\omega_0^2 = [\frac{EI}{3\rho S} + \frac{EA_{dc}^2}{6\rho}](\frac{2\pi}{L})^4 + \frac{T_0}{3\rho S}(\frac{2\pi}{L})^2 - \frac{K_2 V^2}{\rho S} \qquad (4.2)$$

The different frequency tuning behaviors can be explained from equation (4.2). If the direction of electrostatic force is perpendicular to the motion of the beam, there is no electrostatic interaction between the motion and the electrostatic force (the K_2V^2 term is zero). Therefore, the frequency increases because increasing the gate voltage only stretches the beam to increase the tension of beam and then increases the static displacement A_{dc}. However, on the other hand, if the direction of the motion of the beam is parallel to electrostatic force, both stretching (increase in A_{dc}) and electrostatic interaction (described by the K_2V^2 term and will lead to the decrease of frequency) have to be included. Electrostatic attraction to the gate has a softening effect on the beam for low gate voltages. As the gate voltage continues increasing, the hardening due to stretching will overcome it and lead to the increase of resonance frequency again.

4.3 Capacitive spring softening effect in SWNT resonators

The elastic hardening effect in SWNT resonators has been widely reported everywhere. However, the field-induced capacitive spring softening effect has rarely been observed, since in a conventional SWNT resonator [1-2, 7], only the bottom-gate is used for frequency tuning. The motion of nanotube is perpendicular to the electric field, resulting in negligible spring softening. To this end, we demonstrate SWNT resonators with a dual-gate configuration, which enables both upward and downward frequency tuning by exploring both elastic hardening and capacitive softening effects.

4.3.1 Dual-gate SWNT resonators

Our SWNT resonators with a dual-gate configuration are fabricated using our one-step direct transfer technique. Figure 4.1(a) shows the SEM image of a typical dual-gate SWNT resonator. Suspended nanotube (indicated by the arrow) spans across the source (S) and drain (D) electrodes (in green) with an underneath bottom-gate and nearby end-gates electrostatically coupled to the nanotube. For a typical device, the S and D electrodes are 2 μm wide, separated by 3 μm, and the distance between nanotube and the BG is 1 μm. To explain how our dual-gate nanotube resonators can realize frequency-tuning through elastic hardening and capacitive softening mechanisms, a qualitative sketch is illustrated in figure 4.1(b). SWNT resonators exhibit two types of vibration modes: the in-plane mode (left-top panel) moves along the y-direction, and the out-of-plane mode (right-top panel), vibrating like a jumping rope, moves along the x-direction. The details of in-plane and out-of-plane modes will be described in next section. When a voltage V_{bg} is applied on the BG electrode, the electrostatic force will pull down the nanotube toward the gate (gray arrow, along the z-direction), thus increasing the nanotube’s tension and resulting in elastic hardening. Since the electrostatic force is perpendicular to the vibration directions of both in-plane and out-of-plane modes, the effect of capacitive softening is negligible. On the other hand, when an end-gate voltage V_{eg} is applied, the electrostatic force (red arrow) will have component along y-direction in addition to z-direction. As the result, the in-plane vibrational modes will be impeded by the electrostatic force, leading to a strong capacitive softening effect compared to out-of-plane mode. Our dual-gate resonator design differs from previous work [5-6], where the second gate electrode (side-gate) is also perpendicular to the resonator beam. The adoption of end-gate design drastically reduces the fabrication complexity, also enhances the softening effect for the in-plane vibrational modes.

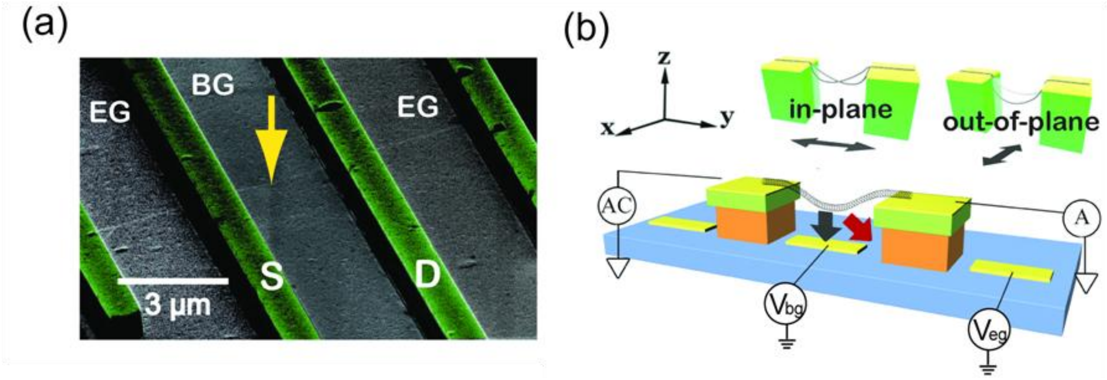

Figure 4.1. Device geometry of a dual-gate SWNT resonator. (a) The SEM image of SWNT NEM resonators. The source and drain electrodes are colorized (green) and 50-nm-thick Au is used as the bottom-contact metal. The arrow indicates the position of a suspended SWNT. (b) A qualitative sketch illustrates how electrostatic force interacts with different resonance modes when a bias voltage is applied on BG or EG electrodes.

4.3.2 Tuning the resonance frequency

To experimentally examine these two frequency tuning mechanisms, we systematically apply voltages on both bottom-gate and end-gate electrodes. Again, we adopt the single-source mixing measurement setup (AM modulation, section 2.5) to detect the resonance frequency of the nanotube resonator by measuring the frequency-dependent mixing current (I_{mix}). The measurement is done in a vacuum chamber at pressure below 10^{-4} torr and a small AC driving voltage (V_{sd}) of 10 mV is applied to the drain electrode to actuate the SWNT resonator through electrostatic interaction.

A. Elastic hardening effect

We first studied the frequency tuning using bottom-gate electrode. As shown in figure. 4.2(a) inset, nanotube resonances are clearly visible, and resonance frequency increases from 11 MHz to 22 MHz as $|V_{bg}|$ increases from 0 V to 2 V. We further extract resonance frequencies at different V_{bg} between -2V to 2V, and the results can be fitted with a parabolic function [Fig. 4.2(a)]. Our observation of frequency tuning using BG electrode agrees well with elastic hardening effect reported on nanotube resonators. At small BG voltages, the nanotube resonators operate in the bending regime, in which resonance frequency f depends quadratically on the BG voltages. The reonant frequency at bending regime can be fit by [9]:

$$f = f_0 + 0.28 \frac{C'}{\sqrt{96s}} \sqrt{\frac{1}{\mu EI}} V_{bg}^2 = f_0 + AV_{bg}^2 \qquad (4.3)$$

, where f_0 is the fundamental frequency, C' is the first derivative of capacitance to nanotube/gate distance, s is the slack, μ is linear mass density, E is Young's modulus, I is the moment of inertia, and A is termed as elastic hardening tuning coefficient. Fitting the experimental data in figure 4.2(a) with equation (4.3) yields measured coefficient A of 1.9×10^6 HzV^{-2}. To compare $A_{measured}$ with the theoretical value A_{theory}, we adopted a cylinder over a metal plane to model the capacitance $C = \frac{2\pi\varepsilon_0 L}{\ln(\frac{2Z}{d})}$, where ε_0 is the dielectric constant; L is the nanotube length; Z is the separation between tube and bottom electrode; d is the diameter of nanotube. Assuming a small slack of 1% and using typical SWNT parameters listed in Table 4.1, the A_{theory} value calculated using equation (4.3) is 2.5×10^6 HzV^{-2}, which agrees well with measured A.

B. *Capacitive softening effect*

Next, we examined the frequency dependence of end-gate voltage [Figure. 4.2(b)]. Interestingly, as shown in figure 4.2(b) inset, nanotube resonance frequency decreases as $|V_{eg}|$ increases. The extracted resonance frequencies at different V_{eg} between -10V to 10V exhibit a negative curvature with increasing field. The observed downward frequency tuning by EG is in strong contrast to elastic hardening, but it can be explained by the capacitive softening effect. To analyze the capacitive softening effect, we start from $f = (\frac{1}{2\pi})\sqrt{\frac{k}{m}}$, where k and m are the spring constant and mass of the nanotube. Since the capacitive softening effect will reduce the effective spring constant, the resonance frequency can be rewritten as $f = (\frac{1}{2\pi})\sqrt{\frac{k - k_{softening}}{m}}$, where $k_{softening}$ is the derivative of electrostatic force, and is written as $k_{softening} = \frac{1}{2}\frac{d^2C}{dz^2}V_{gate}^2$. Substituting $k_{softening} = \frac{1}{2}\frac{d^2C}{dz^2}V_{gate}^2$ into $f = (\frac{1}{2\pi})\sqrt{\frac{k - k_{softening}}{m}}$ and $m=\mu L$, then the frequency dependence of the capacitive softening effect can be expressed as:

$$f^2 = f_0^2 - \frac{C''V_{eg}^2}{8\mu L\pi^2} = f_0^2 - BV_{eg}^2 \tag{4.4}$$

, where C'' is the second derivative of capacitance, and B is termed the capacitive softening coefficient. Again, fitting the experimental data in figure 4.2(b) with equation (4.4) yields the measured coefficient B of $0.8\times10^{12}\,\mathrm{Hz}^2\mathrm{V}^{-2}$. To calculate the theoretical value of B_{theory}, a finite-element simulation (COMSOL) is performed to obtain C'' for EG. The structure for simulation in COMSOL is illustrated in figure 4.3. Using typical SWNT parameters listed in Table 4.1 and C'' obtained from simulation, we calculate a B_{theory} from equation (4.4) of $0.96\times10^{12}\mathrm{Hz}^2\mathrm{V}^{-2}$, which agrees well with measured B. Similar results have been observed on 3 dual-gate resonators, offering a reliable approach for studying both elastic hardening and capacitive softening effects in nanotube resonators for the first time.

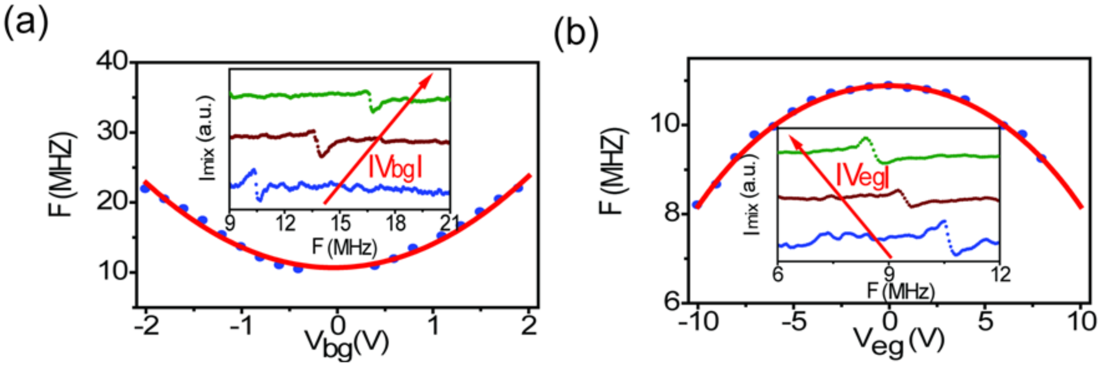

Figure 4.2. Resonance characteristics of a dual-gate SWNT resonator. (a) Elastic hardening effect, and (b) Capacitive softening effect, observed on a SWNT resonator by biasing BG and EG, respectively. Insets of (a) and (b): mixing current (I_{mix}) vs. driving frequency (f) at different BG and EG voltages. Resonance peak shifts to higher frequency as $|V_{bg}|$ = 0.5, 1, and 1.5V is applied, and shift to lower frequency as $|V_{eg}|$ = 3, 7, and 9V is applied.

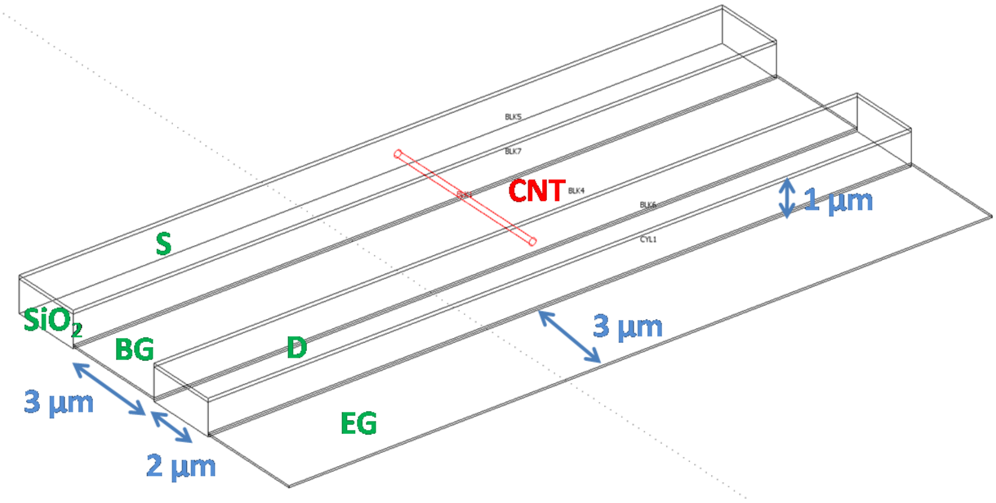

Figure 4.3. Modeling geometry for finite-element simulation of capacitance.

Parameter	Symbol	Value
Diameter	d	2nm
Length	L	3μm
Slack	s	1%
Elastic modulus	E	1TPa
Linear mass density	μ	5×10^{-15} (kg/m)
Moment of inertia	I	7×10^{-37}
Dielectric constant	ε_o	8.85×10^{-12}
Distance between CNT and BG	Z	1μm

Table 4.1. Key values of nanotube parameters used for numerical calculation.

4.4 Capacitive softening effect on different vibrational modes

SWNT resonators are known to exhibit multiple vibrational modes, including in-plane, out-of-plane, and their higher order modes. The behaviors of these vibrational modes have been studied both theoretically and experimentally [9-10]. Here, we reproduce the definition of both modes. The in-plane mode (left-top panel, figure 4.1(b)) moves along the y-direction, and the out-of-plane mode (right-top panel, figure 4.1(b)), vibrating like a jumping rope, moves along the x-direction. In principle, the in-plane and out-of-plane modes are degenerated at zero slack. However, with finite slack there will be frequency discrepancy between them due to the symmetry broken. In addition, the harmonics of both modes can be excited with frequency increase accompanying with the increase of the number of nodes in each mode. Therefore, we should see several distinct resonance modes, the harmonics and the fundamental in-plane and out-of-plane modes, in a SWNT resonator. The resonance frequencies of these modes and their higher order harmonics have been predicted theoretically by considering the effect of slack, as shown in figure 4.4 [10].

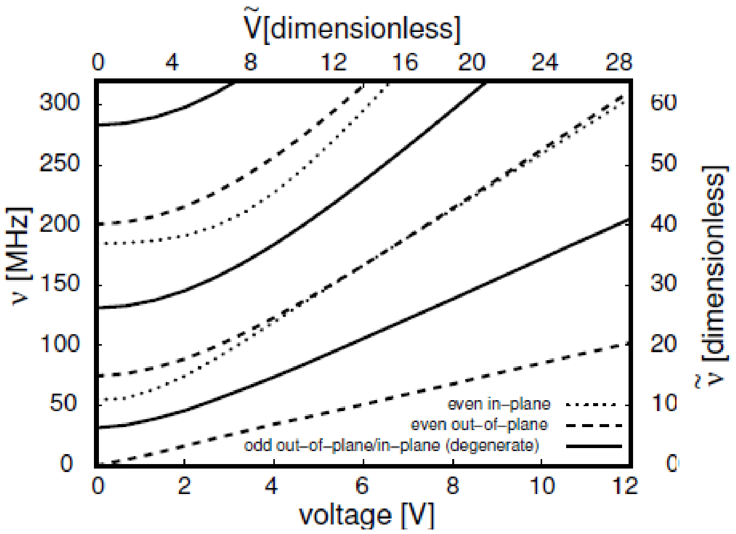

Figure 4.4. Numerical calculations of different vibrational modes. Fundamental and harmonics of in-plane and out-of-plane modes are calculated numerically [10]. The first vibrational mode is fundamental out-of-plane mode.

Based on this unique property in resonance, we therefore examined the capacitive softening effect on different vibrational modes. Figure 4.5(a) shows the mixing current (in color) plotted as a function of driving frequency and EG voltage. Three resonance modes are clearly visible with *f* up to 23MHz, and they all exhibit capacitive softening effect with applied V_{eg}. The V_{eg}-dependent resonance frequencies for all three modes are plotted in the inset of figure 4.5(a). Importantly, three vibrational modes show drastically different frequency tunability. Fitting the experimental data in figure 4.5(a) inset with equation (4.4) yields B = 0.16, 0.8, and $0.76\times10^{12}\text{Hz}^2\text{V}^{-2}$ for vibrational modes from bottom to top, respectively. The two higher frequency modes exhibit ~5 times larger capacitive softening effect compared to the lowest frequency mode. Similar measurements were performed on 3 other SWNT resonators with the same device geometry, and the results are shown in figure 4.5(b). The softening coefficients for the first vibration modes are always much smaller than those of higher order modes, differed by 4 to 6.3 times. This observation agrees with our qualitative analysis shown in figure. 4.1(b), where differences in softening coefficients are expected for in-plane and out-of-plane modes. Therefore, we attribute the first vibrational mode with much smaller softening coefficient as out-of-plane mode, and the higher order vibrational modes with larger softening coefficients as in-plane modes. Our results also agree with the theoretical prediction of the first vibrational mode being the fundamental out-of-plane mode (seen figure 4.4).

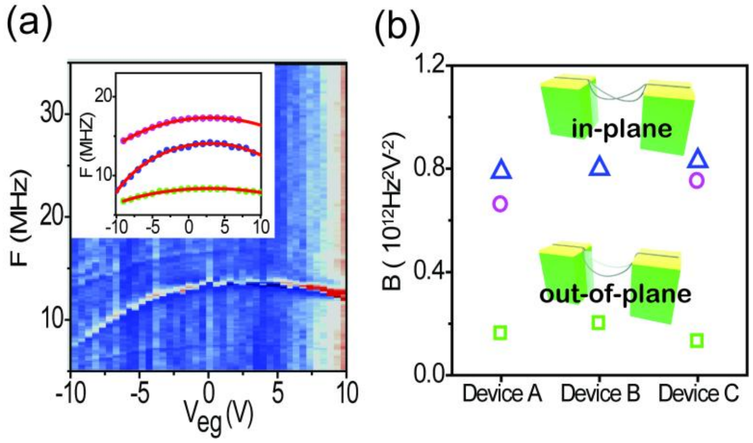

Figure 4.5. Capacitive softening effect on different vibrational modes. (a) Mixing current I_{mix} (color scale) is plotted as a function of driving frequency and V_{eg}. Inset: Resonance peaks (dots) of different modes are plotted with respect to V_{eg}. Red lines are fitting curves with equation (4.5). (b) Measured softening coefficients (*Bs*') of different modes for three resonators. The softening coefficients for the first vibration modes (green squares) are always much smaller than those of higher order modes (blue triangles and purple circles), differed by 4 to 6.3 times.

4.5 Coupling between BG and SG

Lastly, we investigated how the coupling of BG and EG affects the capacitive softening effect. A 2D plot of resonance frequency (in color) vs. V_{sg} and V_{eg} for the second vibrational mode is shown in figure 4.6(a). The resonance frequencies show symmetric tuning around gate voltages corresponding to the charge neutral point, although a shift of neutral point is clearly observed. Furthermore, the V_{eg}-dependent resonance frequencies for different fixed V_{bg} are plotted in figure 4.6(b). As $|V_{bg}|$ increases from 0V to 2V, the downward frequency tuning is again clearly visible, but the curves are shifted toward higher V_{eg} value. The shift rises from our dual-gate geometry, where the charge neutral point will shift as voltage being applied onto the EG. The capacitive softening equation can be modified by including the effect of elastic hardening and an offset voltage, V_0, to account for the effect of BG:

$$f^2 = f_0^{'2} - B(V_{eg} - V_0)^2 = (f_0 + AV_{bg}^2)^2 - B(V_{eg} - V_0)^2 \qquad (4.5)$$

Fitting data in figure 4.6(b) with equation (4.5), we extracted the softening coefficient B and offset voltage V_0, and the results are plotted in figure 4.6(c). The softening coefficient (red circles) remains nearly constant at different V_{bg} voltage, while V_0 (blue squares) varies linearly with respect to V_{bg}. A linear fit of V_0 vs. V_{bg} yields a slope of ~3, suggesting that the BG is about three times more effective than EG for electrostatic charging.

4.6 Summary

In summary, we report the observation of capacitive softening effect in SWNT resonators adopting a dual-gate configuration. While in-plane vibrational modes show strong softening effect when EG voltage is applied, the fundamental out-of-plan mode exhibits small/negligible spring constant softening. Our results not only provide a new experimental tool for differentiating nanotube vibrational modes, but also enable additional freedom for exploring non-linear effects in nanotube resonators. The capability of spring constant tuning by EG coupling enables parametric amplification for quality factor enhancement [11], and makes possible nanotube resonator based room temperature single molecule mass sensor.

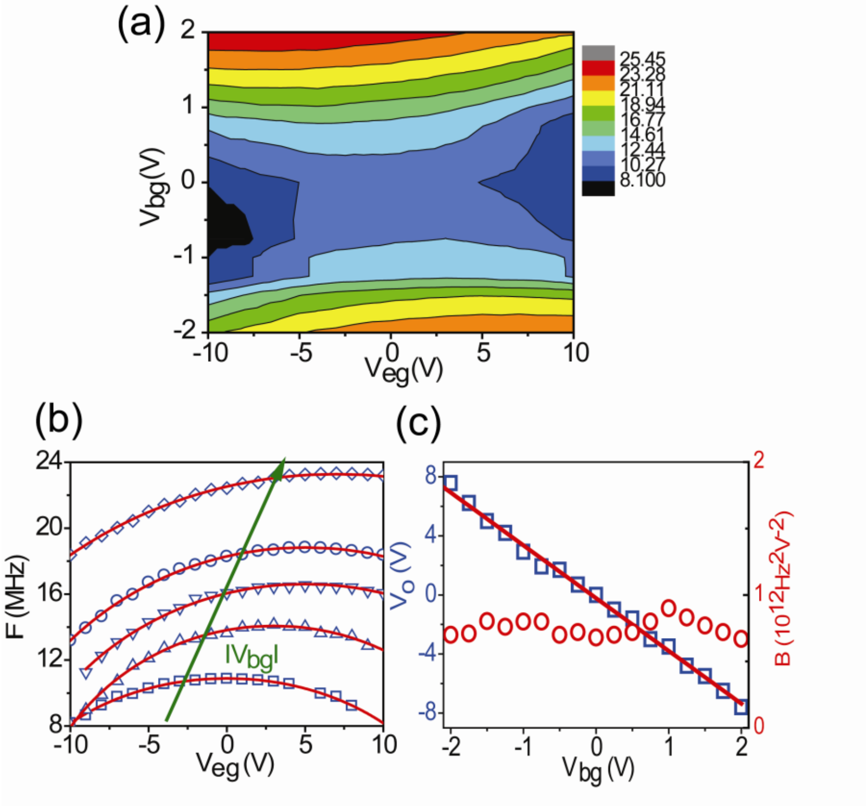

Figure 4.6. Dual-gate frequency tuning of SWNT resonators. (a) 2D plot of resonance frequency (in color) vs. V_{sg} and V_{eg} for the second vibrational mode. (b) Resonance frequencies (blue dots) vs. V_{eg} curves for V_{bg} = 0, -1, -1.25, -1.5, and -2V, from bottom to top. The neutral point V_0 shifts to higher voltages as $|V_{bg}|$ increases. (d) Offset voltage V_0 (blue squares) and coefficient B (red circles) vs. V_{bg} extracted from (c). A linear fit of V_0 vs. V_{bg} yields a slope of ~3.

*This chapter is written based on our work published in *Nano Letters, Volume 11, page 1448-1551, 2011*.

REFERENCE

[1]V. Sazonova *et al.*, "*A tunable carbon nanotube electromechanical oscillator*", Nature **431**, 284 (2004).

[2]H. B. Peng *et al.*, "*Ultrahigh frequency nanotube resonators*", Phys. Rev. Lett. **97**, 087203 (2006).

[3]H. Y. Chiu *et al.*, "*Atomic-scale mass sensing using carbon nanotube resonators*", Nano Lett. **8**, 4342 (2008).

[4]K. Jensen, K. Kim, and A. Zettl, "*An atomic-resolution nanomechanical mass sensor*", Nat. Nanotech. **3**, 533 (2008).

[5]I. Kozinsky *et al.*, "*Tuning nonlinearity, dynamic range, and frequency of nanomechanical resonators*", Appl. Phys. Lett. **88**, 253101 (2006).

[6]W. Y. Fung, E. N. Dattoli, and W. Lu, "*Radio frequency nanowire resonators and in situ frequency tuning*", Appl. hys. Lett. **94**, 203104 (2009).

[7]B. Witkamp, M. Poot, and H. S. J. van der Zant, "*Bending-mode vibration of a suspended nanotube resonator*", Nano Lett. **6**, 2904 (2006).

[8]C. C. Wu, C. Liu. , and Z. Zhong, "*One-step direct transfer of pristine single-walled carbon nanotubes for functional nanoelectronics*", Nano Lett. **10**, 1032 (2010).

[9]V. Sazonova, "*A Tunable Carbon Nanotube Resonator*", PhD. Thesis, Cornell University, Ithaca, NY (2006).

[10]H. Ustunel, D. Roundy, and T. A. Arias, "*Modeling a suspended nanotube oscillator*", Nano Lett. **5**, 523 (2005).

[11]D. Rugar, and P. Grutter, "Mechanical parametric amplification and thermomechanical noise squeezing", Phys. Rev. Lett. **67**, 699 (1991).

CHAPTER 5
PARAMETRIC AMPLIFICATION IN SINGLE-WALLED CARBON NANOTUBE NANOELECTROMECHANICAL RESONATORS

5.1 Introduction

Owing to their low mass and high operating frequency, nanoelectromechanical systems are expected to have excellent sensitivities in ultrasmall mass and force sensing and mass sensitivity below a single Delton has been predicted theoretically [1-6]. In principle, the minimum detectable mass (Δm) is proportional to the effective mass of the system and limited by the readout frequency resolution, which can be approximated by ω_0/Q. Therefore, we can roughly express Δm as $\Delta m = 2\frac{m_{eff}}{Q}$. For better mass sensitivity, one would prefer a resonator with the lightest mass and the highest *Q*. As a result, SWNT resonators standing out with one of the highest Young's modulus and the lightest effective mass are considered as promising candidates to achieve this ultimate goal. Unfortunately, the mass sensitivity of SWNT resonators is impeded by their poor *Qs*, usually around 100 at room temperature [7-10], indicating the importance of enhancing *Q* for nanotube resonators as mass sensors.

The origin of dissipation in nanotube resonators that causes low *Q* is still unknown currently and several possible dissipations have seen suggested. In section 2.6, we discussed that surface loss increases linearly with the increasing surface-to-volume ratio and plays an important role in determining *Q* of nanometer-scale resonators. Another possible loss mechanism is that strain in nanostructure will generate local temperature difference, leading to irreversibly heat flow along local temperature gradients and inducing the thermoelastic damping [11-12]. A recent study has shown that low *Qs* and temperature-dependent behavior are due to the thermal fluctuations of many vibrational modes, called entropic broadening effect [13]. More details about losses in nanotube resonators will be discussed in section 5.2. If low *Qs* are limited by the fundamental constrains, the solution to improve nanotube resonators' sensitivity will be to seek an external way to enhance the *Q*. To this end, we utilized the concept of parametric amplification for *Q* enhancement.

The concept of parametric amplification will be described in section 5.3. In section 5.4, we demonstrate parametric amplification in SWNT resonators by modulating the spring constant of nanotubes at twice the resonance frequency through electrostatic gating, and achieve 10 times *Q* enhancement. The highest *Q* obtained at room temperature is around ~700, which is 3-4 times better than previous *Q* reported for doubly-clamped SWNT resonators. Furthermore, efficient parametric amplification is found to only occur in the catenary vibrational regime and details will be discussed in section 5.5. Lastly, we examine the threshold voltage (V_t) of parametric amplification in section 5.6. The experimental results show good agreement with the theoretical V_t values, suggesting the possibility to predict and control V_t . Our results open up the possibility to employ light-weight and high-*Q* carbon nanotube resonators in single molecule and atomic mass sensing.

5.2 Losses in carbon nanotube resonators

The actual dissipations in nanotube resonators resulting in low *Qs* are still unclear currently. They are believed to be a combination of several loss mechanisms. Here, we summarized previous studies and listed the potential dissipations below.

A. Entropic spectral broadening

Entropic broadening effect is that thermal fluctuations will induce strong coupling between resonance modes. This will lead to spectral fluctuations and contribute to low *Qs* and resonance frequency peak shift observed in resonators. In other words, this effect becomes more dominant for resonators with small bending rigidity (k), since they are expected to have larger fluctuations in thermal equilibrium. Specifically, the quality factor and frequency shifts are arising from the change in length caused by thermal fluctuation of each resonance mode. The change in length leads to the strain being modified; thus, the first and second moment of the strain shift ($\Delta\varepsilon$ and σ_ε^2) will account for the frequency shift and quality factor, respectively. The $\Delta\varepsilon$ and σ_ε^2 are expressed as:

$$\Delta\varepsilon = \frac{L}{2n_f l_p}; \quad \sigma_\varepsilon^2 = \frac{L^2}{8n_f^3 l_p^2}; \quad n_f = \sqrt{\frac{NL^2}{k}} \tag{5.1}$$

, where L is the beam length, n_f is the number of independent degrees of freedom with significant fluctuation amplitudes, l_p is the persistence length, N is the axial tension and k is the bending rigidity. From equation (5.1), $\Delta\varepsilon$ leads to $\Delta f \sim T$ and the strain variance σ_ε^2 predicts that $\delta f\,(Q^{-1}) \sim T$. The δf prediction constitutes entropic spectral broadening and Q^{-1} can be further predicted by:

$$Q^{-1} = \frac{\sqrt{\ln 2}}{2}\frac{L}{n_f^{3/2}\varepsilon\, l_p} \tag{5.2}$$

With equation (5.2), the Q is calculated around 100 for nanotube resonators, closed to the experimentally observed Q. It agrees well with both low Q and temperature-dependent behavior so we believe it is the most likely loss in CNT resonators.

To determine if entropic broadening effect is significant in NEMS resonators, a key length-scale called persistence length $l_p=k/k_BT$ is defined. For short 1D structures with length $L<< l_p$, such as conventional NEMS resonators, they are dominated by elastic effects and thus behave like rigid rods. On the other hand, for long 1D structures with $L>>l_p$, such as organic polymers, they will be dominated by configurational entropic effects. For a typical micron-scale nanotube resonators, the diameter is usually around few nanometers, yielding to a much smaller bending rigidity for flexural modes and thus its length is closed to the persistence length ($L \leq l_p$). As a result, they will behave as semi-flexible polymers, where the bending energy and configurational entropy will contribute comparably to the total free energy.

B. Thermoelastic effect

A normal vibration mode of an elastic resonator will experience damping due to their nonlinear interaction with surrounding elastic modes excited thermally, or phonons. When a resonator is vibrating, the solid is taken out of equilibrium, having an excess of kinetic and potential energy. The coupling of the strain field to a temperature field provides an energy dissipation mechanism that allows the system to relax back to equilibrium. Relaxation is achieved through the irreversible flow of heat driven by local temperature gradients that through the coupling accompany the strain field. This process of energy dissipation is called thermoelastic damping.

The thermoelastic effect can be expressed by a standard model. The dissipation strength is given by

$$\Delta = \frac{\alpha^2 TE}{C} \quad (5.3)$$

, where α is the thermal expansion coefficient, T is the temperature, E is elastic modulus, C is the heat capacity. So the overall value of loss is given by

$$Q^{-1} = \frac{\alpha^2 TE}{C}\left(\frac{\omega\tau}{1+(\omega\tau)^2}\right) \quad (5.4)$$

In previous study, *Q* around 400 is calculated with equation (5.4), setting up the upper bound of quality factor of carbon nanotube resonators. The calculated *Q* is also closed to experimentally observed *Q*, meaning that it may also be a potential dissipation in nanotube resonators.

C. Surface loss

It has been observed that the measured quality factors decrease in a linear fashion as the surface-to-volume ratio increases, directly indicating that the surface loss plays an important role in determining the quality factor. Those surface defects can be adsorbed molecules, dangling bonds, or amorphous oxide layers that occur at the surface of a resonator. They will absorb energy from the fundamental resonance mode and transfer it to other modes and thermal energy that induce dissipation. Nanotube resonators follow this distributing trend, implying that surface loss may be the main dissipation. However, for resonators made out of pristine nanotubes, surface loss (dangling bond, surface defects) should be eliminated. Moreover, nanotube resonators fabricated by different process methods show similar *Q*, further proving that low quality factors are limited by other loss mechanisms rather than surface loss. Most importantly, the Q of nanotube resonators has strong temperature-dependent behavior, which cannot be explained by surface loss.

5.3 Parametric amplification

Conceptually, parametric resonance is excited by a time-varying modulation of a system parameter. A common example of parametric resonance is a pendulum, with the length of the cord changing with time. If the length decreases when the pendulum is in the lower position and increases in the upper position, oscillations of the pendulum will build up. The first application of parametric amplification in a mechanical resonance system was demonstrated by Rugar and Grütter [14]. In their work, parametric amplification in a mechanical cantilever was obtained by periodically modulating the spring constant on the basis of gate capacitive coupling. Thereafter, numerous studies based on parametric amplification in NEMS resonators have been conducted by many other schemes, for example, exploiting stress via piezoelectric electromechanical coupling [15] or a Lorentz force [16].

To understand parametric amplification in SWNT resonators, we start from the equation of motion. It has been shown that nonlinear damping [17] is highly important for SWNT and graphene resonators [18]. Here for simplicity, we drop the nonlinear damping terms and model the SWNT resonator as a classical driven damped harmonic oscillator with a time-varying spring constant. The equation of motion is then expressed as is expressed as [14]:

$$m\frac{d^2x}{dt^2}+\frac{m\omega_0}{Q}\frac{dx}{dt}+[k_0+k_p(t)]x=F(t) \tag{5.5}$$

, where x is the displacement of the nanotube , $F(t)$ is the external driving force, Q is the quality factor, ω_0 is the resonance frequency, k_0 is the unperturbed spring constant, and k_p is the modulated spring constant created by electrostatic coupling, written as $k_p=\Delta k\ sin2\omega_0 t$. m, k_0, and ω_0 are related by $k_0=m\omega_0^2$. To solve the equation (5.5), the normal mode approach described by Louisell is used and details can be found in Rugar and Grütter's work [14]. The parametric amplification will lead to a vibration amplitude gain (G) given by [14]:

$$G = \left[\frac{\cos^2\phi}{(1+V_p/V_t)^2} + \frac{\sin^2\phi}{(1-V_p/V_t)^2} \right]^{1/2} \tag{5.6}$$

, where ϕ is the phase between the driving and pumping signals, V_t is the threshold voltage determined by the system parameters, and V_p is the pumping voltage for parametric amplification. The equation (5.6) shows that the gain is phase sensitive and gain will increase as V_p approaches V_t when an appropriate ϕ is satisfied, as shown in figure 5.1(a). For ϕ =π/2 (black curve) and ϕ =π/6 (green curve), gain increases as V_p approaches to V_t. But For $\phi = 0$, the gain is always less then unity and decreases as V_t increases; For different fixed V_p (figure 5.1(b)), the maximum gain occurs at $\phi = \pi/2$, and the minimum is always at $\phi = 0$.

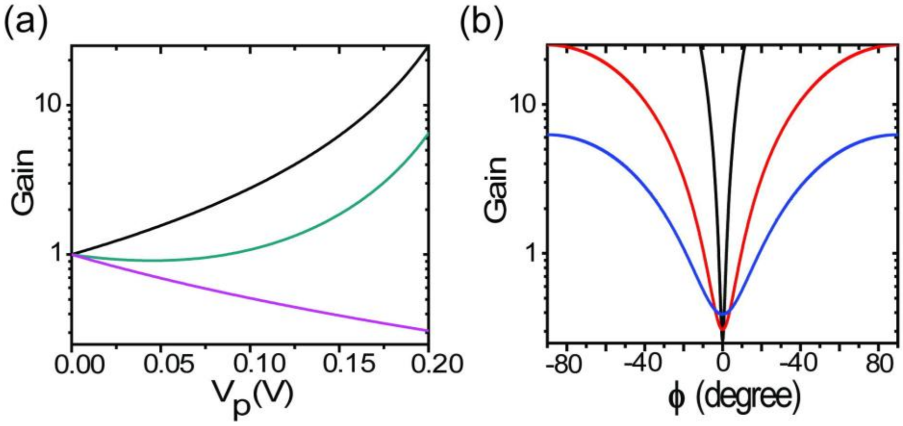

Figure 5.1. Simulation results of parametric amplification. For ϕ =π/2 (black curve) and ϕ =π/6 (green curve), gain increases as V_p approaches V_t. But for $\phi = 0$ (purple curve), the gain is always less than 1 and decreases as V_t increases (b) In fixed V_p case, for different fixed V_p, the maximum gain occurs at $\phi = \pi/2$, and the minimum is at $\phi = 0$.

5.4 Parametric amplification in SWNT resonators

5.4.1 Device fabrication

To experimentally verify the parametric amplification in SWNT resonators, we fabricated SWNT resonators using our one-step direct transfer technique. For a typical device, the source and drain electrodes are 2 μm wide, separated by 3 μm, 50 nm Au is used as contact metal, and the distance between nanotube and the bottom gate is 1 μm. The SEM image of a typical resonator is shown in figure 5.2(a).

5.4.2 Measurement setup

To actuate and detect resonance signals from our SWNT resonators, we employ the frequency modulation (FM) single-source mixing technique [19] instead of amplitude modulation (AM) method [20] in our measurement setup, as shown in figure 5.2(b). For external FM modulation, a small signal from a lock-in amplifier (Stanford Research SR830) at low frequency (616.3Hz) is sent to the RF signal generator (Agilent 8648B). The FM signal is then sent to the source electrode to actuate the resonance and the mixing current from the drain electrode is measured by the lock-in amplifier. To achieve parametric amplification, the second AC voltage (pumping voltage, V_p) from the second RF signal generator (Agilent 8648C) at twice the resonance frequency $2f_0$ is added to the DC gate voltage through a bias-T, and is applied to the gate electrode to modulate the spring constant of the nanotube. We note that the FM mixing technique is chosen as the detection technique because of its better noise-rejection in comparison to the AM method and the background current is zero (an advantage in detecting resonance). In addition, since noise is affected by the amplitude variation, higher noise level is expected for AM method. The results of parametric amplification achieved by both AM and FM techniques are plotted in figure 5.2 (c) for comparison. For the same device with identical DC gate voltage (V_g) and driving voltage (V_{sd}) applied, we observed that for same pumping voltage (V_p = 50 mV), there is rare enhancement appearing in AM measurement scheme (left panel). On the other hand, a significant peak enhancement shows up when FM is adopted (right panel).

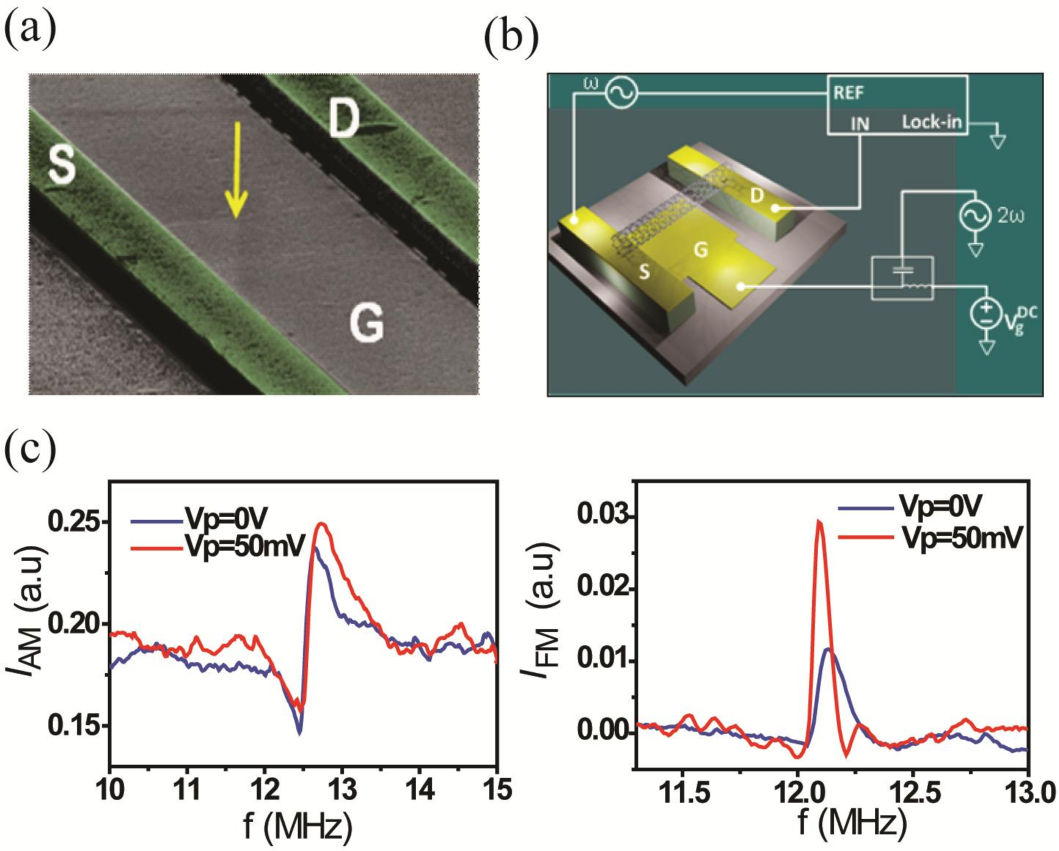

Figure 5.2. Experimental setup of parametric amplification. (a) SEM image of a typical SWNT resonator. (b) Schematic of the experimental setup for parametric amplification in SWNT resonators. (c) The comparison of AM and FM technique for parametric amplification. Left panel: parametric amplification measurement conducted by using AM method. No obvious peak enhancement shows up. Right panel: parametric amplification conducted by using FM method. A significant peak enhancement appears and the linewidth is reduced, indicating a *Q* enhancement.

5.4.3 Demonstration of parametric amplification

To demonstrate parametric amplification, the SWNT resonator is measured in a vacuum chamber at pressure below 10^{-4} torr and δV_{sd} = 20 mV is applied to drive the nanotube. The mixing current as a function of driving frequency at different pumping voltages are plotted in figure 5.3(a). At V_p= 0, we observe a nanotube resonance at f_0 = 23.1 MHz with a poor Q of 24±1. As we increase the V_p at $2f_0$ frequency, resonance peak amplitude is significantly enhanced and peak width is reduced, indicating a Q enhancement. The quality factors are extracted by fitting the experimental data of figure 5.3(a) with [19]:

$$I(\omega)=\frac{2\omega(\omega^2-\omega_0^2-\frac{\omega_0^2}{Q})(\omega^2-\omega_0^2+\frac{\omega_0^2}{Q})}{[(\omega_0^2-\omega^2)^2+(\frac{\omega_0\omega}{Q})]^2} \qquad (5.3)$$

Figure 5.3(b) shows the Q (blue squares) and corresponding gain (Q_p/Q_0) (red triangles) at different V_p. A clear Q enhancement is observed as V_p gradually increases. The maximum enhancement of Q is achieved at V_p= 25 mV with Q=235±9 (blue curve), showing remarkably a 10-fold enhancement compared to the signal without pumping (red curve, Q=24±1). We further compare our Q value with previous works on doubly-clamped SWNT resonators [7-8, 10, 20-23]in Fig. 5.3(c). Overall, previous room temperature Q record is around 200, while our highest Q through parametric amplification is ~700 (marked as a star and the resonance signal with fitting curve is shown in figure 5.3(d)), showing at least three times improvement.

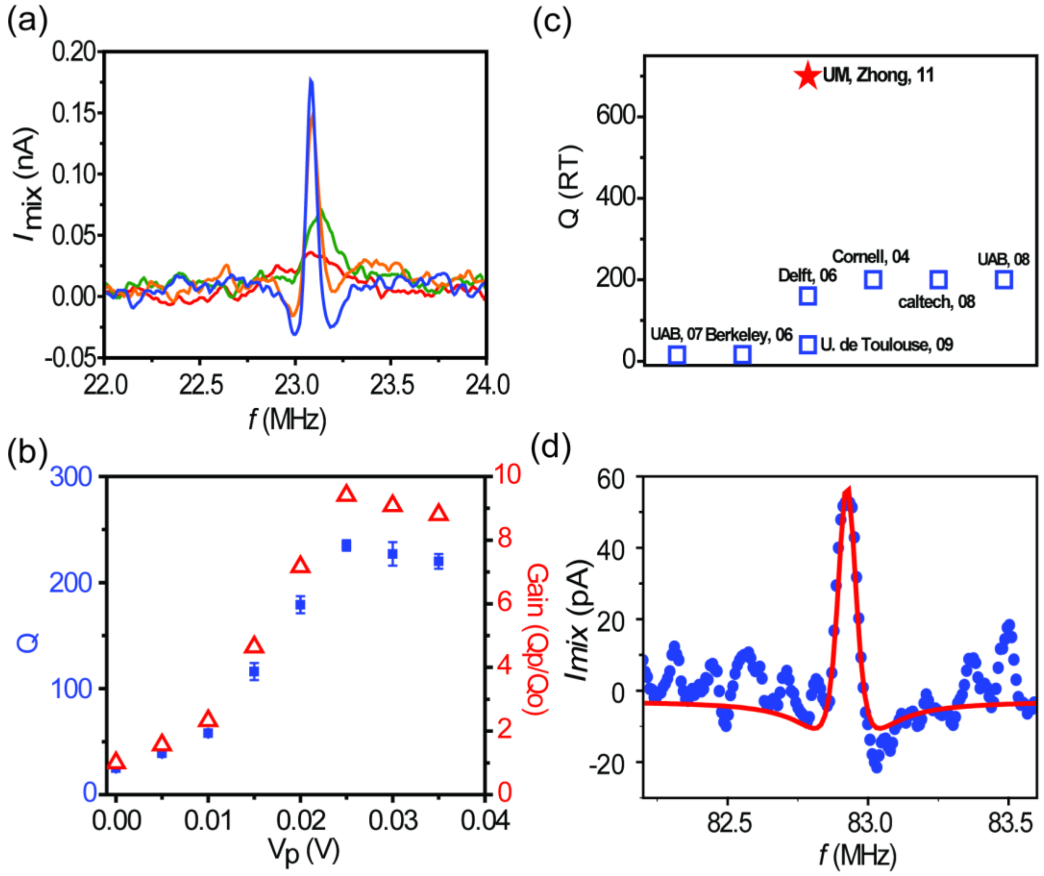

Figure 5.3. Demonstration of parametric amplification in SWNT resonators. (a) Frequency modulated mixing currents are plotted as a function of driving frequency at different pumping voltages ranging from 0 (red), 10 (green), 20 (orange), to 25 (blue) mV. Significant enhancement in peak current and quality factor was observed. (b) Q (blue squares) and gain (Q_p/Q_o) (red triangles) vs. V_p. The quality factor increases from 24±1 ($V_p = 0$ V) to 235 ±9 ($V_p = 25$ mV), corresponding to ~10 times enhancement of Q. (c) List of maximum Q's (blue squares) reported at room temperature in previous literatures. Our maximum Q achieved through parametric amplification is around 700 (marked as star) (d) the resonance signal (blue dots) with fitting curve (red).

5.5 *Dependence of DC gate voltage and AC driving voltage*

5.5.1 DC gate voltage dependence

Next, we examined effects of system parameters on parametric amplification by looking at the DC gate voltage dependence and the AC driving voltage dependence on parametric amplification. Figure 5.4 (a) and 5.4(c) show the maximum gains at different DC gate voltages obtained from two SWNT resonators, respectively. On both devices, we consistently observed effective parametric amplification with gain between 2 to 4 at higher DC gate voltages (blue triangles), but no amplification with gain ~ 1 at lower gate voltages (red triangles). To understand this disruption of parametric amplification, we plotted resonance frequency vs. V_g for both resonators in the figure 5.4(b) and 5.4(d), respectively. The resonance frequency is up-shifted at higher potential due to elastic hardening [21, 24-25], and two vibrational regimes, bending and catenary regimes, are clearly observed [26]. Comparing the gain obtained at different DC gate voltages with the corresponding vibration regimes, we found that efficient parametric amplification only occurs in the catenary regimes for both resonators. This can be explained by the much stronger spring constant modulation, $\frac{dk}{dV_g} \propto f \frac{df}{dV_g}$, in catenary regime. Extracting df/dV_g from figure 5.4(b) and 5.4(d) suggests 3~8 times greater frequency tunability in catenary regime than in bending regime. It is possible to achieve effective parametric amplification in the bending regime by applying large pumping voltage, in which case nonlinear effects need to be considered.

5.5.2 AC driving voltage dependence

We also examined the effect of excitation driving voltage (V_{sd}) on parametric amplification, and the results of maximum gain vs. V_p with different V_{sd} at a fixed DC gate voltage (V_g= -4 V) are plotted in Fig. 5.4(e). The experimental data did not reveal any dependence between maximum gain and V_{sd} when the V_{sd} was increased from 20 mV to 60 mV. This result is consistent with observations from previous work, where no dependence was observed between the gain and V_{sd} [15].

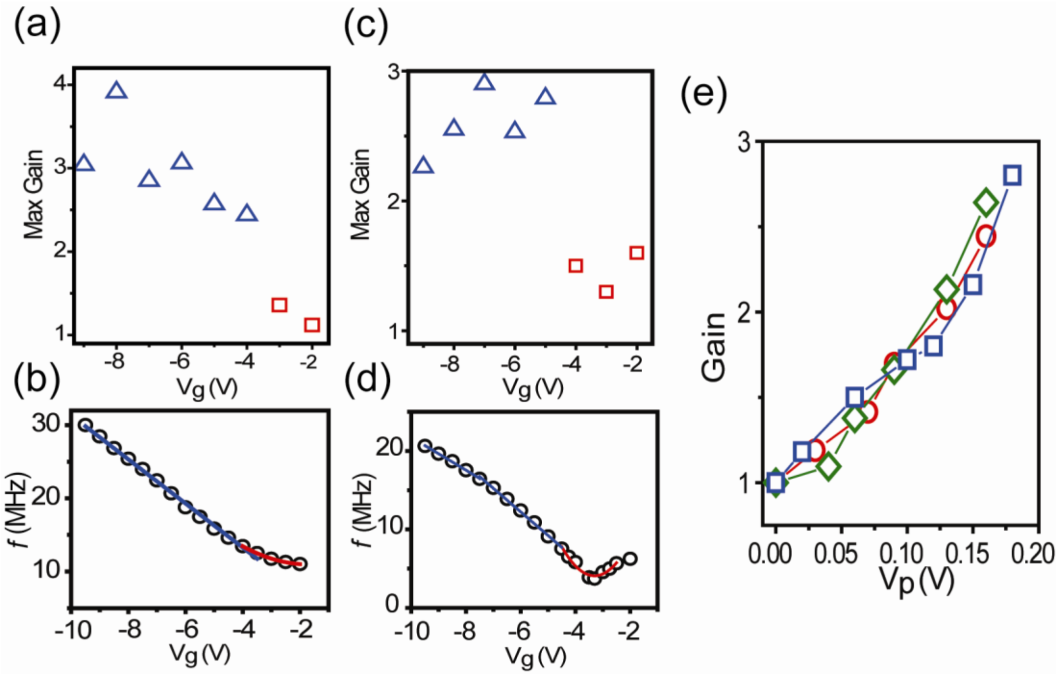

Figure 5.4. Maximum gain dependence on gate voltages and excitation voltages. (a), (c) Maximum gain vs. DC gate voltages of two SWNT resonators. The maximum gains are between 2~4 (blue triangles) in the catenary regime but drop to 1 (red squares) in the bending regime for both devices. (b), (d) The resonance frequency vs. DC gate voltages for two SWNT resonators. Two vibrational regimes, bending and catenary regimes, are shown clearly in both devices. (e), Gain vs. V_p at different driving voltages (V_{sd}) ranging from 20 (red), 40 (green) to 60 (blue) mV. No obvious dependence between gain and V_{sd} is observed.

5.6 *Threshold voltage of parametric amplification*

Last, we examine the threshold voltage for parametric amplification (V_t). As shown in figure 5.5(a), gain increases sharply with increasing V_p, agreeing with optimum parametric amplification near the threshold voltage. In order to extract V_t from the measurement data, we note that equation (5.2) is derived under fixed phase lag between driving and pumping. However, our two-source FM technique will introduce a time varying phase lag, and hence the overall gain is an average result due to random phases. Therefore, the average gain using our measurement technique can be written as

$$G = \frac{1}{2\pi}\int_0^{2\pi} G(\phi)d\phi = \frac{1}{2\pi}\int_0^{2\pi}\left[\frac{\cos^2\phi}{(1+V_p/V_t)^2}+\frac{\sin^2\phi}{(1-V_p/V_t)^2}\right]^{1/2} d\phi \tag{5.4}$$

Fitting data in figure 5.5(a) with equation (5.4), we find a V_t = 0.24 V at V_g = -5 V. Furthermore, the average gain under constant pumping frequency at $2\omega_0$ and varying driving frequency can be calculated using $G = (1-(V_p/V_t)^2)^{-1}$ from ref [17]. The analytical fitting (green curve) yields V_t = 0.23 V at V_g = -5 V, consistent with the numerical fitting result. We further extract V_t values under various V_g, and plot them in Fig. 5.5(b) (red squares). To model V_t dependence on V_g, we follow the derivation of Rugar and Grütter [14] and have V_t expressed as $V_t = 2k_0/QV_gC_g''$, where V_g is the DC gate voltage and C_g'' is the second derivative of the gate capacitance with respect to the distance between the nanotube and gate. To calculate the theoretical values of V_t, we adopt the cylinder over an infinite plane model for capacitance, $C = \dfrac{2\pi\varepsilon_0 L}{\ln(\frac{2Z}{d})}$, and the results are plotted as blue diamonds in figure 5.5(b). Detail parameters of

SWNT resonators are listed in Table 4.1. The experimental results show good agreement with the theoretical V_t values, suggesting the possibility to predict and control V_t by changing the device geometries and gate coupling. We also notice the deviation from the theoretical V_t at V_g = -6 V, and its origin is not clear at this time.

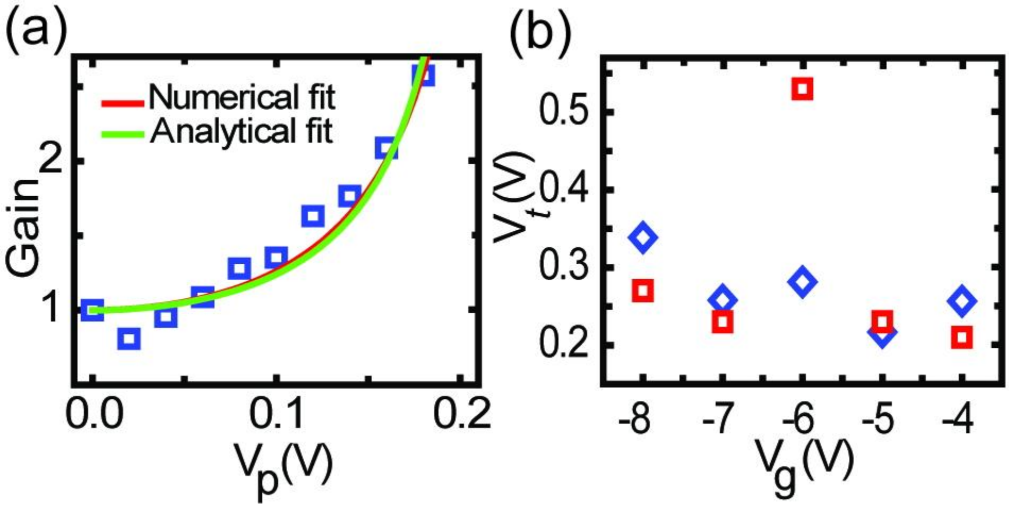

Figure 5.5. Threshold voltages of parametric amplification. (a) Gain (blue squares) vs. V_p at V_g= -5 V. The red curve is numerical fit by using equation (4), and V_t = 0.24 V is obtained. (b) Comparison of calculated V_t (blue diamonds) and measured V_t (red squares) at different gate voltages.

5.7 Summary

In summary, we employ the technique of parametric amplification by modulating the spring constant of SWNT resonators at twice the resonance frequency, and achieve 10 times *Q* enhancement. The highest *Q* obtained at room temperature is around ~700, which is 3-4 times better than previous *Q* reported for doubly-clamped SWNT resonators. Furthermore, efficient parametric amplification is found to only occur in the catenary regime due to the difference of frequency tenability at different vibration regimes. Our results enable the light-weight carbon nanotube as high-Q NEMS resonator for single molecule and atomic mass sensing. We also expect the parametric amplification technique can be applied to other low-Q NEM resonators suffering from intrinsic loss mechanisms, such as graphene resonators [27]. The $2f_0$ modulation through electrostatic gating offers a simple technique which can be easily adopted in various device geometries and the flexibility to be integrated with NEMS applications.

*This chapter is written based on our work published in *Applied Physics Letters, Volume 99, 083110, 2011*.

REFERENCE

[1]H. J. Mamin, and D. Rugar, "*Sub-attonewton force detection at millikelvin temperatures*", Appl. Phys. Lett. **79**, 3358 (2001).

[2]B. Ilic *et al.*, "*Attogram detection using nanoelectromechanical oscillators*", J. Appl. Phys. **95**, 3694 (2004).

[3]Y. T. Yang *et al.*, "*Zeptogram-scale nanomechanical mass sensing*", Nano Lett. **6**, 583 (2006).

[4]C. Hierold *et al.*, "*Nano electromechanical sensors based on carbon nanotubes*", Sens. Actuators A **136**, 51 (2007).

[5]A. K. Naik *et al.*, "*Towards single-molecule nanomechanical mass spectrometry*", Nat. Nanotech. **4**, 445 (2009).

[6]A. N. Cleland, "*Thermomechanical noise limits on parametric sensing with nanomechanical resonators*", New J. Phys. **7**, 235 (2005).

[7]H. B. Peng *et al.*, "*Ultrahigh frequency nanotube resonators*", Phys. Rev. Lett. **97**, 087203 (2006).

[8]H. Y. Chiu *et al.*, "*Atomic-Scale Mass Sensing Using Carbon Nanotube Resonators*", Nano Lett. **8**, 4342 (2008).

[9]K. Jensen, K. Kim, and A. Zettl, "*An atomic-resolution nanomechanical mass sensor*", Nat. Nanotech. **3**, 533 (2008).

[10]B. Lassagne *et al.*, "*Ultrasensitive mass sensing with a nanotube electromechanical resonator*", Nano Lett. **8**, 3735 (2008).

[11]K. Jensen *et al.*, "*Limits of nanomechanical resonators", IEEE nanoscience and nanotech., ICONN* 68 (2006)

[12]R. Lifshitz, and M. L. Roukes, "*Thermoelastic damping in micro- and nanomechanical systems*", Phys. Rev. B **61**, 5600 (2000).

[13]A.W. Barnard *et al.*, "*Entropic spectral broadening in carbon nanotube resonators*", arxiv: 1110.1517v1

[14]D. Rugar, and P. Grutter, " Mechanical parametric amplification and thermomechanical noise squeezing ", Phys. Rev. Lett. **67**, 699 (1991).

[15]R. B. Karabalin, S. C. Masmanidis, and M. L. Roukes, "*Efficient parametric amplification in high and very high frequency piezoelectric nanoelectromechanical systems*", Appl. Phys. Lett. **97**, 183101 (2010).

[16]R. B. Karabalin, X. L. Feng, and M. L. Roukes, "*Parametric nanomechanical amplification at very high frequency*", Nano Lett. **9**, 3116 (2009).

[17]R. Lifshitz, and M. C. Cross, "*Reviews of nonlinear dynamics and complexity*", Wiley-VCH vol. 1 (2008).

[18]A. Eichler *et al.*, "*Nonlinear damping in mechanical resonators made from carbon nanotubes and graphene*", Nat. Nanotech. **6**, 339 (2011).

[19]V. Gouttenoire *et al.*, "*Digital and FM demodulation of a doubly clamped single-walled carbon-nanotube oscillator: towards a nanotube cell phone*", Small, **6** 1060 (2010).

[20]V. Sazonova *et al.*, "*A tunable carbon nanotube electromechanical oscillator*", Nature **431**, 284 (2004).

[21]B. Witkamp, M. Poot, and H. S. J. van der Zant, "*Bending-mode vibration of a suspended nanotube resonator*", Nano Lett. **6**, 2904 (2006).

[22]D. Garcia-Sanchez *et al.*, "*Mechanical detection of carbon nanotube resonator vibrations*", Phys. Rev. Lett. **99**, 085501 (2007).

[23]B. Lassagne *et al.*, "*Coupling mechanics to charge transport in carbon nanotube mechanical resonators*", Science **325**, 1107 (2009).

[24]C. C. Wu, C. Liu, and Z. Zhong, "*One-step direct transfer of pristine single-walled carbon nanotubes for functional nanoelectronics*", Nano Lett. **10**, 1032 (2010).

[25]C. C. Wu and Z. Zhong, "*Capacitive spring softening in single-walled carbon nanotube nanoelectromechanical resonators*", Nano Lett. **11**, 1448 (2011).

[26]V. Sazonova, "*A Tunable Carbon Nanotube Resonator*", PhD. Thesis, Cornell University, Ithaca, NY (2006).

[27]J. S. Bunch *et al.*, "*Electromechanical resonators from graphene sheets*", Science **315**, 490 (2007).

CHAPTER 6

GRAPHENE ELECTROMECHANICAL RESONATORS

6.1 Introduction

The mass responsivity (R) defined by $(2m_{eff}/\omega_0)^{-1}$ is an important index to evaluate a resonator as a mass sensor. High R allows better mass sensitivity and is obtained with low m_{eff} and high ω_0. Thus, the ultimate NEMS structure will be a resonator with one-atom-thick beam and it has to be robust, stiff, and stable, suggesting that a resonator made out of graphene sheet would be a perfect candidate.

Graphene is a flat monolayer of carbon atoms tightly packed into a honeycomb lattice, and is very stiff due to the sp^2 carbon–carbon bonding. In addition, it is one of the lightest materials, and thus even a few molecules adsorbed onto the graphene will make up a significant fraction of the total mass. Furthermore, its ultra-rigid mechanical property [1] pushes its resonance frequency into RF region [2-3]. Low mass density and high resonance frequency are expected to result in exceptional mass responsivity. As well as its superior material properties, graphene also possesses advantages on fabricating NEMS devices. Wafer-scale uniform single layer (SLG) and bilayer graphene (BLG) films have been demonstrated by using CVD growth method on metal substrates [4-7]. The graphene films grown by CVD method also show good quality in both electrical and thermal conductivity in comparison of mechanical exfoliated ones. By transferring these wafer-scale graphene films onto process substrates, one can utilize the conventional top-down processing techniques to fabricate NEMS devices on "graphene substrates". The combination of bottom-up graphene synthesis and top-down NEMS fabrication enables large scale parallel arrays of graphene resonators for scalable device applications.

In this chapter, we present our initial experimental results of graphene resonators and point out some problems from which graphene resonators are suffering as the future research directions. The process procedure of graphene resonators is illustrated in section 6.2 and the measurement setup is described in section 6.3. In section 6.4, the initial experimental results of our graphene resonators are presented. Graphene resonators also suffer the issue of low Q. Future directions of graphene resonators include investigating the potential losses, exploring the origin of nonlinear damping, and demonstrating parametric amplification for Q enhancement, which will be described in section 6.5. Making a large array of graphene resonators with different geometry aspect ratio (w/l) should give us more insight ideas regarding these issues. For Q enhancement of graphene resonators, we expect the same approach we applied on the SWNT resonators would improve the Q of graphene resonators more efficiently.

6.2 Fabrication of graphene resonators

6.2.1 Synthesizing graphene films by CVD method

Following the recipes of Lee et al [5], we use 25µm thick copper foil (99.8%, Alfa Aesar) as starting substrate to grow graphene films. Firstly, the copper foil is loaded into a furnace of a commercial CVD system (Firstnano Easytube 3000). The system is purged with argon gas (Ar) and evacuated to a vacuum of 0.01 torr. The sample is then heated to 1000 ℃ in H_2 environment with vacuum level of 0.35 torr. Depending on the layer numbers of graphene film, CH_4 is purged during the heating-up period accordingly. When 1000 ℃ is reached, CH_4 (70 sccm) is flowed for 15 minutes at vacuum level of 0.45 torr for graphene growth. The system is then cooled down slowly to room temperature with a feedback loop to control the cooling rate.

6.2.2 Transferring graphene films

The basic procedure of transferring graphene onto substrate is described below. A thin polymer film is first deposited onto the copper foil after graphene is grown. Then the copper foil is etched away in acid solution, leaving graphene attached with the polymer film. This polymer film is then deposited onto an arbitrary substrate and after removing the polymer, graphene is left on the substrate. Specifically, we coat our sample with Polymethyl methacrylate (950 PMMA A4) and cured it at 180℃ for 5 minutes. The other side of the sample is etched by O_2 plasma for 30 seconds to remove the graphene on that side. The sample is then left in solution (Aluminum Persulfate) for at least 12 hours to completely dissolve away the copper and transferred on to the substrate. Lastly, the PMMA is cleaned with acetone for 4 hours and rinsed with IPA.

6.2.3 Suspending graphene beams

The process flow of fabricating suspended graphene resonators is illustrated in Figure 6.1. Firstly, 285 nm thermal SiO_2 is grown on a degenerately doped silicon wafer. To reduce the effect of parasitic capacitance, a local gate is employed instead of using conventional global gate. A local gate electrode is placed on the surface and covered by PECVD SiO_2 (450 nm). Then, the un-patterned CVD graphene film is transferred onto the wafer for further processing. The transferred graphene are patterned into an array of rectangles with different aspect ratios by using standard photolithography. The remaining photoresist is cleaned by soaking the sample in the solvent for 4 hours. Next, Cr/Au=5 nm /100 nm are deposited as contact metals. To make suspended graphene beams, SiO_2 underneath the graphene is removed by using BHF. Lastly, we dry the sample by conducting a critical-point dry step (915B Supercritical Dry) to avoid tension on the graphene beam caused by water.

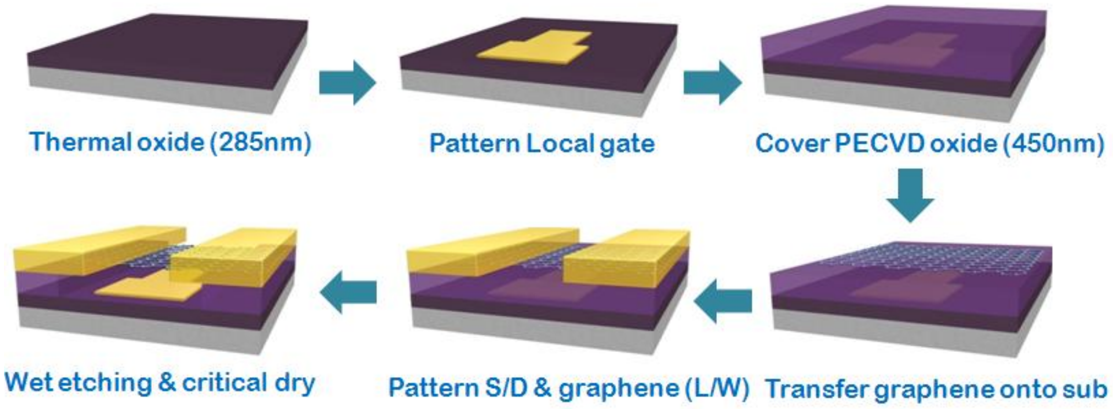

Figure 6.1. Procedure of fabricating graphene resonators. 285 nm thermal SiO_2 is first grown on a degenerately doped silicon wafer. A local gate electrode is placed on the surface and covered by PECVD SiO_2 (450 nm). Then, the un-patterned CVD graphene film is transferred onto the wafer for further processing. The transferred graphene are patterned into an array of rectangles with different aspect ratios by using standard photolithography. Next, Cr/Au=5 nm /100 nm are deposited as contact metals. To make suspended graphene beams, SiO_2 underneath the graphene is removed by using BHF and the sample is dried by a critical-point dry step to avoid tension on the graphene beam caused by water.

6.3 *Measurement setup*

To actuate and detect graphene resonators, the electrical approach same as we utilized in measuring nanotube resonators is adopted. Employing this approach to measure the resonance signals relies on good gate response of conductivity of SLG and BLG [3], meaning that high quality graphene films are required. In our measurement setup, both amplitude modulation (AM) and frequency modulation (FM) are utilized [8-9], as shown in figure 6.2. A small signal ($\Delta\omega$) from a lock-in amplifier is sent to the signal generator to be modulated with the driving signal (ω). The modulated signal is then sent to the source electrode to actuate the resonance and the mixing current from the drain electrode is measured by the lock-in amplifier to determine the resonance.

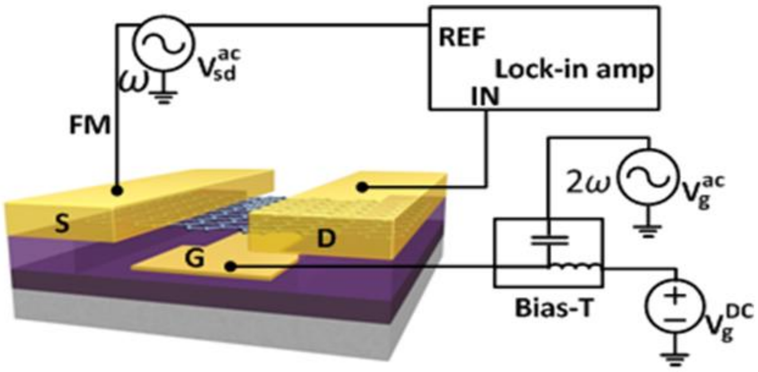

Figure 6.2. Measurement setup of measuring graphene resonators. A small signal ($\Delta\omega$) from a lock-in amplifier is sent to the signal generator to be modulated with driving signal (ω). The modulated signal is then sent to the source electrode to actuate the resonance and the mixing current from the drain electrode is measured by the lock-in amplifier to determine the resonance. For parametric amplification, the pumping signal at frequency $2\omega_0$ is added to the DC gate voltage through the bias T and applied to the gate electrode.

6.4 Experimental results

The SEM image of a doubly-clamped graphene resonator with dimensions of 1 x 3 μm^2 (w x l) is shown in figure 6.2 (a), where a well-defined suspended graphene beam is clamped by metal contacts at both ends. Here, we note that the solution process to remove the underneath SiO_2 is a very critical step. Graphene beams may be damaged during this process, resulting in the graphene beam broken, or torn apart, as shown in figure 6.2 (b). Next, we evaluate the electrical conductance of our graphene devices by using a suspended graphene FET configuration. Figure 6.3 (a) shows the conductance vs. gate voltage for a typical suspended graphene transistor (1 x 1 μm^2). The resistance is ~7 kΩ. In addition, the curve exhibits negligible hysteresis, indicating that the graphene beam is indeed suspended in the air.

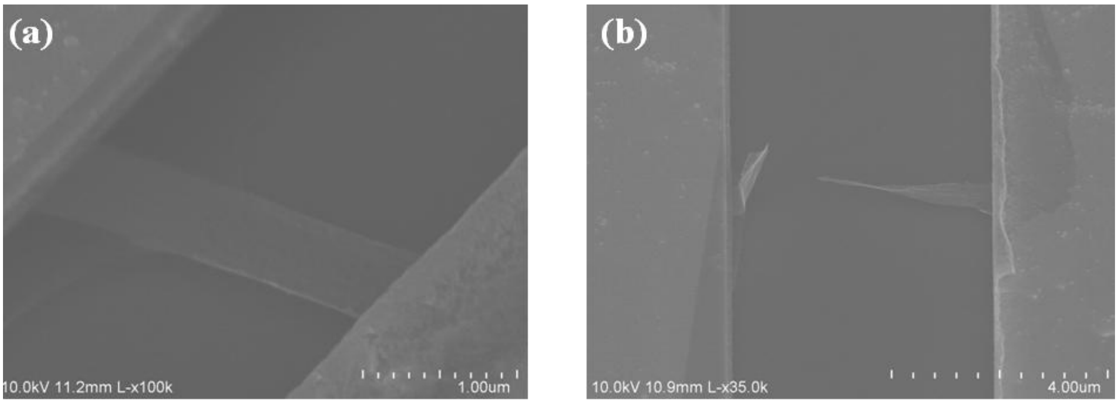

Figure 6.3. SEM image of a doubly-clamped graphene resonator. (a) A well defined suspended graphene beam (1 x 3 μm^2) is clamped by metal contacts at both ends. (b) A graphene beam is broken and torn apart after solution process.

Last, we measure the resonance signals of graphene resonators. The graphene resonators are measured in a vacuum chamber at pressure below 10^{-4} torr and V_{sd}^{ac} = 20 mV is applied to drive the graphene beam into motion. The electromechanical response of a typical graphene resonator with dimensions of 1 x 3 μm^2 is shown in figure 6.3 (b). The DC gate voltage (V_g) is fixed at 3 V, and the frequency-dependent mixing current (I_{mix}) swept between 27 and 31MHz reveals a clear resonance mode of the doubly clamped graphene resonator (black line). To obtain the resonance frequency, we fit the experimental data with equation (5.3) (red line), yielding the resonance frequency, f_0 = 29 MHz with quality factor Q = 70, which is a typical value obtained in graphene resonators.

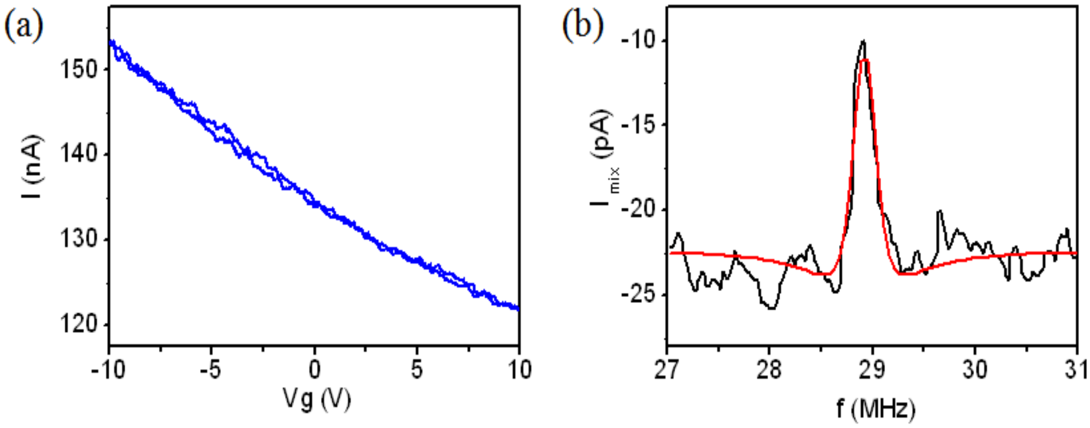

Figure 6.4. Characterization of graphene resonators. (a) Conductance vs. gate voltage of a typical graphene transistor (1 x 1 μm^2). The curve exhibits negligible hysteresis, indicating that the graphene beam is indeed suspended in the air. (b) Electromechanical response (black line) of a typical graphene resonator with dimensions of 1 x 3 μm^2. The DC gate voltage (V_g) is fixed at 3 V and the resonance frequency is f_0 = 29 MHz with quality factor Q = 70.

6.5 Outlook of graphene resonators

6.5.1 Exploring nonlinear dynamics

For resonators with atomic-scale transverse dimensions, such as nanotube and graphene resonators, previous study showed that the simple linear damping scenario breaks down and their behaviors have to be explained by including a nonlinear damping term $\eta x^2\, dx/dt$, where η is the coefficient of nonlinear damping [10-11]. The effect of nonlinear damping is prominent, especially in determining DR and Q. As the driving force increases, the nonlinear damping starts to be dominant due to larger vibrational amplitude. As a result, the quality factor is no longer independent on driving force and Q^{-1} is proportional to $m^{-1}\eta^{1/3}f_0^{-2/3}F_{drive}^{2/3}$. These results show the possibility in controlling the quality factor by exploiting the nonlinear damping. For example, higher Q can be obtained by minimizing the driving force.

The origin of nonlinear damping is still unknown currently. It may stem from the concerted effect of a standard dissipation channel such as contamination and geometrical nonlinearity arising from the elongation of a doubly clamped resonator on deflection. Exploring the possible origins is essential when we try to exploit the nonlinear damping to control the Q. Therefore, it is worthwhile to investigate the dependence of nonlinear damping on contamination, clamping configuration and suspended length. To examine the effect of contamination, a current annealing technique to remove contamination from graphene surface [12] can be employed. Extracting and comparing η with and without the presence of contamination, the dependence of contamination on nonlinear damping should be revealed. In addition, the dependence of clamping and suspended length on nonlinear damping can be studied by testing graphene resonators arrays with different aspect (l/w). By analyzing experimental results along with theory, the behind mechanisms is believed to be explored and allow us to utilize nonlinear damping more efficiently to purchase high-*Q* graphene resonators.

6.5.2 Pursuing high-Q graphene resonators

Increasing quality factors of graphene resonators is the priority when we try to sell them as promising candidates in future NEMS. As a result, understanding the possible constrains of quality factors is important. In addition, if the low *Q* is due to the intrinsic limits, we then may need to seek an external way to enhance the *Q*.

A. Losses in graphene resonators

The main dissipations in graphene resonators are still under debate so far. Previous studies have suggested several possible loss mechanisms and predicted the intrinsic limits of quality factors theoretically [13-16]. Firstly, the "spurious edge modes" due to different vibrational properties of the edge carbon atoms has been proved as one important loss source both theoretically and experimentally. In addition, loss due to the friction between the graphene and supporting substrate (clamping loss) is calculated. The simulation results indicate that clamping loss will significantly reduce *Q* and setup the upper limit of *Q*. In addition, the interlayer friction also shows considerable affect on *Q*, implying BLG resonators may have relatively lower *Q* than SLG resonators. Intrinsic thermoelastic loss is also believed to play a pivotal role in limiting the *Q* for true low dimensional resonators. Lastly, entropic spectral broadening could also be a possible loss in graphene resonators.

As discussing in section 2.6, for a conventional doubly-clamped beam resonator, the clamping loss is proportional to $(l/w)^3$, where l and w are the length and width, respectively. Large aspect ratio is expected to result in large clamping loss. Here, to examine the theoretical prediction, a series of graphene resonators with controlled aspect ratio (l/w) can be carried out to test the dependence of clamping loss on Q. Due to the well homogeneity of our graphene films, the parasitic effects such as surface losses are expected to be suppressed, making our graphene resonators an excellent platform for systematic studies of the clamping loss. In addition, the effect of interlayer friction can be verified by fabricating resonators with both SLG and BLG films.

Moreover, based on the theoretical prediction, the upper bound of quality factor setup by the clamping loss is below a thousand, meaning that little can be done to improve Q from device fabrication side. As a consequence, an external approach for Q enhancement is necessary. To this end, exploiting parametric amplification for Q enhancement in graphene resonator will be a more feasible approach.

B. *Parametric amplification in graphene resonators*

To achieve parametric amplification, the measurement setup is illustrated in figure 6.2. An AC pumping voltage from the second RF signal generator is added to the DC gate voltage through a bias-T to modulate the spring constant of the graphene at $2f_{0.}$ From our preliminary results, we have demonstrated ~10 times enhancement of quality factor and achieved the highest Q of nanotube resonators at ambient temperature. Unlike a nanotube resonator with a slack, the beam of a graphene resonator is much stretched. As a consequence, we believed that parametric amplification will produce more efficient enhancement of quality factor in graphene resonators, enabling the light-weight graphene as high-Q NEMS resonator for single molecule and atomic mass sensing.

REFERENCE

[1]C. Lee *et al.*, "*Measurement of the elastic properties and intrinsic strength of monolayer graphene*", Science **321**, 385 (2008).

[2]J. S. Bunch *et al.*, "*Electromechanical resonators from graphene sheets*", Science **315**, 490 (2007).

[3]C. Y. Chen *et al.*, "*Performance of monolayer graphene nanomechanical resonators with electrical readout*", Nat. Nanotech. **4**, 861 (2009).

[4]X. S. Li *et al.*, "*Large-Area Synthesis of High-Quality and Uniform Graphene Films on Copper Foils*", Science **324**, 1312 (2009).

[5]S. Lee, K. Lee, and Z. H. Zhong, "*Wafer Scale Homogeneous Bilayer Graphene Films by Chemical Vapor Deposition*", Nano Lett. **10**, 4702 (2010).

[6]P. W. Sutter, J. I. Flege, and E. A. Sutter, "*Epitaxial graphene on ruthenium*", Nat. Mater. **7**, 406 (2008).

[7]Y. Lee *et al.*, "*Wafer-Scale Synthesis and Transfer of Graphene Films*", Nano Lett. **10**, 490 (2010).

[8]V. Gouttenoire *et al.*, "*Digital and FM demodulation of a doubly clamped single-walled carbon-nanotube oscillator: towards a nanotube cell phone*", Small, **6** 1060 (2010).

[9]V. Sazonova *et al.*, "*A tunable carbon nanotube electromechanical oscillator*", Nature **431**, 284 (2004).

[10]R. Lifshitz, "*Reviews of nonlinear dynamics and complexity*", Wiley-VCH vol. **1** (2008).

[11]A. Eichler *et al.*, "*Nonlinear damping in mechanical resonators made from carbon nanotubes and graphene*", Nat. Nanotech. **6**, 339 (2011).

[12]J. Moser, A. Barreiro, and A. Bachtold, "*Current-induced cleaning of graphene*", Appl. Phys. Lett. **91**, 163513 (2007).

[13]S. Y. Kim, and H. S. Park, "*The Importance of Edge Effects on the Intrinsic Loss Mechanisms of Graphene Nanoresonators*", Nano Lett. **9**, 969 (2009).

[14]R. A. Barton *et al.*, "*High, Size-Dependent Quality Factor in an Array of Graphene Mechanical Resonators*", Nano Lett. **11**, 1232 (2011).

[15]C. Seoanez, F. Guinea, and A. H. Castro, "*Dissipation in graphene and nanotube resonators*", Phys. Rev. B **76**, 124527 (2007).

[16]S. Y. Kim, and H. S. Park, "*Multilayer friction and attachment effects on energy dissipation in graphene nanoresonators*", Appl. Phys. Lett. **94**, 109118 (2009).

CHAPTER 7

CONCLUSION

In summary, I have implemented both self-detecting SWNT and graphene nanoelectromechanical resonators. To study their nonlinear dynamics, I investigated the frequency tuning mechanisms of SWNT resonators and demonstrated parametric amplifications for Q enhancement in SWNT resonators.

In chapter 3, I first carried out a one-step direct transfer technique to fabricate pristine SWNT nanoelectronics at ambient temperature. Briefly speaking, suspended SWNTs are grown across pillars on a quartz substrate, while predesigned electrodes are fabricated on a separate device substrate. The transfer of suspended SWNTs to the device substrate is implemented by simply bringing two substrates into contact. This process technique prevents unwanted contaminations from conventional lithography and further reduces surface losses. By using this technique, I fabricated SWNT resonators and also demonstrated a fully suspended SWNT p-n diode with ideality factor equal to 1.

SWNT resonators can be electrically actuated and detected by using a capacitive measurement scheme in conjunction with the mixing technique. Therefore, in chapter 4, the gate-induced frequency tuning mechanisms of SWNT resonators was studied. SWNT resonators adopting a dual-gate configuration were fabricated by using the one-step direct transfer technique and downward frequency tuning caused by capacitive spring softening was demonstrated for the first time in SWNT resonators. In addition, in-plane vibrational modes show stronger softening effect than fundamental out-of-plane mode, suggesting that the dual-gate configuration can also serve an experimental tool for differentiating vibrational modes.

For SWNT resonators as mass sensors, their mass sensitivities are impeded by the low quality factor. In chapter 5, parametric amplification was demonstrated for Q enhancement in SWNT resonators and the simplest parametric amplification scheme was implemented by modulating the spring constant of nanotube at twice the resonance frequency through electrostatic gating. Consequently, at least 10 times Q enhancement was achieved and Q of ~700 was the highest value reported at room temperature to date. In addition, this parametric amplification technique was expected able to be applied to other low-Q NEMS resonators. The $2f_0$ modulation through electrostatic gating offers a simple technique which can be easily adopted in various device geometries and the flexibility to be integrated with NEMS applications.

Lastly, in chapter 6, I examined the graphene resonators fabricated from wafer-scale graphene films grown by CVD method. Ultra-high frequency (UHV) graphene resonators were demonstrated, and the Qs of graphene resonators are around 100. The main dissipations leading to low Q are still unknown currently. As a result, improving low Q will be an important task. Future directions of graphene resonators include investigating the potential losses, exploring the origin of nonlinear damping, and demonstrating parametric amplification for Q enhancement. Leveraging the ability to fabricate a large array of graphene resonators from wafer-scale graphene films, those effects can be investigated systematically. These findings will be valuable for understanding the fundamental operations of graphene resonators and open up an opportunity to integrate them with other NEMS systems.